

Dissertation

zur

Erlangung der Doktorwürde (Dr. rer. nat.)

der

Gesamtfakultät für Mathematik, Ingenieur- und Naturwissenschaften

der

Ruprecht-Karls-Universität

Heidelberg

vorgelegt von

Jan Matthias Lüttgens

geboren in Frankfurt a. M.

Tag der mündlichen Prüfung

17. Dezember 2021

Strong Light-Matter Coupling
with
Single-Walled Carbon Nanotubes

Properties and Application

Gutachter

Prof. Dr. Jana Zaumseil


Prof. Dr. Malte Gather

Printed in Sweden by Media-Tryck, Lund University

Lund 2021



Media-Tryck is a Nordic Swan Ecolabel
certified provider of printed material.
Read more about our environmental
work at www.mediatryck.lu.se

MADE IN SWEDEN 

gewidmet meiner Mutter

Table of Contents

Abstract	iv
Kurzfassung	vi
Acknowledgements	viii
Abbreviations	x
1 Introduction	1
2 Background	5
2.1 Light-matter interaction.....	5
2.2 Microcavity exciton-polaritons	16
2.3 Single-walled carbon nanotubes.....	21
2.4 Organic photodiodes	32
3 Experimental methods	36
3.1 Sample preparation.....	36
3.2 Optical Characterization.....	40
3.3 Miscellaneous characterization techniques	47
3.4 Data analysis and simulation.....	48
4 Fluorescence dynamics of SWCNT exciton-polaritons	51
4.1 Introduction	51
4.2 SWNT exciton-polariton emission as a function of detuning	53
4.3 Oxide spacers for improved control over cavity tuning	55
4.4 Polariton population by scattering with acoustic phonons	58

4.5	Vibrationally assisted scattering vs. radiative pumping	61
4.6	Strong coupling of SWCNTs with luminescent sp^3 defects	66
4.7	Pristine vs. sp^3 -functionalized SWCNTs in the strong coupling regime.....	71
4.8	Time-dependent data of strongly coupled sp^3 -functionalized SWCNTs.....	73
4.9	Absence of the Purcell effect.....	76
4.10	Manipulating the polariton population with luminescent sp^3 defects.....	79
4.11	Summary and conclusion	83
5 Ultrafast dynamics of SWCNT exciton-polaritons.....		85
5.1	Introduction	85
5.2	Transparent metalclad cavity.....	87
5.3	Cavity transient transmission and reflectivity	90
5.4	Genetic algorithm fit	98
5.5	Polariton transient transmission	102
5.6	Decay associated difference spectra (DADS)	105
5.7	Polariton mediated biexciton transition.....	108
5.8	Summary and Conclusion	111
6 Spectroscopic photodetectors based on SWCNT exciton-polaritons.....		112
6.1	Introduction	112
6.2	Photodiode and heterojunction design	114
6.3	Strongly coupled heterojunctions	116
6.4	Tunable, strongly coupled photodetectors.....	118
6.5	Strongly coupled flat heterojunction photodiodes.....	122
6.6	Summary and conclusion	124

7 Conclusion and Outlook	126
8 Appendix	130
8.1 Chapter 4	130
8.2 Chapter 6	137
9 References	138

Abstract

Single-walled carbon nanotubes (SWCNTs) are a promising material for strongly coupled optoelectronic devices, due to their outstanding electrical properties in combination with their narrowband excitonic absorption and emission in the near-infrared. The rich SWCNT photophysics allow to study the interaction of exciton-polaritons with a range of other quasi-particles, such as phonons and biexcitons, as well as with synthetic, luminescent sp^3 defects at room temperature. However, the ultimate goal of polariton condensation has not been achieved with SWCNT exciton-polaritons so far, and hence understanding their specific polariton population mechanism with respect to their unique photophysical properties is crucial. Here, time-dependent fluorescence and transmission measurements are used to track the exciton-polariton population in strongly coupled metalclad microcavities, identify the dominant relaxation pathways and transitions, use luminescent sp^3 defects to increase the polariton population by radiative pumping, and manipulate the SWCNT absorption edge by strong coupling in hybrid organic photodiodes.

By investigating the fluorescence decay of SWCNT exciton-polaritons, it is shown, that the dominant population mechanism in this system is radiative pumping. To overcome the thusly imposed limitation of the polariton population by the low SWCNT photoluminescence quantum yield, the SWCNTs are functionalized with luminescent sp^3 defects, leading to a population increase up to 10-fold for highly emissive detunings (photon fractions $> 90\%$). By changing the substituents and the binding pattern, tuning of the defect emission could be further employed to access application-relevant near-infrared wavelengths and improve the conditions for polariton condensation.

Furthermore, the SWCNT exciton-polariton dynamics are studied in the ultrafast regime by transient transmission spectroscopy. The results reveal a polariton-mediated biexciton transition, that is threefold more efficient than in weakly coupled SWCNTs. The polariton to biexciton transition under off-resonant polariton excitation also indicates fast population transfer from dark

to bright polaritons beyond the exciton and photon dephasing times. The efficient biexciton transition of strongly coupled SWCNTs may enable to study correlated many-body states at room temperature, that are predicted for excitonic molecules in strongly coupled high quality cavities.

Lastly, strongly coupled SWCNT hybrid organic photodiodes are presented, demonstrating how exciton-polaritons enable light-detection far beyond the intrinsic SWCNT absorption edge. For equal external quantum efficiency, photocarrier generation was observed 200 nm further into the near-infrared as compared to previously reported strongly coupled photodiodes. Thus, representing the first step towards efficient and tuneable polariton-mediated photocurrent generation by SWCNT hybrid organic photodiodes at application-relevant wavelengths.

Kurzfassung

Einwandige Kohlenstoffnanoröhren (*Single-walled carbon nanotubes*, SWCNTs) sind aufgrund ihrer hervorragenden elektrischen Eigenschaften sowie ihrer schmalbandigen exzitonischen Absorption und Emission im nahen Infrarot ein vielversprechendes Material für optoelektronische Bauelemente im Regime der starken Licht-Materie-Kopplung. Die umfangreiche SWCNT-Photophysik ermöglicht die Untersuchung der Wechselwirkung von Exziton-Polaritonen (stark gekoppelte Licht-Materie Quasiteilchen) mit einer Reihe anderer SWCNT-Quasiteilchen, wie Phononen und Biexzitonen, sowie mit synthetischen, lumineszierenden sp^3 Defekten bei Raumtemperatur. Allerdings konnte für SWCNT-Exziton-Polaritonen bisher keine Polaritonenkondensation gezeigt werden. Daher ist das Verständnis der spezifischen Polariton-Populationsmechanismen in Bezug auf die photophysikalischen Eigenschaften der SWCNTs von entscheidender Bedeutung. In dieser Arbeit werden zeitabhängige Fluoreszenz- und Transmissionsmessungen verwendet, um die Exziton-Polaritonen-Population in stark gekoppelten Mikrokavitäten zu verfolgen und die dominanten Relaxationspfade und Übergänge zu identifizieren. Darauf aufbauend werden lumineszierende sp^3 -Defekte verwendet, um die Polaritonen-population mittels strahlendem Pumpen zu erhöhen. Abschließend wird demonstriert, wie die SWCNT-Absorptionskante durch starke Kopplung von Photodioden manipuliert werden kann.

Durch die Untersuchung der Fluoreszenzabklingzeit von SWCNT-Exzitonen-Polaritonen wurde gezeigt, dass der dominierende Populationsmechanismus strahlendes Pumpen ist. Um die daraus resultierende Begrenzung der Polaritonenpopulation durch die geringe SWCNT-Photolumineszenz-Quantenausbeute zu umgehen, wurden die SWCNTs mit lumineszierenden sp^3 Defekten funktionalisiert. Dies führte zu einer bis zu 10-fachen Zunahme der Polaritonenpopulation unter Abstimmung der Kavität zu hohen Photonanteilen ($> 90\%$). Durch Änderung der Substituenten und der Bindungsmuster könnte die Defektemission zu

anwendungsrelevanten Wellenlängen im nahen Infrarot verschoben werden. Außerdem könnten dadurch die Bedingungen für Polaritonenkondensation erheblich verbessert werden.

Darüber hinaus wurde die Exziton-Polariton-Dynamik der SWCNTs auf der Femtosekunden-Zeitskala mittels transientser Transmissionsspektroskopie untersucht. Die Ergebnisse zeigen einen Polariton-vermittelten Biexziton-Übergang, der dreimal effizienter ist als in schwach gekoppelten SWCNTs. Der Übergang von Polariton zu Biexziton existiert auch bei nicht-resonanter Polariton-Anregung. Dies ist ein Indiz dafür, dass auch nachdem Exziton- und Photon ihre Kohärenz verloren haben, ein effizienter Populationstransfer von dunklen zu hellen Polaritonen stattfindet. Des Weiteren könnte der effiziente Biexziton-Übergang in stark gekoppelten SWCNTs ermöglichen, korrelierte Mehrteilchenzustände bei Raumtemperatur zu untersuchen, die für exzitonische Moleküle in stark gekoppelten Kavitäten hoher Qualität vorhergesagt wurden.

Abschließend werden stark gekoppelte organische SWCNT-Hybrid-Photodioden vorgestellt. Mittels dieser Photodioden lässt sich demonstrieren, wie Lichtdetektion weit über die intrinsische SWCNT-Absorptionskante hinaus durch Exziton-Polaritonen ermöglicht werden kann. Dabei ließ sich die photo-induzierte Ladungsträgererzeugung bei gleichbleibender externen Quanteneffizienz über 200 nm weiter ins nahe Infrarot verschieben als bei zuvor publizierten stark gekoppelten Photodioden. Dies ist der erste Schritt, um den polariton-vermittelten, photoelektrischen Effekt bei anwendungsrelevanten Wellenlängen nutzbar zu machen.

Acknowledgements

Throughout the work on this dissertation, I have received tremendous support within and alongside the many different paths that had to be taken.

First of all, I would like to thank Prof. Jana Zaumseil for giving me the opportunity to work in her group, for her continuous support and guidance, and for helping me to develop my abilities as a scientist. I am grateful for all the valuable opportunities you have given me, to teach younger scientists, to present my scientific work at conferences and to develop my knowledge on optics in St. Andrews and Munich. Over the last few years, I could always be sure to have your support behind me.

I would like to thank Prof. Malte Gather for all my visits to his group in St. Andrews, for your openness and expertise, and for kindly agreeing to review this thesis.

I am thankful to all members of the NMOE and PC2D groups for the friendly and collaborative atmosphere at the Institut für Angewandte Physikalische Chemie. Especially, I want to thank Dr. Arko Graf and Dr. Yuriy Zakharko, who are the pioneers of strong coupling with nanotubes and who spent many lightless hours with me, passing on the flame. I also want to thank Dr. Katelyn Goetz, Dr. Maximilian Brohmann, Maik Matthiesen, Dr. Severin Schneider, Jan Gotthard, Sonja Wieland and Nicolas Zorn, for always being at hand, when there was any problem in the device fabrication lab.

I would like to thank my Master students, Timo Neumann and Matthias Sinnwell for the work load, they were willing to put into their projects, and for the great and inspiring time we had. I would also like to thank all my other students, Eduard Gevorkjan, Niklas Heinrich, Lukas Sigmund, Adam Tywoniak, Chase Zagorec-Marks and especially Julian Petry for their hard work.

Moreover, I would like to thank the excellent institute staff, who make important parts of our work possible in the first place. I thank Peter Jeschka, Günter Meinus, Reinhold Jehle, as well as Klaus Schmitt and his team to put even the most peculiar apparatus into being and I thank

Karin Jordan, Swetlana Duchnay and Benjamin Scherke for fixing any administrative issue that lay in the way.

Furthermore, I would like to thank all of my external collaborators, especially, Dr. Andreas Mischok, who came up with the idea for the strongly coupled SWCNT photodiodes, Dr. Zhouran Kuang for recording countless TA spectra, and Dr. Tiago Buckup, who was an invaluable support for analysing them. In addition, I would like to thank Prof. Alexander Högele and his group for hosting me and especially Dr. Samarth Vadia and Dr. Robin Patel for the great yet sleep-deprived time we had. I learned a lot from all of you and I am very grateful for the time we had.

I would like to thank Nadia, Pentti and Molly for their support during writing this work and Fabian, Phillipe, Steffen, Felix and Frida for proof reading.

Frida, thank you, for always being there for me.

Lastly, I would like to thank my parents for giving me immense support during this time and my brother for his imperturbable optimism.

Abbreviations

0D	zero-dimensional
1D	one-dimensional
2D	two-dimensional
AFM	atomic force microscopy
ALD	atomic layer deposition
BHJ	bulk heterojunction
BX	biexciton
CCD	charge coupled device
CoMoCat	cobalt-Molybdenum Catalyst CVD Technique
CW	continuous-wave
DOS	density of states
EQE	external quantum efficiency
FHJ	flat heterojunction
FWHM	full width half maximum
GA	genetic algorithm
HOMO	highest occupied orbital
HWHM	half width half maximum
IC	internal conversion
ISC	intersystem crossing
Laser	light amplification by stimulated emission radiation
LED	light emitting diode
LP	lower polariton
LUMO	lowest occupied orbital
NA	numerical aperture
NIR	near-infrared
NMP	N-methyl-2-pyrrolidone
MPD	multi-phonon decay
OPD	organic photodiode
OSC	organic solar cell
<i>p</i>	parallelly polarized
P3HT	poly(3-hexylthiophene-2,5-diyl)
PC ₇₀ BM	[6,6]-Phenyl-C ₇₁ -butyric acid methyl ester
PEDOT:PSS	poly(3,4-ethylenedioxythiophene) polystyrene sulfonate

PFO-BPy	poly[(9,9-dioctylfluorenyl-2,7-diyl)-alt-co-(6,6'-(2,2'-bipyridine))]
PL	photoluminescence
PLE	photoluminescence excitation-emission
PLQY	photoluminescence quantum yield
PTFE	polytetrafluorethylene
PSB	photoluminescence sideband
RMS	root mean square
RT	room temperature
<i>s</i>	vertically polarized
SWCNT	single-walled carbon nanotube
TA	transient absorption
TCSPC	time-correlated single photon counting
TD	thermal de-trapping
TE	transverse electric
THF	tetrahydrofuran
TM	transverse magnetic
TM <i>scheme/simulation</i>	transfer-matrix
TMA	trimethyl aluminium
TR	transient reflectivity
TT	transient transmission
UP	upper polariton
UV	ultraviolet
VAS	vibrationally assisted scattering
vis	visible

1 Introduction

Exciton-polaritons are part-matter, part-light quasi-particles, that are formed when an exciton interacts strongly with light. In the strong light-matter coupling regime, the rate of energy exchange between exciton and photon is larger than their decay rates.¹ This is encountered, when photons are trapped inside a material. The resulting so-called bulk exciton-polaritons were first observed for excitons in crystalline semiconductors.^{2, 3} However, with the development of semiconductor and thin film technology⁴, so-called microcavity exciton-polaritons could be created artificially using mirrors to increase the trapped photon's lifetime.⁵ As hybrid light-matter quasi-particles, exciton-polaritons are bosons possessing only 10^{-4} times the mass of an electron. This fostered research efforts into microcavity polariton physics. In 2006, Bose-Einstein-like condensation was first observed for exciton-polaritons in quantum wells of inorganic semiconductors at 5 K⁶ and shortly after, even under ambient conditions employing room-temperature stable excitons.⁷ Polariton condensates possess a plethora of unique quantum optical properties with spontaneously polarized laser-like emission⁸, long-range spatial coherence⁹ and superfluidity at room temperature¹⁰ being the most noteworthy. In contrast to similar physics observed using trapped atoms in the gas phase, exciton-polaritons are based on solid state microstructures, that can be implemented in conventional semiconductor devices. This was demonstrated by electrically creating a polariton condensate¹¹ based on a cavity-integrated light-emitting diode¹². The possibility of harnessing quantum optical phenomena on-chip under ambient conditions has stimulated the research interest in exciton-polaritons since.

Alongside research on exciton-polaritons in systems based on epitaxially grown quantum wells, a wide range of emitters has been investigated in regard to polariton formation and condensation over the last decade. Organic molecules^{7, 13, 14}, conjugated polymers^{15, 16} and fluorescent proteins^{17, 18} have been of special focus due to their room-temperature stable excitons and diverse

photophysics. For organic materials exhibiting optical gain, polariton lasing could be achieved over large parts of the visible spectrum.^{7, 13-22} The optical net gain achieved in polariton condensates of a ladder-type conjugated polymer surpasses the net gain found in weakly coupled semiconductor cavities by five-fold.²³ Exploiting the large gain and ultrafast dynamics of exciton-polaritons based on organic materials, an all-optical transistor with THz switching speed was demonstrated.²³ Furthermore, strong coupling with organic materials gave rise to the idea of modifying material properties without chemical modification.²⁴ Owing to the tunability of exciton-polaritons, photocurrent-generation²⁵⁻²⁷ and spin conversion²⁸⁻³² in organic materials could be manipulated and exploiting the delocalized nature of exciton-polaritons, energy transfer between spatially separated molecules^{33, 34} and long-range energy transport^{35, 36} in disordered molecular systems could be improved in the strong coupling regime.

More recently, low dimensional semiconductors such as monolayered transition metal dichalcogenides³⁷, 2D perovskites³⁸, zinc oxide nanowires³⁹ and single-walled carbon nanotubes⁴⁰ were studied. Among these, semiconducting single-walled carbon nanotubes (SWCNTs) have emerged as an interesting material to create exciton-polaritons optically as well as electrically in the near infrared (NIR).⁴¹⁻⁴⁵ In contrast to organic materials, SWCNTs combine high ambipolar charge carrier mobilities ($1,000-10,000 \text{ cm}^2\text{V}^{-1}\text{s}^{-1}$)^{46, 47} with large oscillator strength (~ 0.01)⁴⁸ and narrow excitonic absorption and emission bands in film⁴⁰. Furthermore, chemical functionalization of a given SWCNT chirality allows to create bright and tuneable exciton trap states even further in the NIR.⁴⁹ These luminescent trap states, termed sp^3 defects, can be controlled in terms of functional group⁵⁰ and binding configuration⁵¹ and their zero-dimensional nature allows for high-purity single-photon emission at room temperature.⁵² In addition to that, SWCNTs exhibit a range of quasi-particles such as biexcitons⁵³, trions⁵⁴ and polarons⁵⁵ at room temperature. Together with their clear polariton mode structure⁴⁰, SWCNT can serve as a test bed to investigate polariton interaction with other quasi-particles and artificial defects. So far, cavity-mediated hybridization of bright excitons with trions⁴² and dark excitons⁵⁶ has been observed and

the resulting polaritons offer means to manipulate the photophysics of the underlying SWCNTs by strong coupling.^{42, 56} This makes SWCNTs a unique material to study exciton-polaritons and a promising candidate for optoelectronic devices in the strong coupling regime.

Up to now, polariton condensation could not be demonstrated with SWCNTs and hence understanding their specific polariton population mechanism with respect to their photophysical properties has become crucial. Connected to the polariton population and dynamics is the role of the polariton dark states. These dark states are believed to be crucial to the polariton dynamics^{57, 58} and therefore understanding interaction between bright and dark polariton states in SWCNTs is essential to design and improve polariton-based devices in general. More specifically, the low SWCNT PLQY may inhibit large polariton populations required for condensation and means to increase the PLQY are of interest.

This thesis focuses on the population mechanisms and dynamics of SWCNT exciton-polaritons. By investigating the fluorescence decay of SWCNT exciton-polaritons, it is shown, that the dominant population mechanism in this system is radiative pumping. To overcome the thusly imposed limitation of the polariton population by the low SWCNT PLQY, luminescent sp^3 defects are used to radiatively populate polaritons and increase polariton population in the NIR. Furthermore, the SWCNT exciton-polariton dynamics are studied in the ultrafast regime by transient transmission spectroscopy. The results reveal an efficient polariton-mediated biexciton transition and that the dark state dynamics can be bypassed on the femtosecond timescale under resonant polariton excitation. The thesis is concluded with the presentation of strongly coupled SWCNT photodiodes, demonstrating how exciton-polaritons enable light-harvesting far beyond the intrinsic SWCNT absorption edge.

The thesis is structured as follows: Firstly, the fundamental equations and concepts to describe strong light-matter coupling of SWCNTs are presented, together with the current state of research on SWCNT and exciton-polariton spectroscopy. In addition, the working principles of planar microcavities and organic photodiodes are introduced (Chapter 2). Subsequently, the

experimental methods used in this thesis are described (Chapter 3). In the result section of the thesis, the population mechanism of the polariton bright states is identified using time-dependent fluorescence measurements and based on this, a method to tailor and increase the polariton population using luminescent sp^3 defects is demonstrated (Chapter 4). In the following, the ultrafast dynamics of SWCNT polaritons as observed transient transmission spectroscopy are presented and analysed (Chapter 5). The result section is concluded with the presentation of strongly coupled hybrid organic photodiodes based on SWCNTs (Chapter 6). Chapter 7, summarizes the main results of this thesis and based on this, develops an outlook on future work.

2 Background

This chapter introduces light-matter interaction, firstly from a macroscopic perspective, and secondly from a microscopic perspective. On that basis, the manipulation of light-matter interaction by planar microcavities is described and strong light-matter coupling is discussed. The current understanding of microcavity exciton-polaritons and their dynamics is presented, followed by a summary of single walled carbon nanotube (SWCNT) photophysics, functionalization and their application within strong light-matter coupling. The chapter concludes with an introduction of organic photodiodes.

2.1 Light-matter interaction

In the following, key aspects of light-matter interaction are introduced, serving as a basis to describe microcavity exciton-polaritons. The discussion aims to present and motivate the models and equations used in this thesis.

2.1.1 Dielectric function and complex refractive index

In a macroscopic description of light-matter interaction, light is described as an oscillating electromagnetic (EM) field that interacts with the charged building blocks of matter, namely electrons and protons, in form of a temporary polarization. For diamagnetic materials, in the absence of external magnetic fields and below radiofrequencies, the magnetic component can be neglected.⁵⁹

In the macroscopic description, different materials are characterized phenomenologically in terms of their permeability towards the electric field component of light, which is described by the dielectric function $\varepsilon(\omega)$ of the material and depends on the angular frequency ω of the light wave.⁵⁹ The dielectric function is connected to the complex index of refraction \tilde{n} by⁴

$$\sqrt{\varepsilon(\omega)} = \tilde{n}(\omega) = n(\omega) + ik(\omega), \quad (1)$$

where the real part $n(\omega)$ affects the oscillatory spatial motion of the electric field and corresponds to Snell's index of refraction. The imaginary part $k(\omega)$ affects the damping of the field in propagation direction within the material and corresponds to the extinction coefficient.⁵⁹ If either the dielectric function or the complex refractive index of a material is known, the light-matter interaction can be described on the basis of Maxwell's equations, yielding transmission, reflection and absorption.⁶⁰ Experimentally, the complex refractive index can be measured by ellipsometry. The n and k parts are causally connected that is, damping of the light field will always change its oscillatory spatial motion and *vice versa*. Hence, measuring one part over a sufficiently large frequency range allows to calculate the respective other part.⁵⁹ Experimentally, the imaginary part k can be readily determined by measuring the absorption A and film thickness d of a given material slab using the relation⁶¹

$$k(\omega) = \frac{A_{\text{OD}}(\omega) \cdot c}{\log_{10} e \cdot 2\omega d}, \quad (2)$$

where c is the speed of light and e is Euler's number and A is given in optical density (OD). The real part n can then be calculated using the Kramers-Kronig relation⁵⁹

$$n(\omega) = 1 + \frac{2}{\pi} \text{CH} \int_0^{\infty} \frac{\omega' k(\omega')}{\omega'^2 - \omega^2} d\omega', \quad (3)$$

where CH is Cauchy's principle value. The Kramers-Kronig relation is a mathematical property of the complex function $\tilde{n}(\omega)$, expressing the aforementioned causality between n and k . The next section illustrates how reflectivity, transmission and absorption of different materials can be calculated using $\tilde{n}(\omega)$.

2.1.2 Transfer matrix scheme

Light propagation in a homogeneous medium, as introduced in the previous section, can be formalized by the transfer matrix (TM) scheme, which is here adapted from Pettersson *et al.*⁶¹.

The TM scheme is a powerful approach that can be easily extended to stacks of different materials, as found in optical components or optoelectronic devices. For this, each layer j ($j = 1, 2, \dots, m$) is described in terms of its thickness d_j and complex index of refraction \tilde{n}_j . Light is described as a plane harmonic wave propagating through the stack, which will be referred to as positive z -direction with an arbitrary angle of incidence θ . The electric field amplitude of the light wave within each layer is given by \mathbf{E}_j^+ for forward propagating light and \mathbf{E}_j^- for backward propagating light. For anisotropic material layers, such as polymers or networks of carbon nanotubes, the complex refractive index is given in terms of an in-plane component and a component in z -direction. Refraction at the layer interface jk is described by the matrix of refraction \mathbf{I}_{jk}

$$\mathbf{I}_{jk} = \frac{1}{t_{jk}} \begin{pmatrix} 1 & r_{jk} \\ r_{jk} & 1 \end{pmatrix}, \quad (4)$$

where r and t are the Fresnel complex reflection and transmission coefficients given by

$$r_{jk} = \frac{q_j - q_k}{q_j + q_k} \quad \text{and} \quad t_{jk} = \frac{2q_j}{q_j + q_k}, \quad (5)$$

for the electric field being perpendicular to the plane of incidence (s- or TE-polarized) and

$$r_{jk} = \frac{\tilde{n}_k^2 q_j - \tilde{n}_j^2 q_k}{\tilde{n}_k^2 q_j + \tilde{n}_j^2 q_k} \quad \text{and} \quad t_{jk} = \frac{2\tilde{n}_j \tilde{n}_k q_j}{\tilde{n}_k^2 q_j + \tilde{n}_j^2 q_k}, \quad (6)$$

for the electric field being parallel to the plane of incidence (p- or TM-polarized). The so-called momentum transfer q is described by $q_j = \tilde{n}_j \cos \theta_j = \sqrt{\tilde{n}_j^2 - n_0^2 \sin^2 \theta_j}$, where n_0 is the ambient refractive index and θ_j the angle of refraction in layer j . Propagation through the layer is given by the phase matrix \mathbf{L}_{jk}

$$\mathbf{L}_{jk} = \begin{pmatrix} \exp(-i\xi_j d_j) & 0 \\ 0 & \exp(-i\xi_j d_j) \end{pmatrix} \quad \text{with} \quad \xi_j = \frac{2\pi}{\lambda} q_j, \quad (7)$$

where $\xi_j d_j$ is the phase thickness of the layer and accounts for absorption losses. The so-called transfer or scattering matrix \mathbf{S} is the product of all optical processes within the stack

$$\mathbf{S} = \begin{pmatrix} S_{11} & S_{12} \\ S_{21} & S_{22} \end{pmatrix} = \left(\prod_{v=1}^n \mathbf{I}_{(v-1)v} \mathbf{L}_v \right) \mathbf{I}_{m(m+1)}. \quad (8)$$

Using the transfer matrix \mathbf{S} , the amplitudes of in- (E_0) and outgoing (E_{m+1}) light can be calculated by

$$\begin{pmatrix} \mathbf{E}_0^+ \\ \mathbf{E}_0^- \end{pmatrix} = \mathbf{S} \begin{pmatrix} \mathbf{E}_{m+1}^+ \\ \mathbf{E}_{m+1}^- \end{pmatrix}. \quad (9)$$

If light is incident from positive z -direction and no light is entering the stack in negative z -direction $\mathbf{E}_{m+1}^- = 0$, the reflectivity R and transmission T can be calculated by

$$R = |r|^2 \quad \text{with} \quad r = \frac{\mathbf{E}_0^-}{\mathbf{E}_0^+} = \frac{S_{21}}{S_{11}}, \quad (10)$$

$$T = |t|^2 \quad \text{with} \quad t = \frac{\mathbf{E}_{m+1}^+}{\mathbf{E}_0^+} = \frac{1}{S_{11}}. \quad (11)$$

If scattering is negligible, the absorption A can be calculated directly by

$$A = 1 - R - T. \quad (12)$$

The TM scheme can also predict the electric field intensity within the stack and the corresponding equations can be found in Pettersson *et al.*⁶¹.

In real samples, a non-negligible interlayer roughness is usually present. In first approximation this can be accounted for by scalar scattering using modified Fresnel coefficients and the roughness coefficient σ , as adapted from Yin *et al.*⁶²:

$$r_{jk}' = r_{jk} \exp(-2(2\pi\sigma/\lambda)^2 \tilde{n}_j^2) \quad \text{and} \quad r_{kj}' = r_{kj} \exp(-2(2\pi\sigma/\lambda)^2 \tilde{n}_k^2), \quad (13)$$

$$t_{jk}' = t_{jk} \exp(-(2\pi\sigma/\lambda)^2 (\tilde{n}_j - \tilde{n}_k)^2 / 2) \quad \text{and} \quad t_{kj}' = t_{kj} \exp(-(2\pi\sigma/\lambda)^2 (\tilde{n}_k - \tilde{n}_j)^2 / 2), \quad (14)$$

here, λ is the wavelength. For sufficiently homogenous layers, that is, with low intralayer scattering, the thusly adapted TM scheme reproduces experimental transmission and reflectivity spectra reasonably well. In this thesis, the TM scheme is used to simulate the transmission and reflectivity of strongly and weakly coupled microcavity samples.

2.1.3 Planar microcavities

Light-matter interaction can be modified using optical resonators. Optical resonators confine light spatially and temporally and by this manipulate the light-matter interaction of a material placed inside the resonator. A planar or also called Fabry-Pérot cavity is an optical resonator comprised of two parallel mirrors separated by the cavity length L_C . Cavities with L_C approaching the wavelength of light are termed microcavities and in this thesis the term *cavity* will always refer to *microcavity*. The resonance condition is constructive interference. For a light wave passing through a cavity under zero degree incidence, any integer multiple of the perpendicular wavevector component k_{\perp} (of the total wavevector k) fulfils the resonance condition⁶⁰ (Figure 2.1a)

$$k_{\perp} = \frac{m\pi}{n_{eff}L_C} \quad \text{with} \quad k_{\perp} = k\cos(\theta), \quad (15)$$

where $m \in \mathbb{N}$ is termed the cavity order and n_{eff} is the effective refractive index between the mirrors. However, for light traveling under an angle θ_{in} inside the cavity, the total wavenumber k can be larger than $2\pi/\lambda$, leading to a characteristic quasi-parabolic energy dispersion given by⁶³

$$E_C(\theta) = \frac{hck}{2\pi} = \frac{hcm}{n_{eff}L_C\cos(\theta)} = E_{0,m}(1 - (\sin(\theta)/n_{eff})^2)^{-1/2}, \quad (16)$$

where the internal angle θ_{in} , was replaced by the external angle of incidence using Snell's law $\sin(\theta_{in}) = n_{air}\sin(\theta)/n_{eff}$. With increasing angle, the electric field oscillates within the cavity materials to different extents depending on its orientation, which leads to a mode splitting at high-angles. Light with the electric field parallel to the plane of incidence forms the so-called TM- or p-branch, whereas light with the electric field perpendicular to the plane of incidence forms the TE- or s-branch. Furthermore, higher order cavity modes can be observed if the reflectivity of the mirror is spectrally broad enough, as is the case for metal mirrors.

The cavity quality is described by the Q -factor, which is the ratio between the resonant cavity frequency ω_c and the full width half maximum (FWHM) $\Delta\omega_c$ of the cavity mode and is directly related to the photon lifetime τ_c within the cavity

$$Q = \frac{\omega_c}{\Delta\omega_c} \quad \text{or} \quad Q = \omega_c \tau_c. \quad (17)$$

The photon population inside the cavity is decaying exponentially due to absorption, scattering and leakage through the cavity mirrors. The former two require the material between the mirrors to exhibit a low parasitic absorption and a high homogeneity. The latter one can be reduced by increasing the mirror reflectivity to yield high Q -factors. In case of metal mirrors, this can be achieved by increasing the metal layer thickness. But because metals have high extinction coefficients, the reflectivity becomes limited by absorption (Figure 2.1b, dashed grey line). Theoretically, metals, especially gold, can still provide high Q -factors up to 500 in the near IR.⁶⁰ However, for organic or nanomaterials as a cavity layer, the Q -factor is usually limited to values below 100^{40, 64-67}, due to intrinsically high scattering and layer roughness. Higher quality factors can be achieved with dielectric mirrors, which have negligible absorption. However, dielectric mirrors provide reduced light confinement, as their reflectivity is based on sequential partial reflection and the light field penetrates far into the dielectric mirror before it is completely reflected.⁴ Accordingly, selection and design of the cavity mirrors is crucial for cavity performance and can be rationalized by TM simulations introduced in the previous section. In the following sections, the modification of the light-matter interaction by planar microcavities is discussed from a microscopic perspective.

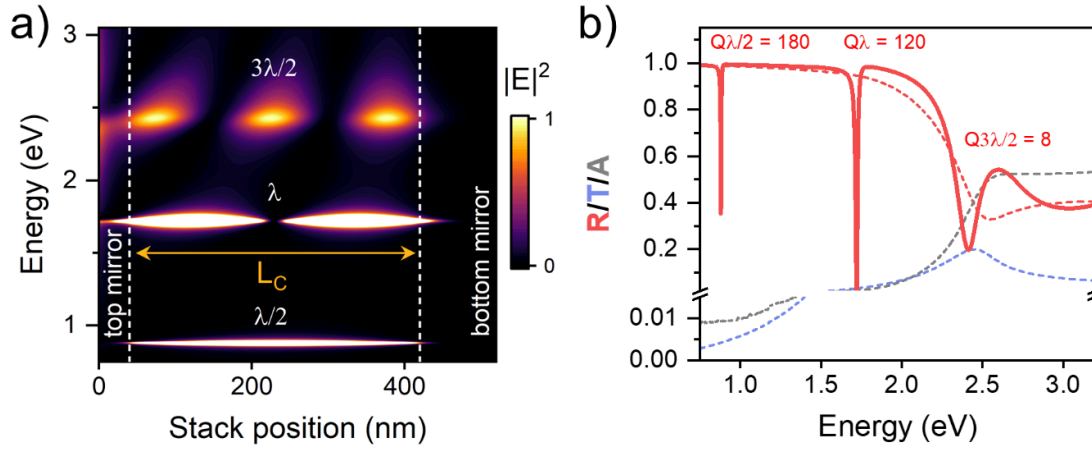


Figure 2.1 **a)** Simulated electric field intensity inside a gold mirror cavity as a function of position within the stack. Dashed lines indicate the semi-transparent top and fully reflective bottom mirror. **b)** Simulated reflectivity of the cavity (red solid line) depicted in (a) with respective cavity mode Q-factors. The dashed lines show reflectivity (red), transmission (blue) and absorption (grey) of the top mirror.

2.1.4 Weak light-matter coupling

To treat phenomena such as light emission, especially with regard to cavity enhancement, a microscopic description has to be employed. An excited state E_e can relax to its ground state E_g by emitting a photon with a frequency ω equivalent to the energy difference between the two states:

$$\hbar\omega = E_e - E_g. \quad (18)$$

Assuming, that the ground state is not re-excited for some time (i.e. weak light-matter coupling), the probability for the excited state to emit a photon of frequency ω can be calculated by Fermi's golden rule⁶⁰

$$\frac{1}{\tau_{sp}} = \frac{2\pi}{\hbar} |\langle f | \mathcal{H}' | i \rangle|^2 \rho_f(\omega), \quad (19)$$

where \hbar is the reduced Plank's constant, $\langle f | \mathcal{H}' | i \rangle$ denotes the matrix element describing the coupling between initial excited state and final photon state for a first order perturbation and ρ_f denotes the density of available photon states with frequency ω . Owing to the probabilistic nature

of this process the rate $1/\tau_{sp}$ is called rate of *spontaneous emission*.⁴ In free space, the emission process is irreversible due to the large number of photon states. Furthermore, the transition probability purely depends on the nature of the excited state $|f\rangle$ in free space⁵⁹ and is therefore also termed *radiative rate* with respect to material properties.

The efficiency of light-matter interaction between an excited state and light is commonly described as the oscillator strength f given by⁵⁹

$$f = \frac{2m\omega_0}{\hbar e^2} |\langle f | \mathcal{H}' | i \rangle|^2, \quad (20)$$

where m is the mass of the oscillator e.g., an electron, ω_0 is the oscillator frequency and e is the elementary charge. Although, a high oscillator strength indicates efficient light-matter interaction, it does not necessarily indicate high luminescence. The excited state can also relax via non-radiative processes such as energy dissipation through vibrations in molecules or lattice vibrations (phonons) in solids. These non-radiative decay processes can be fast compared to the spontaneous emission rate, even for high oscillator strengths. In the following, the term excited state will refer to electronic excitations and especially excitons (bound electron-hole pairs).

2.1.5 The Purcell effect

With the considerations made in the previous section, the effect of optical resonators on emissive materials becomes apparent: In the weak-coupling picture, optical resonators change the number of available photon states into which the emitter can decay radiatively, consequently modifying the spontaneous emission rate.⁴ Note, however, that plasmonic resonators may also affect non-radiative decay rates.⁶⁸ For a resonator detuned from the emission wavelength, the number of available photon states is reduced compared to free space, leading to a decrease of the emitter's radiative decay rate. If the emission wavelength is in resonance, the number of available photon states is increased compared to free space, resulting in an increase of the radiative decay rate. The latter case is termed Purcell enhancement. For a planar microcavity the Purcell factor at the resonance wavelength λ_C depends on the cavity quality factor Q by⁶⁰

$$F_P^{2D} = \frac{1}{4\pi n_{\text{eff}} L_C} Q \quad (21)$$

and gives the ratio between the emitter's radiative decay rate in the cavity and free space $F_P^{2D} = \gamma_{rad}^C / \gamma_{rad}$. Experimentally, Purcell enhancement can be observed by a decrease in photoluminescence (PL) lifetime τ_{PL}

$$\tau_{PL} = \frac{1}{\gamma_{non-rad} + \gamma_{rad}}, \quad (22)$$

where $\gamma_{non-rad}$ is the non-radiative decay rate, and an increase of the photoluminescence quantum yield (PLQY) Φ , which is given by

$$\Phi = \gamma_{rad} \cdot \tau_{PL}. \quad (23)$$

Inside the cavity, the radiative lifetime is decreased by F_P^{2D} . Using equations (22) and (23) the PL lifetime for a weakly coupled emitter inside a cavity can be written as

$$\tau_{PL}^C = \frac{1}{\gamma_{non-rad} + F_P^{2D} \gamma_{rad}} = \left(\left(\frac{1 - \Phi}{\tau_{PL}} \right) + F_P^{2D} \left(\frac{\Phi}{\tau_{PL}} \right) \right)^{-1}. \quad (24)$$

Purcell enhancement has been successfully applied to improve the emission pattern and brightness of light-emitting diodes (LEDs)^{69, 70} as well as the efficiency and dephasing in single-photon sources⁷¹⁻⁷³.

2.1.6 Strong light-matter coupling

Due to the Purcell effect, the radiative lifetime of the exciton τ_X decreases with increasing cavity reflectivity, while the photon lifetime τ_C increases. The cavity enhancement can be brought to an extreme regime in which cavity photon and exciton decay rates become equal and photon and exciton start to coherently exchange energy before they decay.⁵⁹ This regime cannot be treated perturbatively anymore as in section 2.1.4, as the emitter is constantly re-excited, and it is therefore termed strong light-matter coupling regime. In the strong coupling regime, photon and exciton possess a common lifetime, which is $\frac{\tau_X + \tau_C}{2}$ for resonance and leads to broadening and

splitting of the cavity mode (Figure 2.2a and b). The transition between strong and weak coupling regime can be analysed by describing exciton and photon (or cavity mode) with a coupled oscillator (CO) model using the Hamiltonian⁷⁴

$$\mathcal{H} = \begin{pmatrix} E_x - i\hbar\Gamma_x & V \\ V & E_c(\theta) - i\hbar\Gamma_c \end{pmatrix}, \quad (25)$$

where E_x is the exciton energy and $\hbar\Gamma_x$ is the homogeneous linewidth given in terms of half width at half maximum (HWHM). $E_c(\theta)$ is the cavity energy given by equation (16) and $\hbar\Gamma_c$ is the respective HWHM linewidth. The energy difference $E_x - E_c(0)$ is termed detuning Δ . For zero detuning or resonance ($E_x \approx E_c(0)$), the matrix element V and the cavity linewidth $\hbar\Gamma_c$ can be written in terms of cavity mirror reflectivity R :⁷⁵

$$V = \sqrt{\frac{1 + \sqrt{R}}{\sqrt{R}}} \frac{c\hbar\Gamma_x^0}{n_{eff}L_c}, \quad (26)$$

$$\hbar\Gamma_c = \frac{1 - \sqrt{R}}{\sqrt{R}} \frac{\hbar c}{n_{eff}L_c}, \quad (27)$$

where $\hbar\Gamma_x^0$ is the exciton homogeneous linewidth without cavity enhancement. The diagonalized form of the Hamiltonian (25) is

$$E = \frac{1}{2}(E_x + E_c(\theta) - i(\hbar\Gamma_x + \hbar\Gamma_c)) \pm \sqrt{V^2 + 0.25(E_x - E_c(\theta) - i(\hbar\Gamma_x - \hbar\Gamma_c))^2} \quad (28)$$

and it can be given as a function of reflectivity using equations (26) and (27). If the cavity reflectivity is high enough, the square root expression becomes real. This occurs when the matrix element or coupling strength V is larger than half the sum of the exciton and photon linewidths

$$V > \frac{|\hbar\Gamma_x - \hbar\Gamma_c|}{2}. \quad (29)$$

If this so-called strong coupling condition is fulfilled, a high and a low energy solution for equation (28) are obtained, termed upper polariton (UP) and lower polariton (LP) (Figure 2.2b). Note that the condition in equation (29) is softened for inhomogeneously broadened excitons.⁷⁶

The separation between UP and LP at $E_C(\theta) = E_X$, is called Rabi splitting $\hbar\Omega_R$, here given for absorption:

$$\hbar\Omega_R = \sqrt{V^2 - \frac{1}{2}(\hbar\Gamma_C^2 + \hbar\Gamma^2)}. \quad (30)$$

The Rabi splitting can be experimentally determined by fitting equation (28) to experimentally observed UP and LP modes. For this fit, equation (30) has to be adapted for transmission, reflectivity or photoluminescence (PL). The respective expressions can be found in Savona *et al.*⁷⁵. However, for reflectivities well within the strong coupling regime, the splitting in absorption is approximately equal to the splitting in reflectivity,⁷⁵ which is why equation (30) is used to fit the data presented in this thesis.

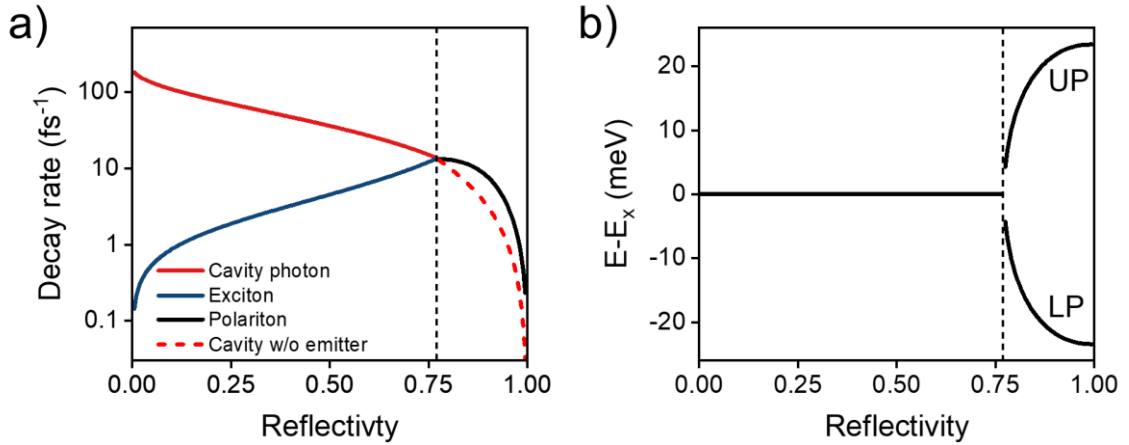


Figure 2.2 **a)** Cavity photon, exciton and polariton decay rates as a function of mirror reflectivity. The cavity photon decay rate for an empty cavity is given for comparison as a dashed line in the strong coupling regime. **b)** Mode splitting in absorption as a function of reflectivity. The gap between UP and LP mode at the onset of strong coupling equals $V = |\hbar\Gamma_X - \hbar\Gamma_C|/2$. The dashed line indicates the onset of strong coupling. The data was calculated using the SWCNT homogeneous linewidth $\hbar\Gamma_x^0 = 0.4$ meV and $n_{eff} = 2.08$.

UP and LP are mixed light-matter states and they are dispersive owing to $E_C(\theta)$, which is why they are also referred to as branches. Their respective photon (exciton) fractions α (β), also termed

Hopfield coefficients, can be calculated by projection of UP and LP onto the respective exciton $|X\rangle = \begin{pmatrix} 1 \\ 0 \end{pmatrix}$ and photon $|C\rangle = \begin{pmatrix} 0 \\ 1 \end{pmatrix}$ states by

$$\alpha_{UP/LP} = |\langle UP/LP|C\rangle|^2 \quad \text{and} \quad \beta_{UP/LP} = |\langle UP/LP|X\rangle|^2. \quad (31)$$

The description presented above can be readily extended to include multiple excitons and cavity modes, by extending the Hamiltonian given in equation (25). Furthermore, any kind of material excitation can be described, including non-emissive excitations, as long as the excitation exhibits a distinct resonance in the dielectric function⁷⁷ e.g., molecular emitters with vibronic replica⁷ or other quasi-particles such as trions⁴². Accordingly, the term exciton may occasionally be replaced with the more general term *oscillator*, representing any kind of vibrational or electronic excited state.

It is important to note, that the data presented in Figure 2.2 were calculated for an ideal case of cavity-emitter interaction, assuming a homogeneously broadened exciton without non-radiative decay channels. In real samples, more than one exciton (or molecule) is coupled to the cavity and the respective resonance may be inhomogeneously broadened. The properties of such systems are discussed in the next section.

2.2 Microcavity exciton-polaritons

This section introduces the spectroscopy of exciton-polaritons together with their potential applications. The discussion is focused on microcavity polaritons based on disordered excitonic systems and organic emitters in particular, as these systems exhibit important parallels to exciton-polaritons based on SWCNTs and are more closely related than work on inorganic polaritons in regard to sample properties. Examples for exciton-polaritons based on disordered materials are small organic molecules^{14, 78-81}, conjugated polymers^{15, 16}, fluorescent proteins^{17, 18}, J-aggregates^{57, 82} and random networks of single-walled carbon nanotubes^{40, 43}. The term exciton-polariton is commonly used to refer to strong coupling of electronic excitations, regardless of the specifics of the underlying emitter. This is owed to the fact, that the polariton-modes and conditions for strong

coupling in all cases are well described by the coupled oscillator model introduced in section 2.1.6. However, the observed photophysical properties of exciton-polaritons are connected to the underlying emitter, which is discussed in the following sections.

2.2.1 Exciton-polariton states

In practice, exciton-polaritons are created by coupling an ensemble of emitters to the light field, with the exception of single-molecule strong coupling. At room temperature, selecting a single emitter requires subwavelength mode volumes, which can only be achieved in plasmonic cavities.⁸³ Furthermore, the oscillator strength of a single emitter may be too small to reach the strong coupling regime.⁸⁴ For an ensemble of excitons, however, the matrix element V of equation (25) increases with number of excitons or oscillators N by

$$V_N = V\sqrt{N}, \quad (32)$$

where V_N is the coupling strength of the ensemble. In a full quantum electro-dynamical picture, expression (32) can be derived from the Tavis-Cummings model,⁸⁴ but it can also be derived classically from an inhomogeneously broadened resonance in the dielectric function.⁷⁷ For a strongly coupled ensemble, the system consists of $N + 1$ states, with one exciton and the photon mode forming the bright polariton states UP and LP, presented in the section 2.1.6. That leaves $N - 1$ degenerate states with the energy E_x called dark states, due to their small photonic component⁸⁵ (Figure 2.3a). It is important to note, that they still exhibit weak absorption,⁷⁷ indicating finite coupling to light. Together with high momentum states of the LP branch, which are not optically accessible with $k_{\parallel} > \frac{2\pi}{\lambda}$, they form the so-called exciton reservoir (Figure 2.3b). The reservoir population possesses the properties of the weakly coupled emitter, due to their small photon fraction. In case of disordered excitonic materials, a manifold of uncoupled states also exists due to emitters with misaligned dipoles.⁴³ For conventional organic microcavities in the linear regime, the bright state population is about 10^{-7} times smaller, than the reservoir states,

including dark states, high momentum states and uncoupled states. In the next section the interplay between these different states will be discussed.

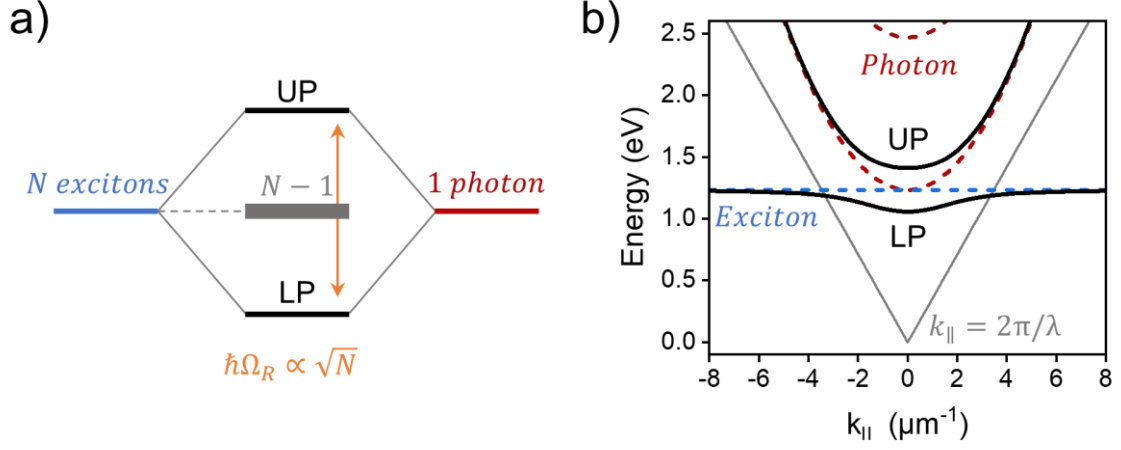


Figure 2.3 a) Schematic representation for coupling of an ensemble of excitons to a photon mode. b) Dispersion of UP and LP as a function of in-plane momentum. Exciton energy and photon modes are indicated by dashed lines. The boundary of the optical accessible part of the in-plane momentum is indicated by the grey line.

2.2.2 Exciton-polariton dynamics

The polariton dynamics are governed by the interaction between bright and dark states.⁵⁸ The polariton bright state lifetime $\tau_{UP/LP}$ depends on the cavity and the exciton lifetime according to

$$\tau_{UP/LP} = \alpha_{UP/LP}\tau_C + \beta_{UP/LP}\tau_{ex}, \quad (33)$$

where $\alpha_{UP/LP}$ and $\beta_{UP/LP}$ are the photon and exciton fraction, respectively. The bright state lifetime can be determined experimentally by measuring the polariton linewidth, which is broadened in comparison to the empty cavity by the exciton component. Note that τ_{ex} is the cavity reduced exciton radiative lifetime. Owing to the Hopfield coefficients $\alpha_{UP/LP}$ and $\beta_{UP/LP}$, the bright state lifetime has an angular dependence.⁸⁶ With bright state lifetimes ranging from 15 to 200 fs in organic microcavities, the angle-dependence may be obscured by the measurement accuracy.⁸⁷

The polariton dark states inherit the lifetime of the weakly coupled emitter and are non-adiabatically coupled to the polariton bright states.^{58, 88} The coupling efficiency is determined by the overlap between bright and dark states, where the density of dark states can be approximated by the absorption spectrum of the weakly coupled emitter.¹² Coupling to dark states connects the UP population to the LP population. If the cavity is tuned in resonance with the dark state or exciton energy, respectively, the LP population oscillates with the Rabi frequency Ω_R and produces a characteristic beating in the polariton decay.⁸⁹ Coupling to the dark states is also responsible for the fact, that polariton emission is predominantly observed from the LP.⁹⁰ Under resonant excitation, non-adiabatic coupling to dark states increases the experimentally observed polariton lifetime of the bright states.⁹¹⁻⁹³ Hence, the experimentally observed polariton fluorescence lifetime is always longer than the bright state lifetime given by equation (33). To stress this fact, the bright state polariton lifetime calculated by linewidth is referred to as polariton intrinsic lifetime in the following parts of this thesis. Apart from resonant excitation of the polariton bright states, polaritons can be injected off-resonantly by excitation of high energy emitter states. The latter excitation scheme reveals the influence of the emitter's photophysics on the polariton dynamics and population.

Under off-resonant excitation, the emitter first undergoes internal conversion (IC) to the lowest lying exciton or reservoir states, respectively (Figure 2.4a). From the exciton reservoir, three population mechanisms have been proposed:⁹⁴ Firstly, reservoir excitons can scatter with acoustic phonons in case of crystalline solids⁹⁵, or molecular translational vibrations in case of amorphous solids⁹⁶ (Figure 2.4 (i)). Secondly, reservoir excitons can scatter with optical phonons in case of atomic crystals⁹⁷, or intramolecular vibrations (vibrationally assisted scattering, VAS) in case of molecular materials⁹⁸⁻¹⁰⁰ (Figure 2.4 (ii)). Lastly, if the two former processes are slow compared to the reservoir excitons' radiative rate, the polaritons can be populated by reservoir excitons in their fluorescing state, which is termed radiative pumping⁸⁰ (Figure 2.4 (iii)). Formerly, radiative pumping was hypothesized to be emission of weakly coupled photons by the emitter, that are re-

absorbed by resonant polariton states. However, recent molecular dynamics simulations suggest, that this energy transfer is based on non-adiabatic coupling of the fluorescing state to the polaritons rather than a true emission event⁶⁶ (Figure 2.4b (iii)). This explains why for radiatively pumped polaritons, the photonic part of the polariton does not act *via* Purcell enhancement on the weakly coupled reservoir states, but the fluorescence lifetime of the uncoupled emitter is retained.^{57, 80, 92} Although, the term *radiative pumping* becomes somewhat misleading in this context, it will be used in this thesis to not confuse its relation to earlier studies.

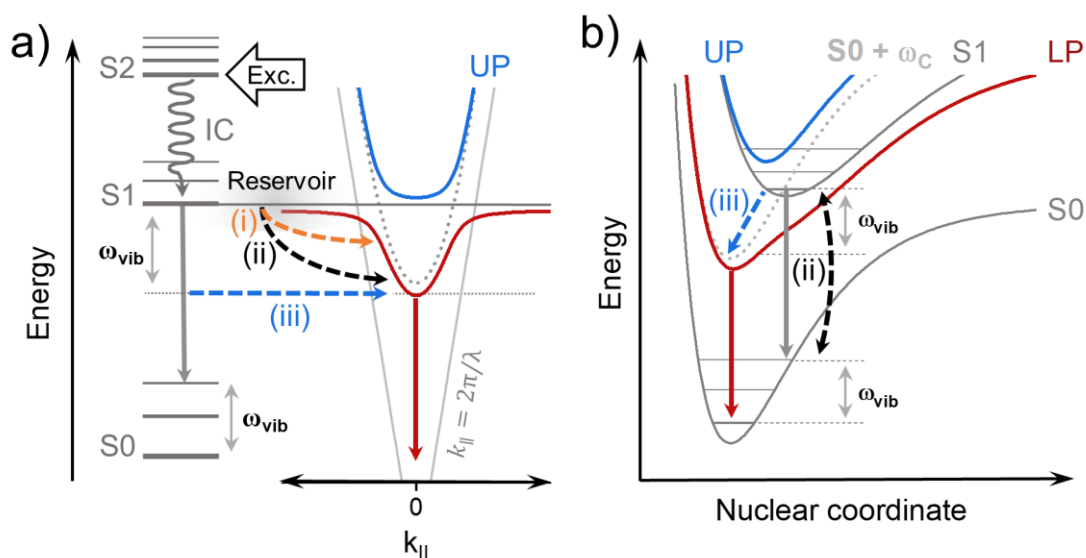


Figure 2.4 Polariton population mechanisms for organic exciton-polaritons with the lower polariton tuned to the second vibronic fluorescence replica. The colour grey indicates the weakly coupled emitter states, with the wavy arrow denoting internal conversion (IC) and straight arrows indicating molecular fluorescence. Dashed arrows indicate polariton population mechanisms, namely scattering with intermolecular vibrations (i, orange), scattering with intramolecular vibrations (ii, black) and radiative pumping (iii). The LP fluorescence is indicated as a red arrow. **a)** Polariton population from the reservoir states outside the light cone (light grey lines) into the LP. The cavity mode is indicated (dotted grey line). **b)** Schematic representation of the energy levels in (a) on the molecular level. The cavity mode is replaced by the ground states raised by the energy of the cavity photon $\hbar\omega_c$ at $k_{||} = 0$ (dotted grey line).⁸⁴ Scattering with an intramolecular vibration is indicated by a black curved arrow and non-adiabatic energy transfer (radiative pumping) is indicated as a blue dashed arrow. LP and molecular fluorescence are given for comparison.

All three population processes, that is scattering inter- and intramolecular vibrations, as well as radiative pumping, are significantly slower than the intrinsic polariton lifetime and can be considered rate limiting for the polariton population. Especially for organic polaritons, the short intrinsic polariton lifetime inhibits polariton relaxation along the LP branch to the zero inplane momentum ($k_{\parallel} = 0$) LP ground state.⁹⁴ Therefore, population distribution along the LP branch arises purely from direct population of the LP states and population maxima cannot be interpreted as so-called relaxation bottlenecks, as was done in earlier studies.^{15, 40, 101} However, if the LP($k_{\parallel} = 0$) state is tuned to a population maximum, the population rate can be faster than the intrinsic polariton decay under high excitation densities, leading to an accumulation of polaritons in the LP ground state.¹⁰² In this regime, population into the LP ground state is believed to be facilitated by bosonic relaxation, also referred to as stimulated-scattering, leading to a superlinear increase of the polariton population above the accumulation threshold. Such a situation is termed polariton condensation. The condensate is a single, macroscopically occupied quantum state and hence its decay leads to coherent emission from the cavity with a super linear power dependence. Accordingly, this phenomenon is termed polariton lasing and is related to Bose-Einstein condensation.⁶ Even though, polariton condensation was observed for a range of organic materials, such as small organic molecules,^{7, 13, 14} conjugated polymers^{15, 16} and fluorescent proteins^{17, 18}, the specific material properties required to reach the condensation threshold remain elusive. Some authors claim that the photoluminescence quantum yield (PLQY) in combination with radiative pumping is crucial,^{79, 80} while others argue that vibrationally assisted scattering is required to overcome the condensation threshold.^{23, 100} This thesis aims to elucidate this question for single-walled carbon nanotubes and to investigate the validity of the aforementioned concepts for exciton-polaritons based on low dimensional, disordered semiconductors.

2.3 Single-walled carbon nanotubes

Single-walled carbon nanotubes (SWCNTs) possess rich photophysics, which are distinct from organic as well as inorganic emitters. The SWCNT geometric and electronic structure can be

derived from a rolled-up sheet of graphene. Depending on the roll-up or chirality vector, given in terms of integer multiples (n, m) of the primitive graphene lattice vectors, carbon nanotubes can be either metallic or semiconducting.¹⁰³ Nanotubes exhibit a prototypical one-dimensional band structure with characteristic van Hove singularities and a bandgap inversely proportional to the SWCNT diameter.¹⁰⁴

This work focuses on the semiconducting (6,5) chirality, which can be readily isolated in large quantities and high purity by selective polymer-wrapping by PFO-BPy [(9,9-dioctylfluorenyl-2,7-diyl)-alt-co-(6,6'-(2,2'-bipyridine))] from mixed nanotube raw material using shear force mixing.¹⁰⁵ The following subsections present photophysical properties of nanotubes with respect to (6,5) SWCNTs, their manipulation by chemical functionalization and concludes with the previous work on SWCNT exciton-polaritons.

2.3.1 SWCNT optical properties

Due to the one-dimensional SWCNT structure, electrons and holes are strongly correlated in nanotubes, giving rise to excitons with large binding energies (200-400 meV)^{106, 107} and narrow linewidths at RT (10-15 meV)¹⁰⁸, that dominate their absorption and emission spectra. Even in densely packed SWCNT films the RT linewidth remains below 100 meV¹⁰⁹. Nanotube excitons are commonly labelled with respect to the transition between the corresponding van Hove singularities, that is E_{11} , E_{22} and so forth. For (6,5) nanotubes (Figure 2.5a), the E_{22} transition is about 2.15 eV (576 nm) and the E_{11} transition is about 1.23 eV (1005 nm) in thin films of random SWCNT networks. Due to fast internal relaxation from higher excitons to the E_{11} state ($E_{22} \rightarrow E_{11} \sim 100$ fs)¹¹⁰ emission is exclusively observed from the E_{11} exciton in the NIR.

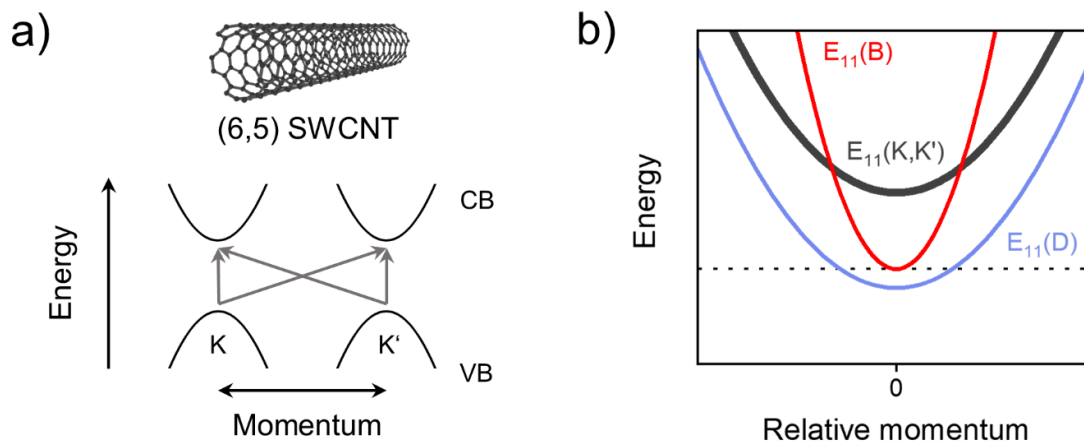


Figure 2.5 a) Schematic representation of the (6,5) SWCNT single electron-hole pair transitions. b) Schematic representation of the SWCNT singlet exciton energy levels as function of relative momentum as described by Perebeinos *et al.*¹¹¹ The dotted line highlights the minimum of the bright exciton dispersion.

Owing to their graphene lattice, SWCNTs exhibit a valley structure with a doubly degenerate valence and conduction band (VB and CB, Figure 2.5a). Accordingly, there are four distinct electron-hole pair excitations, each comprising one singlet and three triplet configurations leading to a total of 16 excitons. Coulomb interactions lift the degeneracy between excitons of different parity and momentum and singlet-triplet exchange splitting lifts their spin-degeneracy.¹¹¹ Due to the weak spin-orbit coupling in SWCNTs, all triplet excitons are dark. They may be detected under external magnetic fields or in the long-lived fluorescence under low repetition, pulsed excitation.¹¹²⁻¹¹⁶

The following focusses on the singlet exciton manifold. The dark even parity exciton $E_{11}(D)$ is lowest in energy (Figure 2.5b), hence, radiative recombination is inhibited at thermal energies below the even-odd parity splitting.^{111, 117} Next in energy is the bright odd parity exciton, giving rise to the fundamental E_{11} transition (Figure 2.5b). Above the odd parity exciton lay the two, degenerate momentum-forbidden excitons $E_{11}(K)$, which are partially allowed by coupling with the so-called D_0 phonon giving rise to a phonon sideband in absorption (Figure 2.6b).^{118, 119} The

exciton dispersion is parabolic close to the band minimum, with the $E_{11}(B)$ exciton dispersion being distorted by large exchange energy (Figure 2.6b).¹¹¹

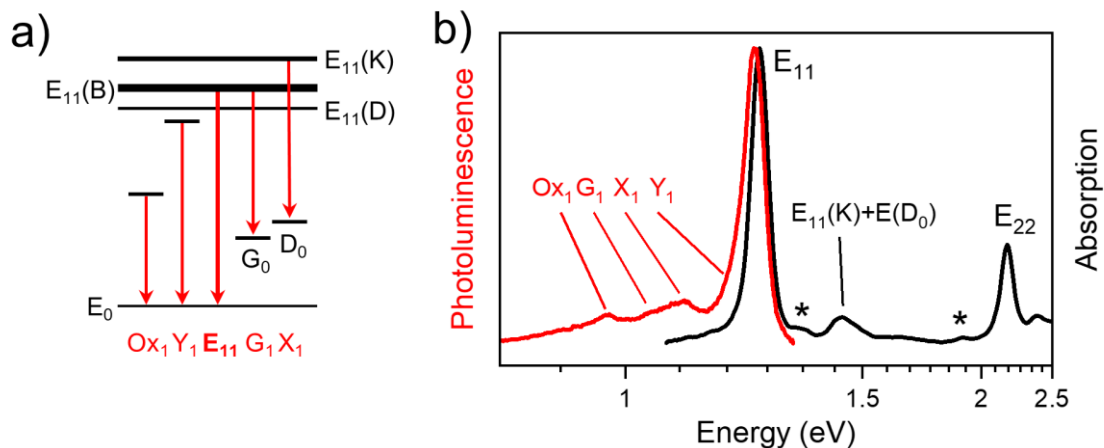


Figure 2.6 a) Schematic representation of luminescent (6,5) SWCNT transitions. The PL band notation is given in red. **b)** PL (red) and absorption spectrum (black) of (6,5) SWCNT in a polymer matrix. Impurities of other chiralities are indicated by an asterisk.

Apart from the fundamental E_{11} transition, a series of weak, red-shifted peaks are observed in the (6,5) SWCNT emission spectrum. These peaks will be referred to as photoluminescence side bands (PSBs) and are shown in Figure 2.6. The G_1 transition arises from decay of the $E_{11}(B)$ states under emission of a G_0 phonon,¹²⁰ whereas the X_1 transition originates from decay of the partially allowed $E_{11}(K)$ exciton.^{120, 121} The Y_1 transition is believed to be of extrinsic origin as it shows tube-to-tube variations.¹²² The Ox transition shows batch-to-batch variations and might be connected to unintentional luminescent oxygen defects.¹²³ In this work, the Ox transition is observed for samples that were prepared under ambient conditions.

2.3.2 SWCNT exciton dynamics

The SWCNT exciton dynamics are dominated by the interplay between their one-dimensional properties, that is their transport and diffusion properties, and the zero-dimensional or molecular-like behaviour of their strongly-bound excitons.¹¹⁰ From this, a plethora of short and long-lived species arise, with the most prominent ones depicted in Figure 2.7a. After generation, excitons may dissociate into free carriers¹²⁴ or diffuse up to a few hundred nanometres along the nanotube¹²⁵. Due to the aforementioned fast internal relaxation, diffusion is only relevant for the E_{11} exciton.¹¹⁰ Its lifetime is limited by diffusive quenching at the nanotube ends or non-radiative defects.¹²⁶⁻¹²⁸ At higher excitation densities, the quenching rate is increased by exciton-exciton annihilation via an Auger-type mechanism¹²⁹⁻¹³¹ with a cubic dependence on the exciton density in defect free nanotubes¹³². The carrier generation efficiency increases with the energy of the excited exciton ($E_{11} < E_{22} < E_{33}$)¹³³ and depends on pump fluence, wrapping polymer and dielectric environment.^{55, 133} The photocarriers may form bound states with excitons, termed trions,^{53, 134, 135} or with the nanotube lattice, termed polarons¹³⁶⁻¹³⁸, leading to characteristic signatures in SWCNT transient spectra. However, in PFO-BPy wrapped SWCNTs these signatures are much weaker or even absent, due to less efficient charge carrier generation.⁵⁵ In this system, significant trion features are only observed upon chemical⁵⁵ or electrical doping⁵⁴ and polaron features may be observed under excitation of higher excitons at increased pump fluences.⁵⁵

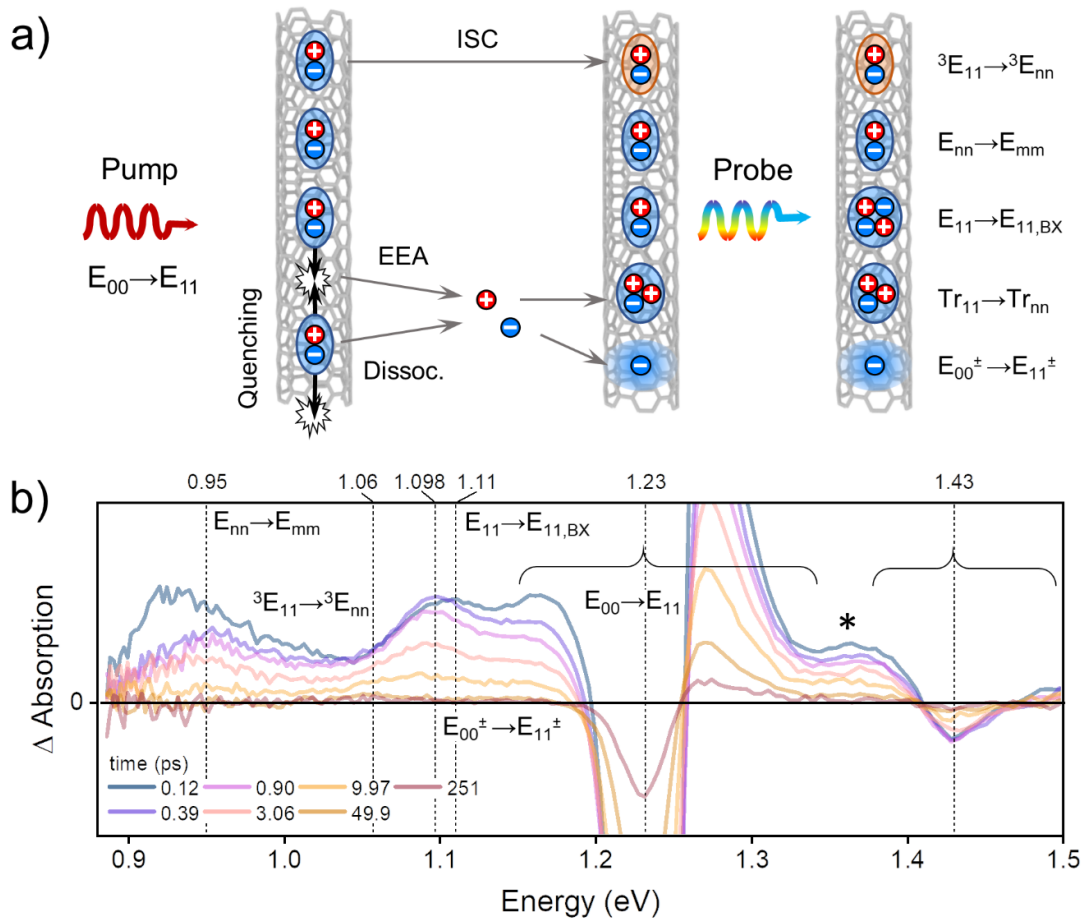


Figure 2.7 a) Schematic illustration of the excited state processes in SWCNTs. In PFO-BPy wrapped (6,5) SWCNTs, the amount of photoinduced charges and the concomitant species are strongly reduced, as is the triplet generation in film. **b)** Typical transient absorption spectrum for E_{22} excitation of (6,5) SWCNTs in a PFO-BPy matrix with the transitions of (a) indicated (dashed lines). The asterisk denotes the (9,1) impurity.

In the following, the dominant transient features of (6,5) SWCNTs in a PFO-BPy matrix will be discussed and are shown in Figure 2.7b. The peak assignment follows previous observations made for semiconducting SWCNTs in liquid samples and gelatine matrices. The discussed transitions in solid films relate to those observed for liquid samples of PFO-BPy wrapped SWCNTs in tetrahydrofuran⁵⁵ by a consistent red-shift of 10-20 meV. All NIR transient SWCNT absorption spectra are dominated by the ground state bleach of the $E_{00} \rightarrow E_{11}$ transition (Figure 2.7b)^{55, 138} persisting up to hundreds of picoseconds, likely due to carrier induced bleaching.⁵³ The ground state bleach (GSB) features a strong photoinduced absorption at its blue and red flanks, which

arise from a red-shift of the E_{11} absorption during excitation¹³⁹, supposedly due to carrier induced lattice deformations.¹³⁷ The high intensity of the blue flank was also attributed to transitions from the even parity dark exciton $E_{11}(D)$ into the two exciton manifold.¹⁴⁰ Hence, the full picture remains to be clarified conclusively.^{129, 137, 139-141} The photoinduced bleach of the $E_{11}(K)+E(D_0)$ phonon sideband (Figure 2.7b, 1.43 eV) approximately follows the GSB behaviour. Apart from the features mentioned above, the SWCNT transient absorption spectra exhibit sample specific features, such as the absorption band around 1.35 eV (Figure 2.7b, asterisk), caused by a (9,1) SWCNT impurity present in PFO-BPy-selected SWCNTs.

Regarding the transient products, SWCNT prominently feature generation of biexcitons (BX), a bound state of two excitons analogous to molecular hydrogen. The $E_{11} \rightarrow E_{11,BX}$ transition occurs about 110 meV below the GSB (Figure 2.7b),^{53, 134} exhibiting a red-shift following the $E_{00} \rightarrow E_{11}$ transition. SWCNT biexcitons can be created resonantly, which indicates, that their formation involves defects or deformations, allowing this otherwise forbidden transition.¹³⁴ Biexcitons annihilate by coupling to the electron-hole continuum of the respective exciton with a lifetime of about 60 fs in SWCNTs.¹³⁴ The decay of their transient signal, however, follows the exciton population and is long-lived.⁵³ The biexciton signal may exhibit a red shoulder after a few picoseconds (Figure 2.7b) which is attributed to polaron generation assisted by the PFO-BPy wrapping polymer⁵⁵ and depends on the number of induced carriers. Despite the fast intersystem-crossing (ISC) in SWCNT (~ 20 ps)¹⁴², the triplet exciton ${}^3E_{11} \rightarrow {}^3E_{mn}$ transition is weak for PFO-BPy wrapped SWCNTs⁵⁵ and virtually absent in films (Figure 2.7 b, ~ 1.06 eV). The remaining prominent photoinduced absorption is attributed to higher exciton transitions $E_{nn} \rightarrow E_{mnn}$ ^{133, 136, 138, 143} and decays within about 10 ps (Figure 2.7b, ~ 0.95 eV). Radiative recombination of excitons plays a negligible role in the transient absorption features of SWCNTs due to the fast non-radiative processes discussed before⁵³ and there is no report of stimulated emission signatures.

Radiative recombination of excitons in SWCNT has to be investigated separately in time-dependent luminescence experiments. The odd parity bright singlet exciton $E_{11}(B)$ exhibits a

biexponential fluorescence decay. The short lifetime component has been attributed to decay through radiative and non-radiative channels, followed by a slower decay attributed to population exchange with the long lived dark excitons.^{125, 144} Under off-resonant excitation, the SWCNT PL sidebands also exhibit this biexponential behavior but with longer lifetime components. This is in agreement with the sideband origins discussed in the previous section (Figure 2.6, PSB), connecting the sideband emission directly or indirectly (in case of the $E_{11}(K)$ -related X_1 band) to the $E_{11}(B)$ population. For very short nanotubes or high defect densities, the fluorescence decay becomes monoexponential and the influence of dark-bright exciton redistribution vanishes.¹⁴⁴ In long, defect free nanotubes, the dark exciton lifetime (> 2.4 ns) is still diffusion limited, with conversion efficiencies to the $E_{11}(B)$ state of up to 50%.¹²⁵ Hence, in both regimes, the SWCNT PLQY is governed by diffusive quenching (< 0.2 % in (6,5) SWCNT thin films).¹²⁶ However, not all nanotube defects lead to quenching and some may exhibit bright PL, such as specific oxygen defects mentioned in connection with the PL sidebands.¹²³ Recently, synthetic methods have been developed to introduce luminescent defect configurations, that trap mobile excitons and facilitate radiative recombination. This is discussed in the next section.

2.3.3 Luminescent sp^3 defects

Luminescent sp^3 defects, also referred to as organic colour centres or quantum defects,¹⁴⁵ are able to trap mobile excitons and serve as radiative recombination sites, leading to red shifted emission in the NIR with substantially increased PLQY (2-8 fold).^{49, 50} These defects may be introduced synthetically *via* various chemical reactions¹⁴⁶ and their properties depend on defect density⁵⁰, the introduced functional group¹⁴⁷ and on the defect binding configuration¹⁴⁸. Upon functionalization, two sp^3 hybridized carbon atoms are created within the sp^2 hybridized nanotube lattice, distorting the energetic landscape of the nanotube and creating excitonic trap states on the order of 100 meV below the E_{11} exciton (Figure 2.8a).¹⁴⁹ With regard to their binding configuration, two main types of defects have been identified, commonly termed E_{11}^* (emission peak at 1.05 eV or 1180 nm) and E_{11}^{*-} (emission peak at 0.95 eV or 1300 nm) in case of (6,5) nanotubes (Figure 2.8b). The

defects efficiently trap mobile excitons already at low densities ($\sim 1 \mu\text{m}^{-1}$) and increase the SWCNT PLQY mainly by preventing diffusive quenching at non-radiative defects.^{50, 150} However, high sp^3 defect densities ($> 14 \mu\text{m}^{-1}$) reduce the PLQY, due to disruption of the nanotube lattice.^{50, 150} At optimum densities for PFO-BPy wrapped (6,5) SWCNTs ($\sim 8 \mu\text{m}^{-1}$) the PLQY is increased to about 4 %, with about 90 % of emission from the defect states.⁵⁰

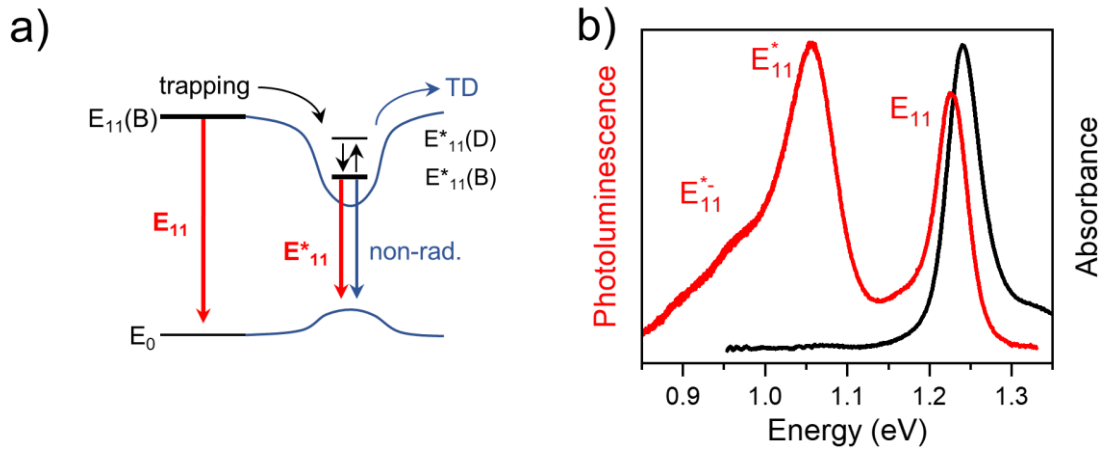


Figure 2.8 a) Schematic depiction of the defect states and recombination dynamics. Red arrows indicate radiative decay and blue arrows indicate non-radiative deactivation. Trapping of diffusing excitons and equilibration between defect dark and bright states is denoted by black arrows. b) PL (red) and absorption spectrum (black) of sp^3 -functionalized (6,5) SWCNTs in a polymer matrix.

Although, luminescent sp^3 defects possess radiative lifetimes similar to the mobile SWCNT excitons on the order of 1-10 ns^{111, 151, 152}, their fluorescence lifetimes are prolonged compared to pristine SWCNTs, owing to their reduced non-radiative decay.^{153, 154} The dominant non-radiative decay channel in sp^3 defects in non-polar environments at low temperatures is multi-phonon decay (MPD).¹⁵³ At higher temperatures, thermal de-trapping (TD) becomes relevant, explaining the longer lifetime of more red-shifted defect configurations, that correspond to deeper trap states.¹⁴⁹ Together, they dominate the exciton relaxation at room temperature

$$\frac{1}{\tau_{relax}} = \frac{1}{\tau_{TD}} + \frac{1}{\tau_{MPD}} + k_{other}, \quad (34)$$

where k_{other} refers to any quantitative deviation between equation (34) and the experimentally obtained decay. For samples with shorter lifetimes, such as polymer-embedded networks of SWCNTs (100-200 ps), k_{other} is dominated by additional non-radiative deactivation channels such as interaction with the polymer matrix¹⁵⁵. In liquid samples of non-polar solvents, longer lifetimes are observed (100-500 ps), indicating a higher contribution of slow, radiative recombination.¹⁵³ In analogy to pristine SWCNTs, sp^3 defects exhibit a biexponential fluorescence decay, which is as well attributed to the presence of various defect dark states energetically close to a single bright defect state.¹⁵⁴ The short lifetime component is believed to contain the aforementioned exciton relaxation channels and the redistribution between bright and dark states τ_{BD} ¹⁵³

$$\frac{1}{\tau_{short}} = \frac{1}{\tau_{BD}} + \frac{1}{\tau_{relax}} \approx \frac{1}{\tau_{BD}} + \frac{1}{\tau_{non-rad}}, \quad (35)$$

assuming that the same relaxation channels apply to bright and dark states. This assumption is valid if the non-radiative decay is significantly faster than the radiative decay. The long lifetime component represents the pure exciton relaxation ($\frac{1}{\tau_{relax}} < \frac{1}{\tau_{BD}} + \frac{1}{\tau_{relax}}$), without redistribution, that is through radiative and non-radiative channels^{153, 154}

$$\frac{1}{\tau_{long}} \approx \frac{1}{\tau_{relax}} = \frac{1}{\tau_{non-rad}} + \frac{1}{\tau_{rad}} = \frac{1}{\tau_{TD}} + \frac{1}{\tau_{MPD}} + k_{other}. \quad (36)$$

Accordingly, the contribution of radiative recombination is higher than for the short component. In contrast to pristine nanotubes, the defect bright state is lowest in energy. Hence, at thermal energies below the gap between bright and dark states, the fluorescence decay becomes mono-exponential.^{156, 157}

2.3.4 Strong coupling with SWCNT

Over the last few years, semiconducting single-walled carbon nanotubes have emerged as an excellent material for strong coupling in the near infrared (NIR) owing to their unique

photophysical properties described above. SWCNT exciton-polariton can be readily created in metalclad cavities containing dense random networks of SWCNTs in a polymer matrix.⁴⁰ Additionally, their high ambipolar charge transport enables electrical injection of polaritons.⁴¹ Their large oscillator strength E_{11} excitons facilitate strong coupling in plasmonic lattices^{44, 45} and reaching the ultrastrong coupling regime.⁵⁶ When using pure films of aligned SWCNTs, even the weaker E_{22} transition can be ultrastrongly coupled.⁴³ In high density SWCNT films (~ 40 wt%⁵⁶), the absorption phonon-sideband of the momentum-forbidden dark $E_{11}(K)$ (section 2.3.1) is strongly coupled as well^{42, 56}, leading to cavity-mediated hybridization between bright and dark excitons.⁵⁶ However, the effect of this hybridization on the polariton PLQY remains elusive.⁵⁶ Upon electrochemical doping of cavity-embedded, strongly coupled SWCNTs, the emergence of SWCNT trion-polaritons was observed.⁴² Yet, interaction of SWCNT exciton-polaritons with biexcitons and luminescent defects had not been investigated at the beginning of this thesis. Furthermore, there exists little knowledge of the population mechanism of SWCNT exciton-polaritons, a subject which is crucial in regard to application in devices as well as to polariton condensation. In the results part of this thesis, these open questions are addressed.

2.4 Organic photodiodes

Organic photodetectors are an interesting alternative to conventional inorganic photodetectors due to their wavelength tunability, low-cost manufacturing and compatibility with lightweight, flexible devices, despite their commonly inferior device performance in comparison with their inorganic counterparts.¹⁵⁸ Photodetectors may be created from phototransistors, photoconductors or photodiodes.¹⁵⁹ The following discussion focuses on photodiodes as it serves as basis for the strongly coupled photodiodes presented in Chapter 6.

Due to the typically large exciton binding energies found for organic materials, spontaneous exciton dissociation into electrons and holes is inhibited for most materials, with a few exceptions such as polythiophene derivatives.¹⁵⁹ This inhibition can be overcome by employing an electron-donating material (D) and an electron-accepting material (A). Donor-acceptor (DA) pairs can be selected by choosing materials with low ionization potential for D and high electron affinity for A. Given that the lowest unoccupied molecular orbital (LUMO) of the acceptor is higher in energy, than the highest unoccupied molecular orbital (HOMO) of the donor, excitons can be dissociated at the DA-interface. Figure 2.9a depicts photoinduced electron transfer from the HOMO of D to the HOMO of A for photoabsorption of A. If a photon of lower energy is absorbed by D, electron transfer can occur from the LUMO of D to the LUMO of A (not depicted). Prior to dissociation into free charges, a charge transfer (CT) state is formed (Figure 2.9b) with the hole occupying the HOMO of D and the electron occupying the LUMO of A. Consequently, less strongly bound CT states facilitate exciton dissociation into charge carriers.¹⁶⁰ In DA systems, the interface for exciton dissociation can be increased by blending of the D and A phases, whereas charge carrier extraction is facilitated by continuous D and A phases (Figure 2.9b). Accordingly, the morphology of the DA system is crucial, with DA blends commonly achieving better device performances for optimized morphologies.¹⁶¹ An active layer with a homogeneous D and A phase is termed flat heterojunction (FHJ), whereas intermixed D and A phases are referred to as bulk heterojunctions (BHJ).

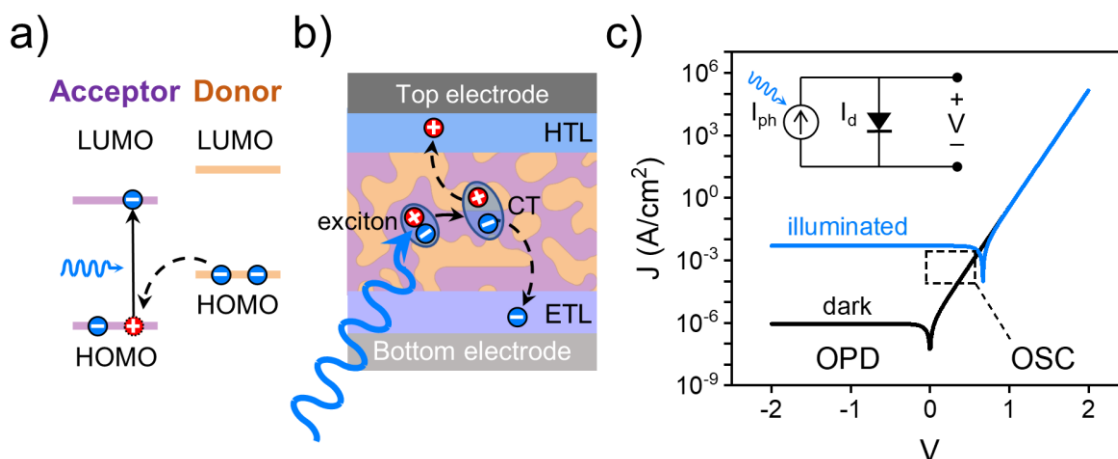


Figure 2.9 a) Photoinduced electron transfer from the HOMO of D to the HOMO of A. b) Device schematic of a BHJ photodiode with hole and electron transport layers (HTL and ETL) and reflective top and transparent bottom electrode. Exciton generation (blue wavy arrow), diffusion (black solid arrow), CT state dissociation and carrier extraction (black dashed arrows) are indicated. c) Idealized current density-voltage (JV) curve of a photodiode in the dark and under illumination. The current density of the diode is calculated using the Shockley equation. For illumination a current source is added in parallel to the diode.¹⁶² OPD and OSC operation regimes are indicated.

Photodiodes are two terminal devices with commonly vertical topology, that is, the active medium is sandwiched between the contacts (Figure 2.9b).¹⁵⁹ The contacts may be metallic, with the bottom contact being transparent and hence often replaced by a conductive oxide to increase light in-coupling. In addition, charge transport or blocking layers may be used to either improve charge extraction or block charges of opposite sign, depending on the specific energy level alignment for a given D-A-electrode combination. Depending on diode operation, the device may be considered a solar cell, that is for forward bias operation below the open circuit voltage (Figure 2.9c, dashed square), or a photodetector, that is for zero or reverse bias operation (Figure 2.9c).¹⁶³ The area indicated in Figure 2.9c (dashed square) corresponds to the maximum power extractable from the solar cell.¹⁶² The minimum of the current density curve corresponds to the open circuit voltage. Increasing the open circuit voltage increases the solar cell power conversion and can be achieved by large HOMO(D)-LUMO(A) gaps¹⁶⁰ or a steep absorption edge (low Urbach energy)¹⁶⁴.

Depending on the photodetector application, various figures of merit may be of importance. Here, the discussion shall be limited to the most fundamental two, that is the external quantum efficiency (EQE) and the specific detectivity (D^*). The EQE describes the ratio between collected charge carriers ($n_{carriers}$) and incident photons ($n_{photons}$) of a device and is often given as the spectral responsivity $\mathcal{R}(\lambda)$ ¹⁶³

$$EQE = \frac{n_{carriers}}{n_{photons}} = \frac{hc}{e\lambda} \mathcal{R}(\lambda), \quad (37)$$

where e is the elementary charge. The efficiency depends on the morphology and thickness of active and charge transport layers, the absorption and recombination losses within these layers and the in-coupling efficiency of the incident light field. The internal quantum efficiency (IQE) describes the efficiency of photocarrier generation in terms of absorbed photons, that is, the EQE corrected for reflection (R) and transmission (T) of the device

$$IQE = \frac{n_{carriers}}{n_{photons,abs.}} = \frac{EQE}{1 - R - T}. \quad (38)$$

As all electronic devices, OPDs are subject to noise, which limits the detection at low light intensities. The total spectral noise density $S_{noise}(f)$ is given by¹⁶³

$$S_{noise}(f) = \sqrt{S_{shot}^2 + S_{thermal}^2 + S_{1/f}^2}, \quad (39)$$

where S_{shot}^2 is the shot noise, arising from the discreteness of electric charges and increases with dark current i_{dark} $S_{shot}^2 = \sqrt{2ei_{dark}}$. The thermal noise $S_{thermal}^2$ arises from thermal excitation of carriers, especially in case of low shunt resistance $S_{shot}^2 \propto \sqrt{R_{shunt}^{-1}}$. The $1/f$ -noise $S_{1/f}^2$ may have different origins, but mostly arises from carrier recombination, which increases for lower electrical frequencies $S_{1/f}^2 \propto 1/f$. The specific detectivity $D^*(\lambda, f)$ accounts for the total spectral noise density $S_{noise}(f)$ at a given responsivity $\mathcal{R}(\lambda)$ and is normalized to the device active area A_{active} for better comparison between different devices (note that absorption is referred to as A

in this thesis). For organic photodiodes (OPDs), the shot noise is commonly the dominant noise source and hence $D^*(\lambda, f)$ depends strongly on the dark current density with $J_{dark}^{-1/2}$ ¹⁵⁹

$$D^*(\lambda, f) = \frac{\mathcal{R}(\lambda)\sqrt{A_{active}}}{S_{noise}(f)} \stackrel{OPD}{\approx} \frac{\mathcal{R}(\lambda)}{\sqrt{2eJ_{dark}}} \quad (40)$$

D^* is given in Jones ($\text{cm Hz}^{1/2}\text{W}^{-1}$) and yields the signal to noise ratio for a 1 W signal of 1 cm^2 active area measured at 1 Hz electrical bandwidth. Reduction of the dark current is therefore of special importance for OPDs.

State-of-the-art OPDs exhibit EQEs about 20-50 % and specific detectivities up to 10^{13} Jones in the visible spectral range¹⁵⁸, however, the EQE drops dramatically beyond 800 nm¹⁶³. As the NIR spectral range is relevant for applications in optical communication, environmental monitoring, biomedical imaging and sensing¹⁵⁸, improving the NIR performance of OPDs is of special interest.^{158, 159} One approach is to employ hybrid OPDs containing nanomaterials such as colloidal quantum dots (50 % EQE with up to 10^9 Jones)^{158, 165} or SWCNTs (2 % EQE with up to 10^{10} Jones)^{166, 167}. Another approach is to convert the photodiode device structure into a microcavity, by increasing the reflectivity of semi-transparent electrode.¹⁶⁸ The resulting cavity enhanced absorption increases the EQE in spectral areas, where the active medium has only low absorption.^{169, 170} By this approach EQEs of about 25 % and specific detectivities up to 10^{13} Jones could be achieved for polymer-fullerene OPDs in the spectral range below 1000 nm. The same approach can be used to strongly-couple the active medium of a photodiode.^{25, 26} For a strongly coupled phthalocyanine-fullerene OPD, an EQE of 0.5 % above 1000 nm could be demonstrated.²⁵ Hence, employing strongly coupled SWCNT-OPDs is a promising approach to create NIR photodetectors. This concept is demonstrated in Chapter 6.

The next chapter proceeds with describing the experimental methods used to prepare the samples and devices introduced in this chapter and to address the open questions on SWCNT exciton-polaritons.

3 Experimental methods

This chapter describes the experimental techniques used in this thesis and explains the data analysis and simulation software.

3.1 Sample preparation

3.1.1 SWNT dispersions

Selective Dispersion of (6,5) SWCNTs

Monochiral (6,5) SWCNTs were selectively extracted from CoMoCAT raw material (Chasm Advanced Materials, SG65i, 0.38 g/L) by shear force mixing (Silverson L2/Air, 10 230 rpm, 72 h) and polymer-wrapping with PFO-BPy (poly[(9,9-dioctylfluorenyl-2,7-diyl)-alt-co-(6,6'-(2,2'-bipyridine))], American Dye Source, $M_w = 40$ kg/mol, 0.5 g/L) in toluene.¹⁰⁵ Aggregates were removed by centrifugation at 60,000g (Beckman Coulter Avanti J26XP centrifuge) for 2×45 min with intermediate supernatant extraction. For the experiments described in Chapter 4, the resulting dispersion was split into two parts, one for the pristine SWCNT samples and one for sp^3 functionalization. The employed lots of SG65i were L58 (distributed by Chasm Advanced Materials) and MKCJ7287 (distributed by Sigma Aldrich). The employed lots of PFO-BPy for polymer-wrapping were #15L007A1, #16D008A1, #18H004A1 and #21AO11A1.

Functionalization of (6,5) SWCNT

The functionalization of polymer-wrapped (6,5) SWCNT was performed after Berger *et al.*⁵⁰ For functionalization, a toluene solution of 18-crown-6 (99%, Sigma-Aldrich) was added to the as-prepared polymer-sorted (6,5) SWCNT dispersion. Subsequently, a solution of 4-bromobenzenediazonium tetrafluoroborate (96 %, Sigma-Aldrich) in acetonitrile was added. The amounts were chosen such that the mixture contained 0.36 mg/L of (6,5) SWCNT (corresponding

to an E_{11} absorbance of 0.2 for 1 cm path length), 7.6 mmol/L of 18-crown-6 and 0.369 mmol/L of the diazonium salt in an 80:20 vol-% toluene/acetonitrile solvent mixture. The reaction mixture was left at room temperature in the dark for 16 hours without stirring. Afterwards, the reaction mixture was passed through a PTFE membrane filter (Merck Millipore, JVWP, 0.1 μm pore size) to collect the SWCNTs. The filter cake was washed with acetonitrile and toluene to remove any unreacted diazonium salt and excess polymer.

P3HT:PC₇₀BM:(6,5) SWCNT blends

For bulk heterojunction blends, the (6,5) SWCNT dispersion was passed through a PTFE membrane filter (Merck Millipore, JVWP, 0.1 μm pore size). The resulting filter cake was washed twice with toluene for 10 min at 80 °C to reduce the PFO-BPy content. The SWCNTs were re-dispersed to 0.5 g/L in chlorobenzene (99 %, Merck) and 100 μL were added to 450 μL of a 3.5 g/L solution of regio-regular poly(3-hexylthiophene-2,5-diyl) (P3HT, BASF SE, $M_w = 64$ kg/mol) in chlorobenzene and sonicated until homogeneous (~ 2 h) resulting in a wrapping polymer exchange. To this dispersion, 450 μL of a [6,6]-Phenyl-C₇₁-butyric acid methyl ester (PC70BM > 99 %, Lumtec) were added with a concentration of 4.5 g/L, followed by 10 min of sonication. For all sonication steps, the bath (Branson 2800 MH Ultrasonic Cleaner) was actively cooled to remain around room temperature. The resulting blend had approximately a 3:4 P3HT/PC₇₀BM-ratio with 1.4 wt% SWCNT.

3.1.2 Film preparation

PFO-BPy matrix

For solid PFO-BPy matrices, the polymer batch was tested for suitable film formation, as it is synthesized on laboratory scale. Material supplied by American Dye Source Inc. shows high batch-to-batch variation and was polydisperse. The batches #14B031A1 and #12JU27C1 were found to yield smooth films (1.3-2.8 RMS roughness) for spin-speeds below 1500 rpm at (20 g/L). Other lots showed signatures of phase separation possibly due to two different molecular

weight species. Hence, the PFO-BPy for SWCNT selection had to be removed before film preparation and replaced with either #14B031A1 and #12JU27C1.

Pristine and functionalized SWNT

To deposit pristine or functionalized SWCNT in a PFO-BPy matrix, the as-prepared dispersion was passed through a membrane filter (Merck Millipore, JWVP, 0.1 μm pore size or VSWP, 0.1 μm pore size) and the filter cake was washed with toluene. Afterwards, the SWCNT filter cake was manually peeled off the membrane. Note that for pristine or functionalized samples, the filter cake needs to contain at least 100 μg SWCNT (based on absorbance and filtered volume of the respective dispersion) to form stable films. The filter cakes were transferred into a 5 mL round bottom flask and washed three times with toluene at 80 $^{\circ}\text{C}$ for 15 min to ensure sufficient removal of free wrapping polymer. Subsequently, 0.8 mL of a 2 g/L PFO-BPy solution were added and the mixture was sonicated for 1 hour. Afterwards, 0.2 mL toluene was added in 50 μL steps each followed by 15 min of sonication until a homogeneous liquid with a honey-like viscosity was obtained. The number of dilution steps varied for different SWCNT batches. During sonication, the bath temperature was kept between 10-20 $^{\circ}\text{C}$ to avoid unwrapping of PFO-BPy. The final dispersions were allowed to warm up to room temperature prior to deposition by spin-coating. For high SWCNT concentrations ($> 1 \text{ wt}\%$), the film thickness and homogeneity was found to vary strongly for different SWCNT batches, hence, the film properties were always checked on a reference substrate by profilometry and optical microscopy, before film deposition.

3.1.3 SWCNT microcavities

For microcavity fabrication, all substrates were cleaned by ultrasonication in acetone and 2-propanol for 10 min, respectively, and subsequently treated 10 min with UV ozone (Ossila E511, 10 min). For non-transparent cavities (Chapter 4), 100 nm Au was thermally evaporated (MBraun G3) onto polished Si substrates with a 2 nm Cr adhesion layer. Afterwards, an AlO_x spacer layer was deposited by atomic layer deposition (Ultratech, Savannah S100, precursor

trimethylaluminium, Strem Chemicals, Inc.) at a temperature of 80 °C. The respective spacer thicknesses can be found in Chapter 4. The SWCNT layer was spin-coated from SWCNT dispersion at 2000 rpm on glass substrates yielding an average film thickness of (80 ± 20) nm and a SWCNT concentration of 1.13 wt%. The cavity was finalized with a second AlO_x spacer and 40 nm Au as a semitransparent top mirror. For transparent cavities (Chapter 5), glass substrates (Schott, AF32eco, 300 μm) were used. For top and bottom mirrors 30 nm Au and symmetric AlO_x spacers were deposited with a SWCNT layer sandwiched in between. The bottom mirrors was deposited on a 2 nm Cr adhesion layer. The respective spacer thicknesses can be found in Chapter 5. The SWCNT layer was spin-coated at 800 rpm yielding an average film thickness of (30 ± 15) nm with a 1.1 wt% SWCNT concentration in film. A schematic is given in Figure 3.1.

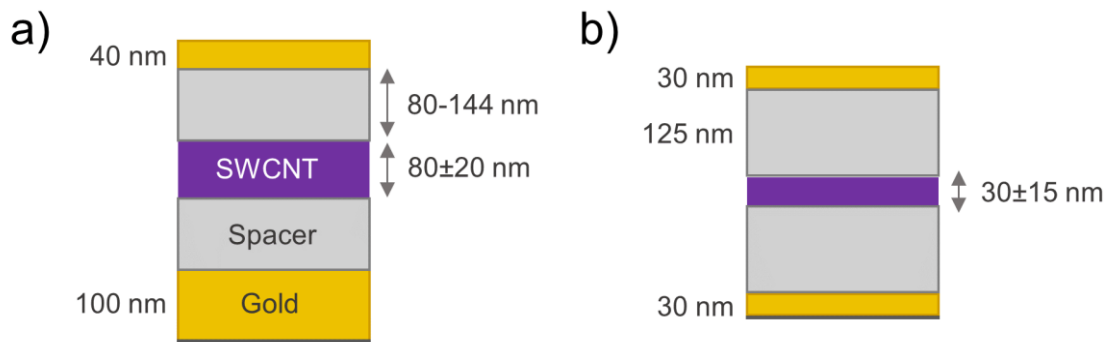


Figure 3.1 a) Schematic of the cavity stack used in Chapter 4 and b) in Chapter 5.

3.1.4 SWCNT Photodiodes

For photodiode fabrication, glass substrates were cleaned by ultrasonication with acetone, 2-propanol and de-ionized water for 10 min and treated with O_2 plasma for 3 min. Metal contacts were structured using a shadow mask. For the bottom contacts, a 1 nm Al adhesion layer and 25 nm Au were deposited by thermal evaporation in a vacuum chamber (Angstrom EvoVac) at a base pressure of 1×10^{-7} mbar. The samples were taken out of the chamber and treated again with O_2 plasma. Poly(3,4-ethylenedioxythiophene) polystyrene sulfonate (PEDOT:PSS, P VP AI4083, Clevios) was spin-coated at 3000 rpm to form a 40 nm layer, which was annealed at 150 °C for 10 min. Afterwards, the substrates were transferred to a dry nitrogen glovebox. Bulk

heterojunctions were prepared by spin-coating of a P3HT:PC₇₀BM:(6,5)SWCNT solution in chlorobenzene at speeds between 500 and 2000 rpm to yield thicknesses ranging from 160 to 230 nm. Flat heterojunctions were prepared by spin-coating a 14 g/L P3HT solution in chlorobenzene at 2000 rpm, followed by 0.5 g/L SWCNT in toluene spin-coated at 1000 rpm and 20 g/L PC₇₀BM in dichloromethane:2-chlorophenol (1:1) spin-coated at 2000 rpm. The devices were completed with 50 nm 4,7-diphenyl-1,10-phenanthroline (BPhen) doped with Cs and 100 nm Ag as a top electrode by thermal evaporation under vacuum. The finished devices were encapsulated with a glass lid and moisture getter using UV-curable epoxy (Norland NOA68). All photodiodes were fabricated in collaboration with Dr. Andreas Mischok.

3.2 Optical Characterization

3.2.1 UV-vis Transmission

Transmission spectra of dispersions and films were recorded with a Cary 6000i UV/Vis/NIR absorption spectrometer (Varian).

3.2.2 Angle-resolved optical characterization

For angle-resolved measurements a Fourier imaging system was employed, to enable on-shot measurement of the cavity and polariton dispersion, respectively. Reflected or emitted light was collected by an infinity corrected $\times 100$ NIR objective with 0.85 NA (Olympus, LCPLN100XIR) focused onto the sample. The spot diameter of ~ 2 μm defined the investigated area on the sample. The collected light was imaged from the back focal plane of the objective onto the entrance slit of a spectrograph (Princeton Instruments IsoPlane SCT 320) using a 4f imaging system (Figure 3.2) comprising a Fourier lens (achromatic doublet, $f_1 = 200$ mm) and a tube lens (achromatic doublet, $f_2 = 300$ mm). The resulting angle-resolved spectra were recorded by either a thermoelectrically cooled 640×512 InGaAs array (Princeton Instruments, NIRvana:640ST) or a 1340×400 Si CCD camera (Princeton Instruments, PIXIS:400) in case of high energy UP modes.

A linear polarizer (Thorlabs LPNIR050) was placed in front of the spectrometer to select between TE and TM polarization.

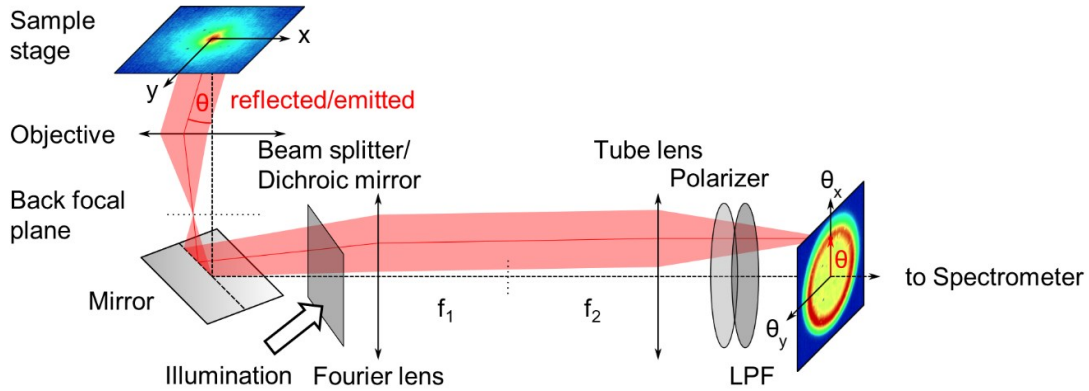


Figure 3.2 Schematic of the employed Fourier imaging microscope setup and illustration of the transformation from a real-space coordinates to angular coordinates.

For reflectivity measurements, the collimated white light source was directed into the objective using a non-polarizing broadband beam splitter (Thorlabs BSW29R, 50:50 split ratio,). For luminescence measurements, a 640 nm laser diode (Coherent OBIS, 5 mW, continuous wave) was directed into the objective using a dichroic mirror (Thorlabs DMLP730B, 730 nm cut-on) exciting the red tail of the E_{22} transition. Residual reflected laser light was blocked by a long-pass filter (LPF, 850 nm cut-off). For hyperspectral images, the Fourier lens was removed. For micrographs, the sample was illuminated from the top with collimated white light and the spectrograph grating was replaced by a mirror.

3.2.3 Thickness determination by transfer matrix simulation

Spin-coated films of SWCNTs exhibit inherent thickness gradients, which result in height differences of several tens of nanometers over large sample areas. In case of cavities, the change in film thickness determines the energy at zero degrees incidence of the respective cavity or LP mode. By monitoring the angle-resolved spectral reflectivity, sample positions of desired cavity thickness can be found. For this, the reflectivity spectra of the cavity samples presented in

Chapter 4 were simulated for an 80 nm thick SWCNT layer, as a function of oxide thickness (Figure 3.3a) using the transfer matrix scheme presented in the Background, section 2.1.2. Prior to data acquisition, the cavity samples were scanned to find sample positions that exhibited LP energies (Figure 3.3b), predicted for an 80 nm thick SWCNT layer at a given spacer thickness.

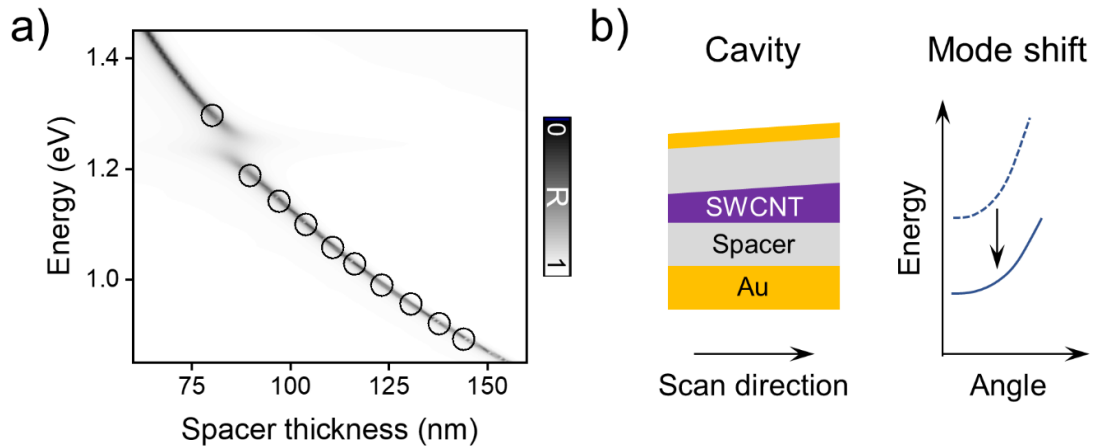


Figure 3.3 a) Simulated cavity reflectivity of the cavity stack shown in (b) as a function of oxide spacer thickness with an 80 nm SWCNT film. Black circles indicate the polariton mode energy (UP for positive, LP for negative detunings) for the different oxide spacer thicknesses in Chapter 4. **b)** Illustration of the mode shift to lower energies with increasing SWCNT thickness for a constant oxide spacer thickness.

3.2.4 Confocal optical characterization

The confocal optical setup is depicted in Figure 3.4. If not specified otherwise, confocal luminescence spectra were recorded by focusing the spectrally filtered (Photonete LLTF Contrast vis and short pass filter, **SPF**) output of a picosecond-pulsed supercontinuum laser source (Fianium WhiteLase SC400, ~6 ps pulse width, 20 MHz repetition rate, ~20 J/cm² pulse energy) through a $\times 100$ NIR-optimized objective (N.A. 0.85, Olympus, **OBJ1**) onto the sample. The sample could be moved by a xyz-piezo stage (Mad City Labs). The angle-integrated emission spectra were recorded using a spectrograph (Acton SpectraPro SP2358) connected to a liquid nitrogen-cooled InGaAs line camera (Princeton Instruments OMA V, **LC**). For this, the sample emission was separated from the back scattered laser light by a dichroic mirror (**DM**) and a long

pass filter (**LPF**), and focused with a tube lens (**TL1**) onto the entrance port of the spectrograph. The spectrograph allowed for spatial and spectral imaging of the sample emission, by changing between a mirror (**M**) and two gratings (**G1**, **G2**) mounted on a motorized turret. For spectral imaging the 150 grooves mm^{-1} grating with a 1200 nm blaze was used. The focused laser spot could be inspected by directing residual laser light to an alignment camera (Pixelink, **Si Cam**) using a flip-mirror (**FM**) and a tube lens (**TL2**).

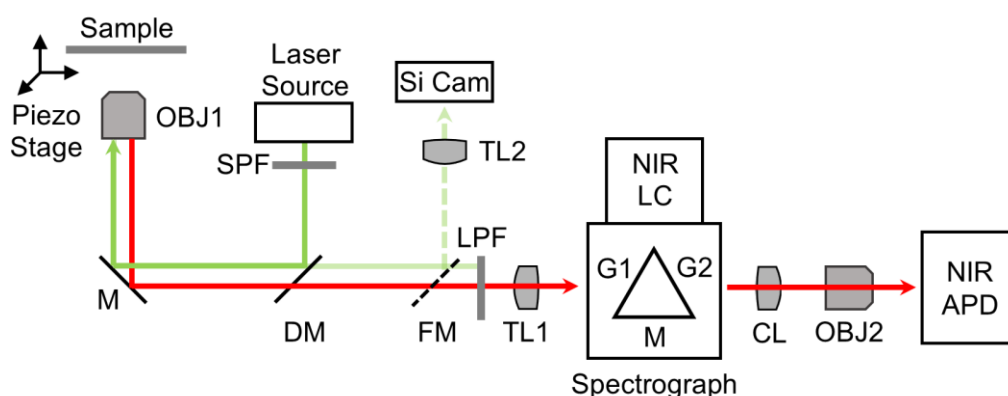


Figure 3.4 Schematic of the setup used for confocal optical characterization. Excitation (green) and emission (red) beam paths are indicated.

The recorded data was corrected for background noise and detection efficiency (section 3.2.9). The described confocal setup was also used for spatial and excitation-wavelength maps of the sample emission (section 3.2.5) and fluorescence lifetime measurements (section 3.2.6). Due to the geometrical restrictions of the setup, these measurements were not performed with angular-resolution and the consequences are discussed in section 3.2.7.

3.2.5 Photoluminescence spatial and excitation maps

In confocal configuration, spatial scans of the sample emission were performed using the xyz-piezo stage (Mad City Labs, **PZ**, Figure 3.4). The same configuration was used to record photoluminescence excitation (PLE)-maps, by tuning the laser output over the spectral range of

interest and corrected for the LLTF's wavelength-dependent output power. Both measurements were automated using a customized LabVIEW script, written by Dr. Yuriy Zakharko.

3.2.6 Fluorescence Lifetime

The fluorescence decay dynamics were investigated using time-correlated single photon counting (TCSPC). Using the side exit of the spectrograph used for confocal configuration (section 3.2.4), the sample fluorescence was focused onto a gated InGaAs/InP avalanche photodiode (Micro Photon Devices, **NIR APD**, Figure 3.4) through a collimating lens (**CL**, Figure 3.4) and a $\times 20$ NIR-optimized objective (Mitutoyo, **OBJ2**, Figure 3.4). Statistics of the arrival times of the photons were acquired with a TCSPC module (PicoHarp 300, Picoquant GmbH). The instrument response function (IRF) was estimated for each sample from the fast, detector-limited PL decay of the (6,5) SWCNTs at the E_{11} transition at 1015 nm. All decay curves were fitted to a biexponential model in a reconvolution procedure correcting for the IRF using the SymphoTime64 software. The detection limit based on the IRF FWHM of ~ 80 ps using this procedure was 8 ps. To record the cavity fluorescence lifetime, an angle-integrated emission spectrum was recorded prior to performing TCSPC to select the cavity emission wavelength at $k_{\parallel} = 0$.

3.2.7 Interpretation of angle-integrated polariton emission spectra

In case of confocal measurements of cavity luminescence, the polariton or cavity angular dispersion has to be considered. The cavity luminescence recorded with the confocal setup approximately resembles the sum over the angle-resolved cavity luminescence from -30 to 30 degrees (Figure 3.5a and b). This estimate will be used throughout this thesis, when interpreting confocally measured cavity luminescence. For the fluorescence lifetime measurements, polariton emission at the wavelengths corresponding to $k_{\parallel} = 0$ was collected. The maximum range of angles that contribute to this emission is ± 20 degrees for cavity detunings up to -33 meV based on the FWHM (Figure 3.5c). Note that for detunings closer to resonance, the curvature around $k_{\parallel} = 0$

decreases, leading to an increased contribution from larger angles. However, in case of TCSPC experiments, the angular-dependence of the polariton intrinsic lifetime of the cavity samples presented here cannot be resolved and the contribution can be neglected.

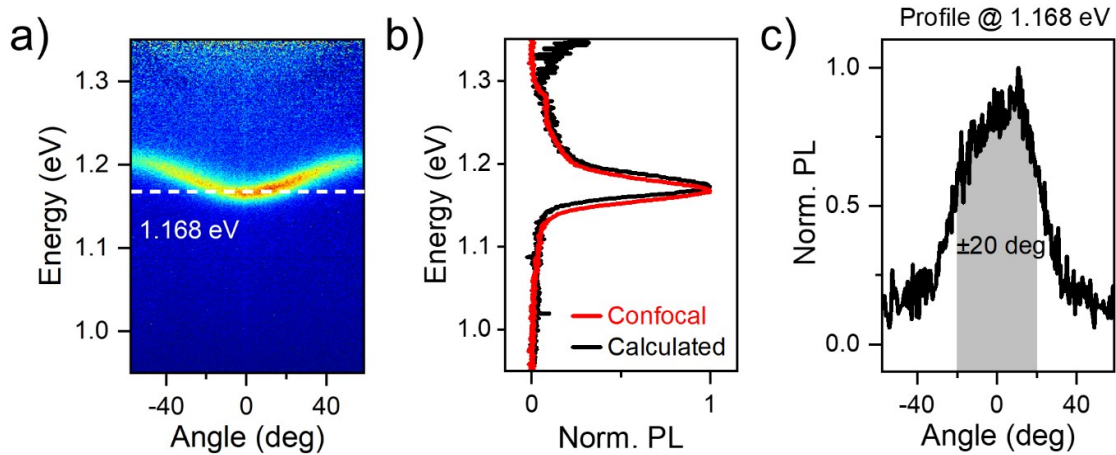


Figure 3.5 **a)** Angle-resolved PL of a SWCNT microcavity in the strong coupling regime. **b)** Normalized PL of the same sample measured confocally at a position with similar detuning (red line) and the sum of the data in (b) from -30 to 30 degree for comparison (black line). **c)** Intensity profile of data in (a) at 1.168 eV.

3.2.8 Photoluminescence Quantum Yield

The PL quantum yield (PLQY) of pristine and functionalized SWCNT films in PFO-BPy was determined by an absolute approach¹⁷¹ directly measuring the ratio of emitted and absorbed photons. For this, the spectrally-filtered output of a supercontinuum laser (10 ps pulse width, 20 MHz repetition rate, WhiteLase SC400, Fianium) was tuned to the (6,5) SWCNT E_{22} transition at 576 nm, collimated, and directed into an integrating sphere (LabSphere, Spectralon Coating). Using an optical fiber, the signal from the sphere was coupled into an Acton SpectraPro SP2358 spectrograph (grating 150 lines/mm) and imaged onto an OMA-V InGaAs line camera (Princeton Instruments) for spectra acquisition. The SWCNT emission was measured by collecting the signal in the NIR range (900-1600 nm) with an SWCNT sample mounted inside and the laser beam being directed onto the sample. The SWCNT absorption was measured by determining the laser attenuation by the sample around 576 nm. To only account for direct emission and absorption,

the laser was directed onto the integrating sphere wall and the corresponding emission and absorption spectra were subtracted from the spectra recorded under direct illumination. The collected spectral intensities were corrected as described in section 3.2.9, transformed by $I(\lambda) \cdot \lambda$ and integrated to yield the number of absorbed and emitted photons.

Due to the small stokes shift of SWCNT, it is necessary to account for reabsorption in highly concentrated samples such as films.¹⁷² For this, the SWCNT film emission spectrum was collected as described in section 3.2.4 and scaled to the red tail of the emission spectrum collected from the integrating sphere. The resulting spectrum was used to calculate the number of emitted photons, as described above. Note that this approach still contains reabsorption for a single pass of photons emitted in the volume of the film. However, the chosen approach still contains the effects of interactions in solid film on the SWCNT emission, in contrast to approaches employing the emission spectrum of dilute liquid samples to account for reabsorption. Determining the PLQY as described above, ensures conservative estimation of the non-radiative decay rate (see Chapter 4).

3.2.9 Spectral corrections

In transmission and reflectivity experiments, spectral corrections were performed by recording the substrate transmission and reflectivity, respectively, and dividing the sample spectrum by its corresponding reference. For luminescence experiments, the detection efficiency was determined by measuring the transmission of a calibrated white light source (Thorlabs SLS201/M, 300-2600 nm) of known spectral power distribution ($I_{theo,lamp}(\lambda)$) through the detection path. Using the experimental transmission spectrum ($I_{exp,lamp}(\lambda)$), a correction function $f_{corr}(\lambda)$ was determined by

$$f_{corr}(\lambda) = \frac{I_{exp,lamp}(\lambda)}{I_{theo,lamp}(\lambda)}. \quad (41)$$

All experimental luminescence spectra were divided by a corresponding correction function. Additionally, all luminescence spectra given in energy were transformed by (Jacobian correction):

$$I(E) = I(\lambda) \cdot \lambda^2/hc. \quad (42)$$

3.2.10 Transient transmission and absorption

All femtosecond transient transmission (TT) and absorption (TA) measurements were conducted on a commercial TA spectrograph (Helios Fire, Ultrafast Systems). The pump-pulses were generated by a commercial optical parametric amplifier (TOPAS-Prime, Light Conversion) pumped by a regeneratively amplified femtosecond Ti:sapphire laser (Astrella, Coherent) centered at 800 nm (4 kHz repetition rate, 78 fs pulse durations, 1.6 mJ pulse energy). The investigated area on the sample was defined by the spot size of the focused pump beam with a FWHM $\sim 250 \mu\text{m}$. For a 100 nJ pulse, the pump fluence was typically $200 \mu\text{J}/\text{cm}^2$. The supercontinuum probe beam was linearly polarized at the magic angle (54.7°) relative to the pump beam. Prior to analysis, spectra were corrected for the group velocity dispersion of the broadband probe beam. All TT and TA measurements were performed by Dr. Zhouran Kuang.

3.3 Miscellaneous characterization techniques

3.3.1 Profilometry

Profilometry of photodiode active layers was carried out using a Bruker Dektak XT profilometer. For all other samples, film thickness and RMS roughness were extracted from micrographs recorded by atomic force microscopy (AFM) with a Bruker Dimension Icon in tapping mode. The employed tips (Scanasyt-Air, Bruker) had a nominal tip radius of 2 nm and a nominal spring constant of 0.4 N/m. The image quality was controlled automatically by the Bruker Scanasyt algorithm.

For soft films (polymers and SWCNT-polymer composites) the layer thickness was determined from the step heights of manually created scratches. For oxide films, steps were created on a photolithographically structured height reference substrates by a lift-off technique. The height reference substrates were prepared by spin-coating of LOR5B (MicroChem, 4000 rpm, 30 s, 185 °C baked for 4 min) and S1813 (MicroPosit, 4000 rpm, 30 s, 115 °C baked for 1 min) and subsequent illumination under a dark-field photo mask with an 80 mJ/cm² dose. The exposed samples were developed in MF-319 (MicroPosit) for 22 s. After oxide deposition, the photoresist was removed overnight in N-methyl-2-pyrrolidone (NMP, Sigma Aldrich), creating evenly spaced, parallel lines of oxide for step height measurements.

3.3.2 EQE and Current density

All EQE and current density measurements were conducted at the Gather Lab at the University of St. Andrews. For photodiode characterization, density-voltage characteristics were recorded with a source measuring unit (SMU, Keithley 2450). The external quantum efficiency was determined by measuring the photocurrent without external voltage (short-circuit current) under illumination. The light-source, an optical parametric amplifier (Ekspla PG403) pumped by a solid-state regenerative amplifier laser (Ekspla PL2210), was tuned over visible and NIR spectral window (~1 nm linewidth). The excitation power was calibrated to 0.1 mW using amplified Si (Thorlabs PDA100A) and Ge (Thorlabs PDA50B2) photodiodes. The calculated EQE spectra were smoothed over 5 nm using a Savitzky-Golay algorithm.

3.4 Data analysis and simulation

Data analysis was conducted either with OriginPro¹⁷³ 2020 (OriginLab) or MATLAB¹⁷⁴ 2021 (MathWorks). All simulations were implemented in MATLAB.

3.4.1 Angle-resolved data and coupled oscillator fit

Data analysis of the angle-resolved spectra was automated using a MATLAB code adapted from an earlier version written by Dr. Arko Graf. The script performed the corrections discussed in

section 3.2.9 for reflectivity and luminescence measurements, respectively, apart from the background correction, which was executed by the spectrometer control software (LightField 4.5, Teledyne Technologies). The angle was assigned to the data using the nominal objective NA. 5 % of the high angle signal was removed due to diffraction artifacts stemming from the objective aperture. The mode position was extracted from the peak position of a Lorentzian fitted to each data line. The resulting modes were analyzed by fitting the analytical expressions of the coupled oscillator model presented (Background, section 2.1.6).

3.4.2 Transfer matrix simulation

The transfer-matrix (TM) scheme was adapted from a MATLAB code written by Dr. Laura Tropf based on Pettersson *et al.*⁶¹ The core function calculating the transfer matrix (Background, section 2.1.2) was adapted to include scalar scattering after Yin *et al.*⁶² For TM simulation of transient transmission spectra, the code was rearranged to accommodate a commercial genetic algorithm¹⁷⁵ to fit the input parameters of a simulated cavity stack to experimental transient transmission spectra, which is described in Chapter 5.

3.4.3 Complex refractive index data

Complex refractive index data for SWCNTs and PFO-BPy was experimentally determined by Laura Tropf and Dr. Andreas Mischock at the University of St Andrews using an ellipsometer from J.A. Woollam Co. (model M-2000DI). For SWCNT layers with concentrations different from the reference data, the SWCNT E_{11} absorption was approximated with a Lorentzian peak and the complex refractive index of the SWCNT-PFO-BPy composite was calculated using the Kramers-Kronig relation (Background, section 2.1.1). The experimentally obtained refractive index of PFO-BPy was used as the background refractive index. For time-dependent simulations, the transient complex refractive index was calculated from SWCNT transient absorption data using the Kramers-Kronig relation (Background, section 2.1.1) in combination with a genetic algorithm¹⁷⁵ to fit the SWCNT film thickness.

The temperature-dependent and time-dependent refractive index for gold thin films was calculated using a MATLAB code implementing the method of Liu *et al.*¹⁷⁶ and Rakic *et al.*¹⁷⁷.

Refractive index data for other materials were downloaded from refractiveindex.info and the corresponding references are listed in Table 3.1.

Table 3.1 Complex refractive index data.

Material	Reference
Au	K. M. McPeak, S. V. Jayanti, S. J. P. Kress, S. Meyer, S. Iotti, A. Rossinelli, and D. J. Norris. Plasmonic films can easily be better: Rules and recipes, <i>ACS Photonics</i> 2, 326-333 (2015)
Ag	W. S. M. Werner, K. Glantschnig, C. Ambrosch-Draxl. Optical constants and inelastic electron-scattering data for 17 elemental metals, <i>J. Phys. Chem. Ref. Data</i> 38, 1013-1092 (2009)
AlO _x	R. Boidin, T. Halenkovič, V. Nazabal, L. Beneš, P. Němec. Pulsed laser deposited alumina thin films, <i>Ceram.</i> 42, 1177-1182 (2016)

3.4.4 Global analysis

Time-resolved transient transmission and absorption datasets were analyzed according to Alagna *et al.* via standard global analysis.¹⁷⁸ The spectra were fitted globally by a sum of exponentials with wavelength dependent amplitudes. As SWCNT exhibit slightly non-exponential decays owing to diffusive contributions to their decay,¹¹⁰ the number of exponentials was chosen to yield minimum fitting error and residual structure. For SWCNT and cavity data five exponentials and one offset gave the best results.

4 Fluorescence dynamics of SWCNT exciton-polaritons

The complex photophysics of SWCNTs and overall goal of polariton condensation pose the question of how exciton-polaritons are populated and how they relax to radiative states. In this chapter, the contributions of possible relaxation processes, i.e., scattering with acoustic phonons, vibrationally assisted scattering and radiative pumping, are investigated using angle-resolved steady-state and time-resolved PL measurements on planar microcavities with a wide range of detunings. The chapter is concluded by demonstrating how luminescent sp^3 defects can be used to increase and tailor the SWCNT exciton-polariton population.

Part of this chapter was published in Lüttgens *et al.*, ACS Photonics **2020**, 8 (1), 182-193.¹⁰⁹ Modified reprints are presented with permission of the American Chemical Society.

4.1 Introduction

A striking characteristic of SWCNT exciton-polaritons in planar microcavities is a distinct change of emission intensity with detuning,^{40,41} which already suggests that the polariton population may be a function of detuning. This feature was first described in the seminal study on SWCNT polaritons by Graf *et al.*⁴⁰ and hypothesized to be a phonon-related relaxation bottleneck. In this chapter, a systematic study is conducted to find definite evidence for the population mechanics, that produce the observed emission features. The relaxation can be investigated by injecting polaritons off-resonance via exciting the SWCNTs at the E_{22} transition well above the strongly coupled, lowest excited state. After fast internal relaxation the exciton reservoir is populated.⁷⁴ From there, the excitations can either populate the polariton states or follow radiative and non-radiative channels of the weakly coupled emitter. Figure 4.1 depicts the established polariton population mechanisms conceivable for SWCNTs, that is, scattering with acoustic phonons (process i), scattering with optical phonons (process ii), and radiative pumping (process iii) (see

Background, section 2.2.2 for details). In the organic polariton literature, process ii is also termed vibrationally assisted scattering (VAS) and the term shall be adopted here, for better comparison with references used in this chapter. Due to the short intrinsic polariton lifetime in metalclad cavities (15-50 fs, calculated by linewidth), polaritons decay virtually instantaneously after population. Therefore, the structure of the steady-state polariton PL and the long-lived polariton fluorescence lifetime are direct indicators of the population mechanism. In the first part of this chapter, the polariton steady-state PL is assessed, followed by analysing the polariton fluorescence decay to identify the population mechanism. In the second part of this chapter, the effect of SWCNT luminescent sp^3 defects on the polariton dynamics and population is presented.

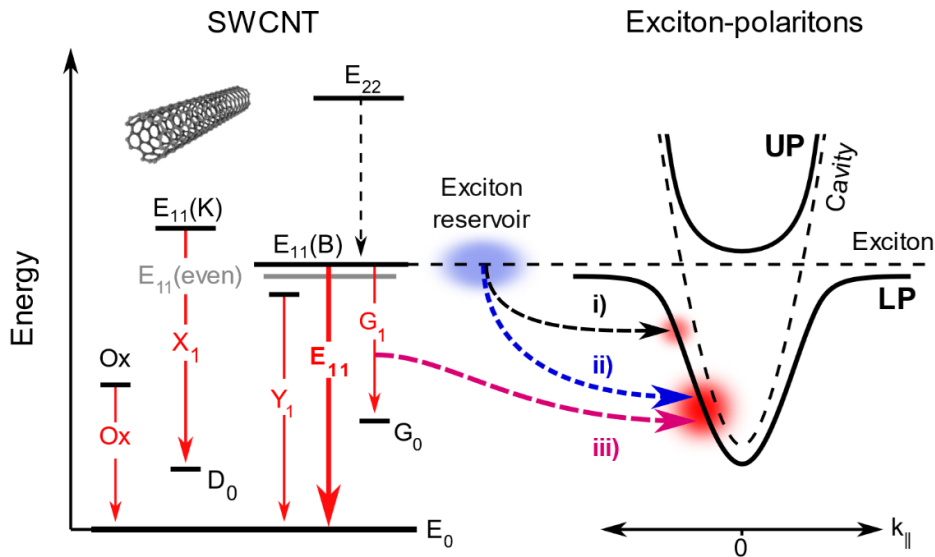


Figure 4.1 Schematic of the polariton population in SWCNT exciton-polaritons. **(Left)** Weakly coupled transitions in (6,5) SWCNTs: The fundamental E_{11} transition (from the bright $E_{11}(B)$ exciton) followed by weaker and red-shifted sideband transitions (Y_1 , X_1 , G_1 , Ox). $E_{11}(K)$ denotes the degenerate K-momentum dark excitons. **(Right)** SWCNT exciton-polariton upper (UP) and lower (LP) polariton modes (solid lines) with cavity mode and exciton absorption (dashed lines). The conceivable population mechanisms are scattering of reservoir excitons with acoustic phonons (i), with optical phonons (ii) or radiative pumping (iii).

4.2 SWNT exciton-polariton emission as a function of detuning

The characteristic change of emission intensity as a function of detuning observed for SWNT exciton-polaritons is presented in Figure 4.2b. The data was recorded from a metal-clad microcavity with strongly coupled (6,5) SWCNTs embedded in a polymer matrix, as employed in the original study by Graf *et al.*⁴⁰ Using the inherent thickness gradient of the spin-coated SWCNT/polymer film from 240 nm to 330 nm, different cavity detunings can be observed and characterized by moving to different positions on the sample.

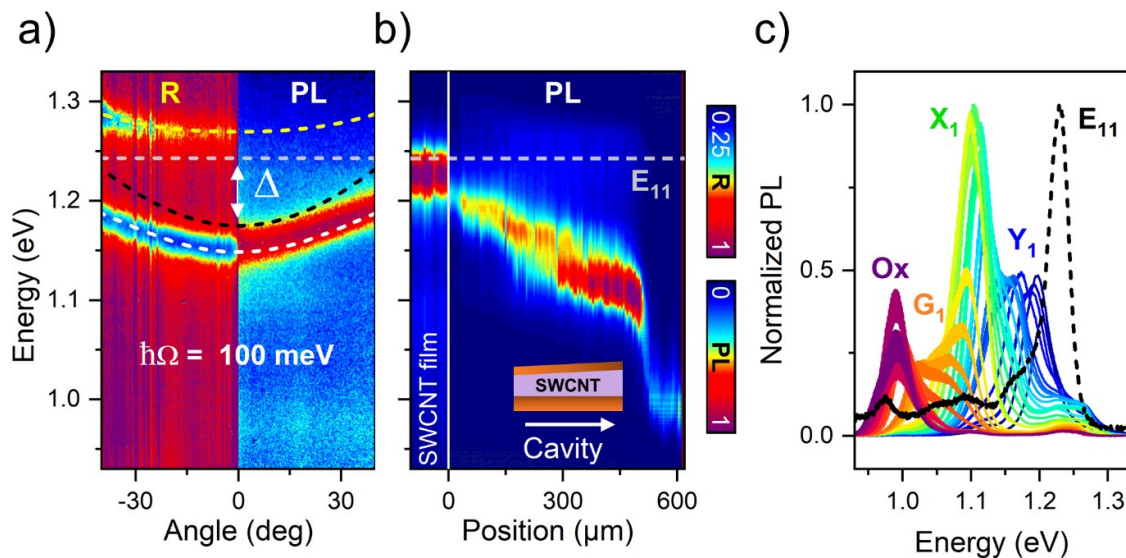


Figure 4.2 Metalclad cavity filled with (6,5) SWCNT in a PFO-BPy matrix. **a)** Angle-resolved reflectivity (R) and emission (PL) spectra with E_{11} energy (grey dashed line), UP (dashed yellow line), cavity mode (dashed black line), LP (dashed white line) and detuning Δ . **b)** Angle-integrated PL spectra as function of sample position (i.e., film thickness). The PL scan of a (6,5) SWCNT reference film is given as reference. **c)** Data in (b) color-coded for the overlap with SWCNT sideband transitions (Y_1 - blue, X_1 - green, G_1 - orange and O_x - purple). The PL spectrum of the reference is given for comparison (black dashed line).

Figure 4.2a shows angle-dependent reflectivity and emission spectra in TM polarization for one specific detuning recorded using Fourier imaging (see Experimental, section 3.2.2). The data exhibits upper and lower polariton modes with a clear anti-crossing at exciton absorption,

confirming that the sample is in the strong coupling regime. A coupled oscillator fit to the polariton modes, as described in the Experimental, section 3.4.1, yields a Rabi splitting of 100 meV and a detuning of - 68 meV.

Figure 4.2b presents confocally collected PL from cavity shown in Figure 4.2a for a scan along the sample. In this confocal configuration, the polariton emission is integrated over all angles up to 30° (Experimental, section 3.2.7). The emission below the E_{11} exciton absorption can be attributed to the lower polariton branch. The PL from a scan along a (6,5) SWCNT reference film is given for comparison (Figure 4.2, left). While the polariton emission exhibits several maxima over the whole detection range with intensity changes of up to 90 %, the exciton emission (E_{11} , 1.227 eV) of the reference film remains essentially constant with fluctuations of about 35 %. By scanning along the sample, the film thickness and thus the detuning of the microcavity is changed. Increasing the film thickness or cavity length, respectively, shifts the LP to lower energies and results in a red shift of the polariton emission with distinct emission maxima, that cannot be explained by inhomogeneities of the SWCNT layer.

Figure 4.2c reveals that the spectral positions of the observed emission maxima coincide strikingly well with the SWCNT photoluminescence sideband (PSBs) emission energies of the (6,5) SWCNT PL spectrum, that is, the Y_1 (1.205 eV), X_1 (1.097 eV), G_1 (1.050 eV) and O_x (0.970 eV) sidebands (see Background, section 2.3.1 for more details on SWCNT PSBs). Therefore, the SWCNT PSBs must play a prominent role in the polariton population of the system.

However, the relative intensities of the LP emission maxima are more difficult to interpret, as they are not only influenced by the efficiency of the polariton population but also by the E_{22} excitation efficiency at a given detuning. Owing to the large stopband of metalclad cavities, there usually exist higher-order cavity modes (Background, section 2.1.3). Here, the E_{22} absorption can be increased by the cavity λ -mode (~ 2 eV) resulting in a detuning dependence of the excitation efficiency. In Figure 4.2c, this may be the case at the detuning for which the LP emission maximum correlates with the X_1 transition. In the following section, a more controlled sample

design is presented, in which the detuning is independent of the SWCNT layer thickness. Apart from other advantages explained in the following sections, this sample design also allows to correct the LP emission intensity for cavity enhanced absorption at the E_{22} transition, which is done in the last section 4.10.

4.3 Oxide spacers for improved control over cavity tuning

In order to quantitatively assess the impact of detuning on the polariton population, the cavity detuning has to be decoupled from the SWCNT film thickness, that is, the number of strongly coupled SWCNT excitons. For this, cavities with uniform dense (6,5) SWCNT films and metal oxide (AlO_x) spacer layers were prepared (Experimental, section 3.1.3). Employing atomic layer deposition (ALD) for the spacer layer, the cavity tuning can be precisely controlled without changing the SWCNT layer thickness or number of emitters, respectively. Furthermore, this approach ensures that the SWCNT layer is always at the electric field maximum of the cavity's fundamental mode and the number of weakly coupled SWCNTs is reduced. To compensate for remaining thickness variations of the SWCNT layer, the LP position was predicted by transfer matrix simulations for a SWCNT thickness of choice, here 80 nm, and for each oxide thickness.

By locating sample positions with the corresponding LP energy, the emitter layer thickness can be controlled beyond the intrinsic accuracy of the employed spin-coating process down to ± 1.8 nm (Experimental, section 3.2.3). Lastly, controlling the sample layer thicknesses to high accuracy allows for precise determination of the λ -mode position of each sample, which governs the excitation efficiency, as it could be resonant with the excitation laser and is therefore of relevance in the last section, where the polariton populations of different samples are compared to each other.

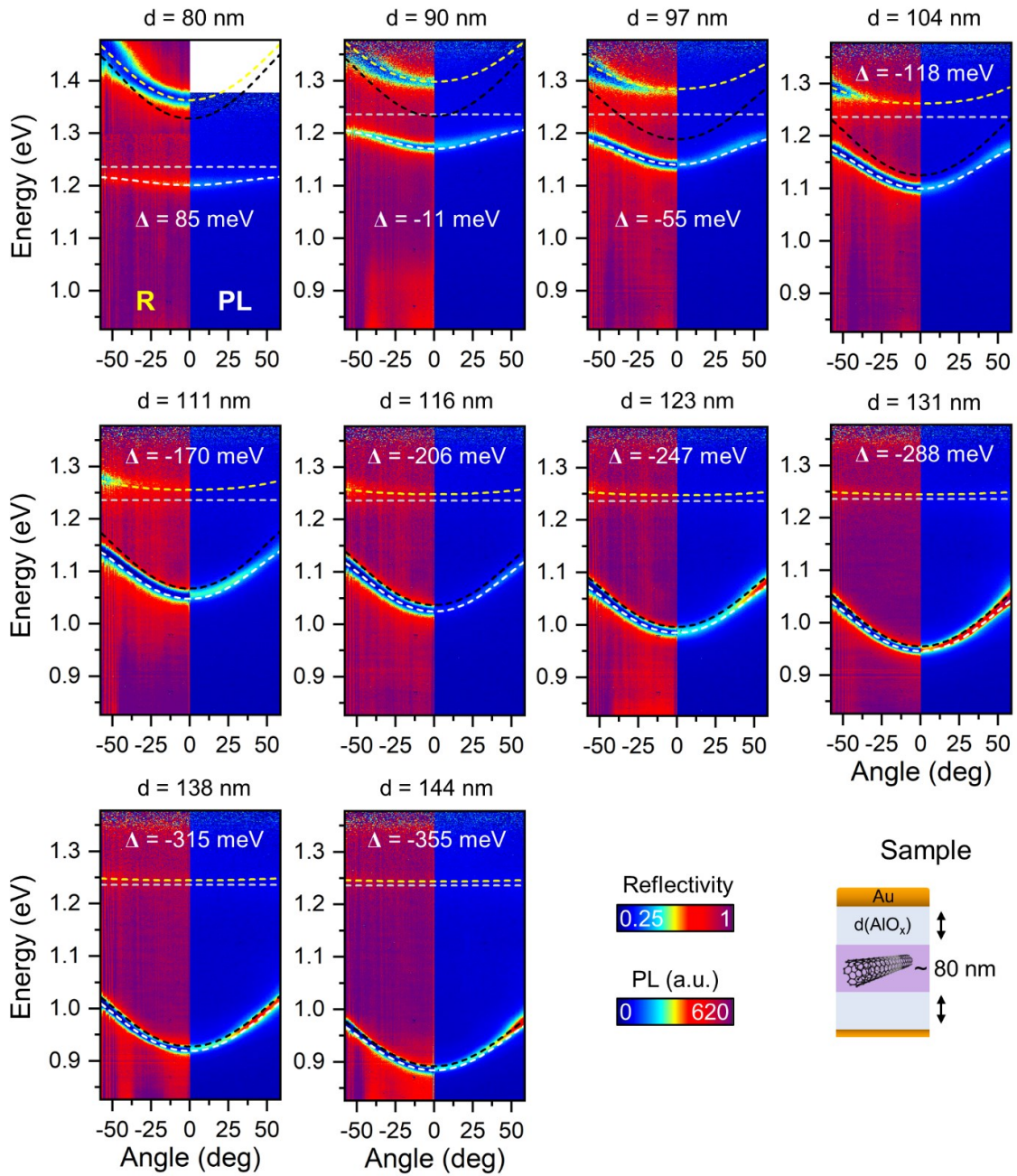


Figure 4.3 Angle-resolved reflectivity (R) and photoluminescence (PL) spectra of ten strongly coupled oxide spacer cavities. Spacer thickness d and detuning Δ are given for each data set. The data was fitted to the CO-model (dashed lines) and the results are shown in Figure 4.4.

In the following, the basic properties of the strongly coupled oxide spacer cavities are presented. Figure 4.3 depicts the angle-resolved reflectivity (R) and photoluminescence (PL) spectra of ten SWCNT filled oxide spacer cavities tuned over the whole SWCNT emission spectrum. For

smaller oxide spacers (80-111 nm) an anti-crossing at the energy of the SWCNT exciton is clearly visible, indicating strong coupling. For the 80 nm oxide spacer, the UP mode lay outside the InGaAs detection range and was recorded using a Si-CCD. Note that the Si-CCD-data shows a distortion of the UP mode at the SWCNT phonon-sideband in absorption (1.44 eV). At higher SWCNT concentrations, a full splitting is observed at this energy due to strong coupling of the phonon-sideband in absorption.^{42, 56} For larger oxide spacers (116-144 nm), the anti-crossing shifts outside the NA of the objective and the UP becomes fainter, however, the Rabi-splitting can still be extracted from the dispersion of the visible part of the UP mode using the CO-model (see Experimental, section 3.4.1 for details). Emission is only observed from the LP mode, with the PL intensity showing a strong modulation depending on detuning and angle, similar to the observations made in section 4.2.

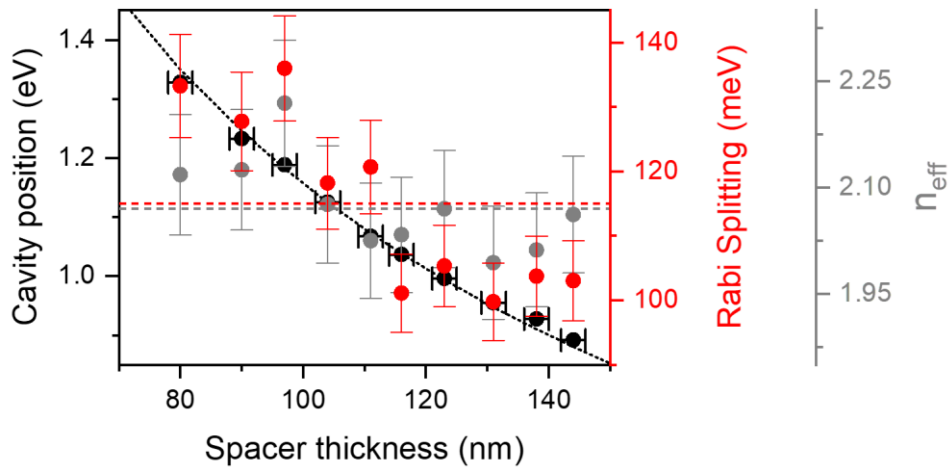


Figure 4.4 CO-fit results of the angle-resolved reflectivity of the oxide spacer cavities shown in Figure 4.3. The calculated cavity position is given as black dashed line. The average values of the Rabi splitting and the effective refractive index are given as red and grey dashed lines, respectively.

Figure 4.4 depicts the CO-model parameters obtained from a fit to the angle-resolved reflectivity data shown in Figure 4.3. The fitted cavity positions (C_0) agree well with the calculated cavity position ($C_{0,\text{calc}}$), given by

$$C_{0,\text{calc}} = \frac{hc}{2n_{\text{eff}} \cdot (2L_{\text{ox}} + L_{\text{SWCNT}})}, \quad (43)$$

where n_{eff} is the effective refractive index, averaged over the fitted values for n_{eff} (2.07). L_{ox} is the thickness of the oxide spacer and L_{SWCNT} is the thickness of SWCNT film (80 nm). As uncertainty of the cavity position, the error estimated for the SWCNT film thickness was used (2 nm). Theoretically, the Rabi splitting and effective refractive index do not depend on detuning or cavity length, respectively. However, the fitted Rabi splitting and effective refractive index values (Figure 4.3) scatter considerably and decrease with increasing cavity length. Therefore, the respective error bars in Figure 4.4 were estimated by the error of the ordinate intercept of a linear regression to the fitted Rabi splitting and effective refractive index. Even with this higher uncertainty, the obtained Rabi splitting decreases with increasing cavity length (Figure 4.4). This may be due to decreasing light-matter coupling for an increasing number of scattering sites with increasing oxide spacer length. The effective refractive index depends less on the cavity length and the average of all fitted values describes the fitted cavity positions using equation (43) (Figure 4.4, black dashed line), in agreement with the CO-model.

The following sections elaborate, how the possible polariton population mechanisms can be distinguished experimentally exploiting the more controlled sample design.

4.4 Polariton population by scattering with acoustic phonons

The first conceivable polariton population mechanism based on SWCNTs is scattering with acoustic phonons, that is, a reservoir exciton loses momentum and energy equivalent to an acoustic phonon, to occupy a corresponding state in the LP branch (Figure 4.1, process i). In case of organic polaritons, the intrinsic polariton lifetime is too short to allow for further scattering of

bright polaritons with acoustic phonons. Accordingly, the respective LP population can only arise from single scattering events.¹⁰² In (6,5) SWCNTs, LP states down to about - 37 meV below the exciton energy could be populated by this mechanism, which is the energy of the SWCNT radial breathing mode (RBM)¹⁷⁹. As there is no experimental data on the acoustic phonon modes and density of states (DOS) in SWCNT-polymer composites, two possible scenarios are considered in the following.

In the first scenario, the acoustic phonons are assumed to possess a one-dimensional DOS, exhibiting characteristic van Hove singularities, as was derived from the unperturbed SWCNT crystal structure.^{179, 180} Since the scattering rate depends on the phonon density of states (DOS)⁹⁶, distinct peaks should be visible in the polariton PL down to - 37 meV detuning, indicating efficient population at the van Hove singularities. This is not observed, as can be seen in Figure 4.2b. In the second scenario, the acoustic phonon DOS is assumed to be significantly broadened by local disorder present in the polymer-embedded random SWCNT network and essentially becomes a continuum. For this scenario, the LP population and emission, respectively, can be calculated following a model developed for J-aggregates by Litinskaya *et al.*⁹⁸ As the model does not treat the J-aggregates explicitly on the molecular level, the approach can be readily adapted to networks of SWCNTs, effectively treating them as semiconducting polymers¹⁰⁴. Following Litinskaya *et al.*⁹⁸, the change of the LP emission intensity with detuning is proportional to the scattering of reservoir excitons with a continuum of acoustic phonons and can be written as

$$I_{LP}(\Delta) \propto \frac{|\beta_{LP}|^2}{\gamma_C} O^{(ex-pol)}, \quad (44)$$

where $I_{LP}(\Delta)$ is the emission intensity of the lower polariton, β_{LP} is its exciton fraction, γ_C is the cavity lifetime and $O^{(ex-pol)}$ is the overlap between the reservoir exciton population and the LP DOS (a derivation can be found in Appendix, section 8.1.1). Using equation (44) and the data obtained from the microcavities with oxide spacers, the LP emission as a function of detuning for population by scattering with acoustic phonons was calculated. For this, the overlap between the

reservoir exciton population and the LP branch was approximated by calculating the overlap between the experimental spectra of the SWCNT E_{11} absorption and the LP mode in reflectivity, both for 80 nm SWCNT film thickness. The exciton fraction was taken from a CO-fit to the microcavity reflectivity data (Figure 4.3) and the cavity lifetime was calculated from the LP linewidth at the detuning with the highest photon fraction (98 %). The results are shown in Figure 4.5.

For the purpose of this section, the following discussion is limited to general trends of LP emission with detuning. The more intricate correlation with sidebands after full correction of the data is presented in section 4.10. Figure 4.5a depicts the normalized LP emission at $k_{||}=0$ as a function of detuning for oxide spacer microcavities filled with SWCNT. The experimental LP emission increases with increasing photon fraction of the LP from positive to negative detuning, whereas the calculated LP emission decreases with increasing photon fraction (Figure 4.5b). Only for small detunings with sufficient overlap between reservoir exciton and polariton states as well as sufficiently high exciton fraction, scattering with acoustic phonons would contribute significantly to the LP emission (compare equation (44)). The observation, that experimental LP emission monotonically decreases for detunings from -188 to 85 meV detuning, suggests that the contribution of acoustic phonons to the polariton population is very small.

Since the experimental data does not support either of the two conceivable scenarios for acoustic phonon involvement in the polariton population, this process can be ruled out. The following focusses on the remaining two population mechanisms, that is, scattering with optical phonons and radiative pumping.

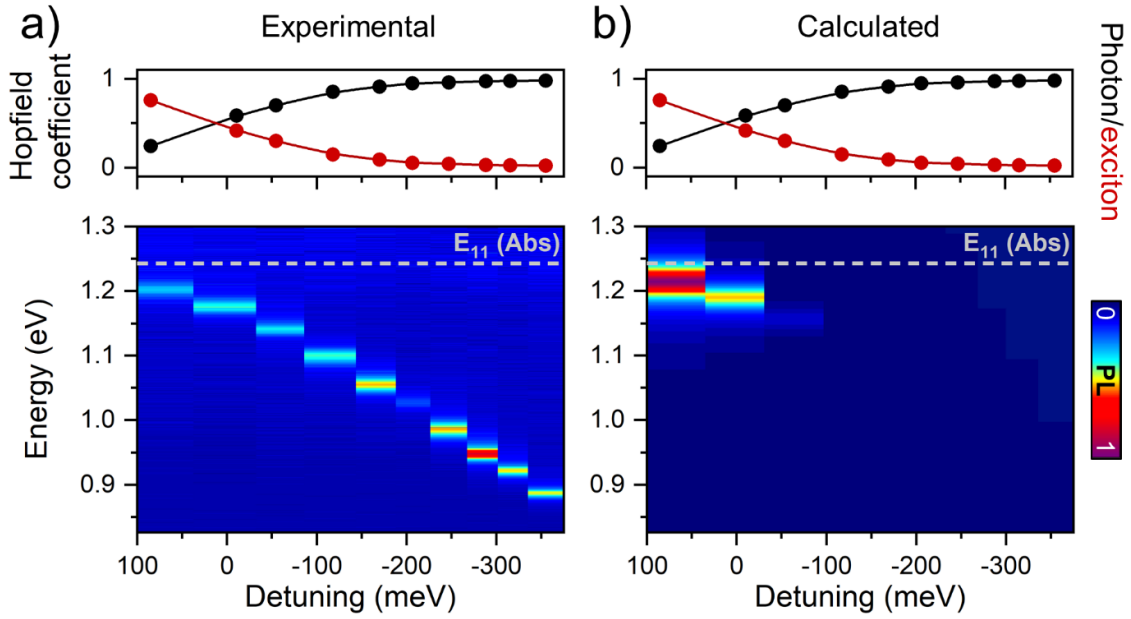


Figure 4.5 Normalized LP emission intensity at $k_{||}=0$ as a function of detuning for **a)** experimental and **b)** calculated data. The corresponding Hopfield coefficients for excitons (red dots) and photons (black dots) are given for comparison.

4.5 Vibrationally assisted scattering vs. radiative pumping

In section 4.2 it was found, that all SWCNT photoluminescence sidebands (PSBs) seem to contribute to the LP population. This already suggests, that the responsible mechanism might be radiative pumping (Figure 4.1, process iii), since all PSB can radiatively populated the LP (compare Background, section 2.2.2), regardless of their photophysical origin. However, the X_1 and G_1 sidebands originate from optically active D and G phonons, which may scatter reservoir excitons into the LP (Figure 4.1, process ii). The latter process is predicted to be very fast for disordered organic semiconductors,⁹⁸ whereas the former process occurs with the emission efficiency of the weakly coupled emitter.⁸⁰ In the following, the polariton fluorescence decay is investigated and compared to a weakly coupled reference to distinguish between the two processes.

The time-dependent fluorescence data was obtained using time-correlated single-photon counting (TCSPC). The cavity fluorescence was averaged over $\pm 20^\circ$ around $k_{||}=0$, due to restrictions of

the measurement setup (for details see Experimental, section 3.2.6 and 3.2.7). Note that for organic polaritons, the reservoir related fluorescence lifetime component was found to be angle-independent⁸⁷ and angle-dependent lifetime changes only appear on the timescale of the intrinsic polariton decay.⁸⁶

Figure 4.6 presents the time-dependent fluorescence data. For the fluorescence decay of the oxide spacer microcavities introduced in section 4.3, all transients were well-described by a biexponential decay convoluted with the instrument response function (IRF). Figure 4.6a shows a representative histogram. The extracted lifetimes ranged from 20 to 200 ps for the short lifetime component and from 170 to 650 ps for the long lifetime component (Figure 4.6c). The same biexponential behaviour was found for the PSBs of the weakly coupled reference film (representative histogram in Figure 4.6b). The transients of the E_{11} exciton and Y_1 PSB were detection limited. The biexponential decay of the weakly coupled reference is in accordance with the corresponding SWCNT literature. For individual SWCNTs, the short lifetime component has been attributed to the decay of the E_{11} population through radiative and non-radiative channels followed by a slower decay attributed to the redistribution of the exciton population between bright and dark states.^{125, 144} The shorter lifetime of the E_{11} decay compared to the PSBs agrees with the underlying SWCNT relaxation processes (see Background, section 2.3.2 for details). The temporally resolved PSBs exhibited lifetimes between 8 and 80 ps for the short lifetime component and 100 to 300 ps for the longer lifetime component (Figure 4.6d).

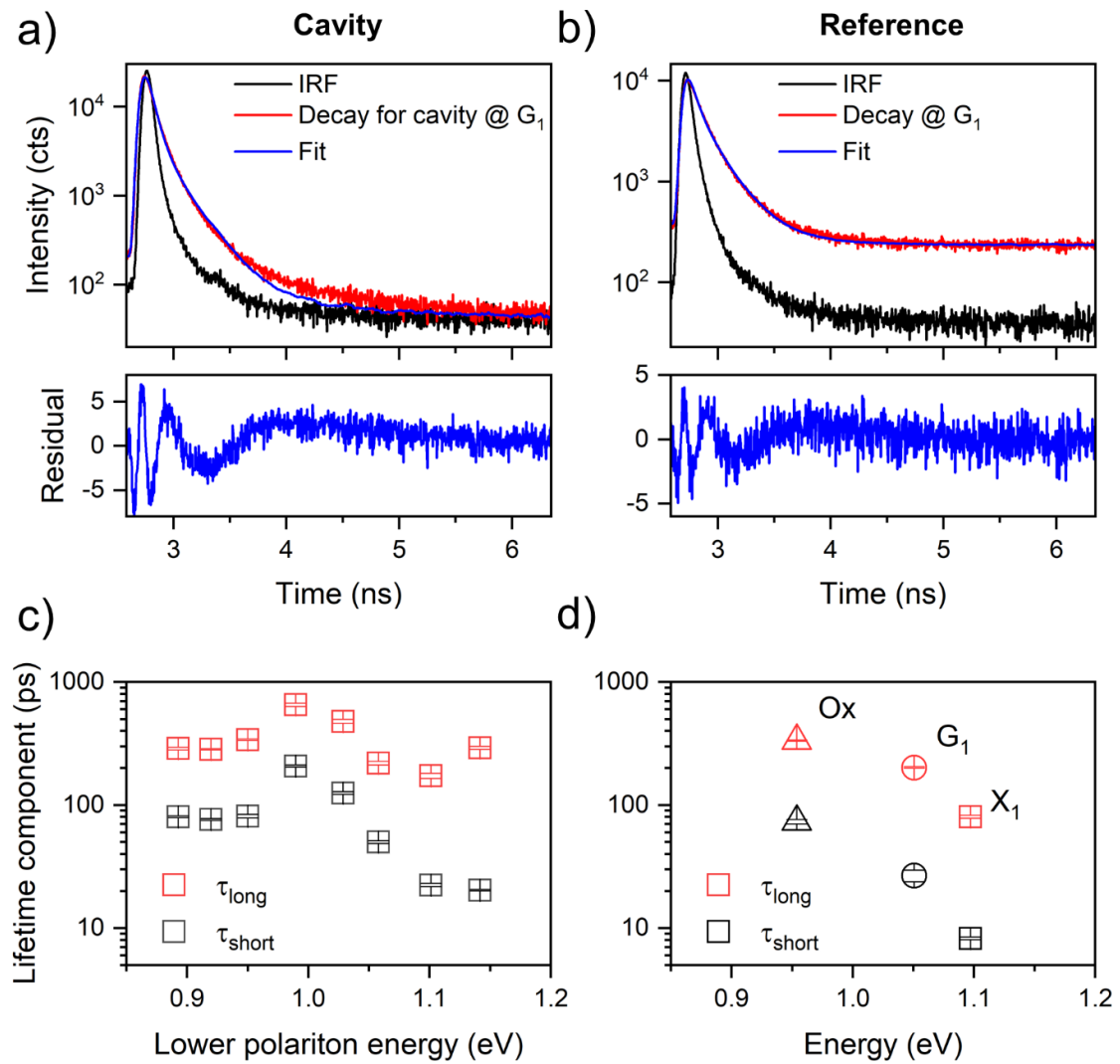


Figure 4.6 TCSPC timetraces (red lines) for a cavity tuned to the G_1 sideband (a) and the respective reference (b). Indicated are the IRF (black line) and the biexponential deconvolution with residual (blue lines). c) depicts the long and short fluorescence lifetime components obtained for the oxide spacer microcavities with detunings from -55 to -355 meV. d) depicts the PSB fluorescence lifetimes measured for the reference. Error bars represent the uncertainty of the biexponential deconvolution.

To interpret the obtained lifetime data, the following kinetic considerations are made: In the presented microcavities, the polariton radiative decay of the microcavities is on the order of a few tens of femtoseconds (≈ 30 fs, calculated by linewidth). Therefore, the significantly longer lifetimes observed in the TCSPC experiments can be assigned to the underlying rate limiting step

of the polariton population.⁵⁷ Since population of the exciton reservoir should occur very rapidly after excitation of the E_{22} transition (575 nm) due to ultrafast conversion from the E_{22} to E_{11} manifold (< 1 ps)¹¹⁰, the rate limiting step is assumed to be transfer from the exciton reservoir into polariton states. In case of radiative pumping (Figure 4.1, process iii), the observed fluorescence lifetimes should be approximately equal the lifetimes observed for the underlying emitter (see Background, section 2.2.2 for details). For this it is assumed, that the rate of radiative decay from the reservoir states is not affected by the polaritons or the cavity. Depicting radiative pumping as non-adiabatic coupling between the fluorescing state and the polariton makes this assumption plausible⁶⁶, as in this description, no true emission event is involved. Experimental evidence for is given later in section 4.9. In case of vibrationally assisted scattering (VAS) (Figure 4.1, process ii), a significant reduction of the observed polariton fluorescence lifetime compared to the decay of the weakly coupled reference should be observed⁹⁸ considering an estimated scattering rate of $(90 - 500 \text{ fs})^{-1}$ for this process (see Appendix, section 8.1.2 and 8.1.3 for detailed calculation). In the latter scenario, the VAS mechanism constitutes an additional non-radiative decay channel for reservoir excitons into the polariton modes and the overall measured cavity fluorescence decay would be shortened substantially. The data relevant for this comparison is summarized in Figure 4.7.

Figure 4.7a relates the LP fluorescence decay at $k_{\parallel} = 0$ for the different oxide spacer cavities to the fluorescence decays obtained for the reference film. In the top panel, the reference spectrum of a weakly coupled SWCNT film is shown. The different PSBs are highlighted as components of a multi-Lorentzian fit to show their contributions to the SWCNT emission spectrum. The PSB timetraces were recorded at by selecting the respective emission maximum. The centre panel depicts the LP emission spectrum, that was temporally resolved by the TCSPC experiment. The corresponding transients are given in the lower panel. The LP energy was again adjusted to be equivalent to 80 nm SWCNT film thickness.

Figure 4.7b shows the experimentally obtained short lifetime components for the strongly coupled SWCNT microcavities (blue diamonds) and the weakly coupled reference film (coloured squares). The lifetimes obtained for cavity different cavity detunings are equal or even slightly longer compared to the corresponding weakly coupled sidebands (Figure 4.7b, diamonds vs. squares). Similar trends were found previously^{57, 92} for the fluorescence lifetimes of strongly coupled cavities compared to their weakly coupled references and were interpreted as evidence for radiative pumping by Grant *et al.*⁸⁰ The calculated fluorescence lifetimes expected in the VAS limit (black circles), that is in absence of radiative pumping, is by orders of magnitude faster. Based on this, also a competition between VAS and radiative pumping in case of the X_1 and G_1 sidebands can be excluded. Furthermore, the biexponential decay for both, microcavity and reference, excludes a scenario in which the LP decays on the same timescale as the fluorescence from the sub-bandgap states, as it would lead to a triexponential decay. This is in accordance with the ultrashort LP lifetime calculated by linewidth (grey triangles). Together with the aforementioned arguments, this leads to the conclusion that radiative pumping is the most suitable model for the observed SWCNT exciton-polariton fluorescence dynamics.

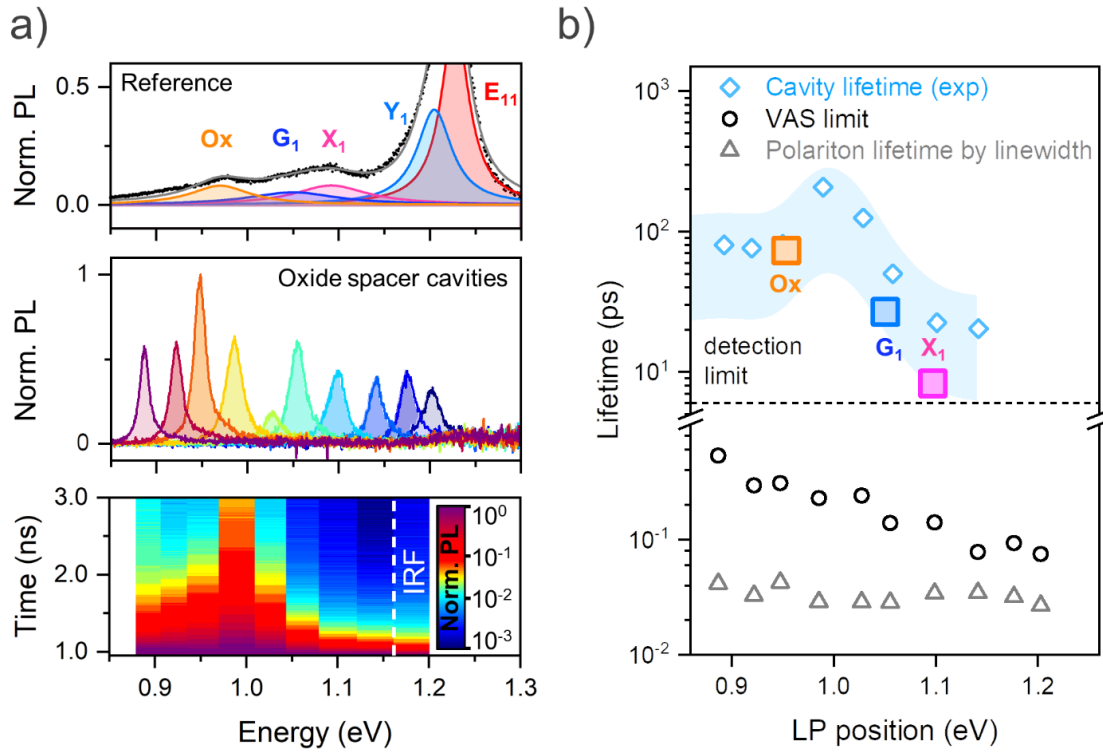


Figure 4.7 a) Correlation between reference and cavity fluorescence decay **Top panel:** Multi-Lorentzian fit to the PL of a pristine SWCNT film. **Centre panel:** $k_{\parallel}=0$ emission of the oxide spacer cavities (solid lines). The emission is normalized to the detuning with maximum intensity. **Lower panel:** fluorescence transients of the cavity emission shown in the centre panel. The instrument response function (IRF) is given for comparison. **b)** Comparison between experimental and calculated fluorescence lifetimes as a function of LP position. The blue shaded area error indicates the measurement accuracy based on IRF.

4.6 Strong coupling of SWCNTs with luminescent sp^3 defects

In the previous sections, radiative pumping was found to be the dominating population mechanism in SWCNT exciton-polaritons, governing the polariton fluorescence decay and explaining the observed LP emission maxima. Since radiative pumping is the rate-limiting step of the polariton population, the polariton population is also limited by the SWCNT PLQY. However, the SWCNT PLQY can be increased by synthetically introducing luminescent sp^3 defects into the SWCNT lattice.^{49, 50} These artificial defects trap mobile excitons, protecting them against diffusive quenching,¹⁵⁴ and exhibit bright, red-shifted (> 150 meV) emission peaks

(for a detailed information see Background, section 2.3.3). As only low sp^3 defect densities are required to increase the SWCNT PLQY, functionalized SWCNTs still exhibit strong absorption at the E_{11} resonance, which should allow to strongly couple the E_{11} exciton to a cavity. In the following, cavities containing 4-bromophenyl-functionalized SWCNTs are presented. These sp^3 defects possess two luminescent configurations termed E_{11}^* and E_{11}^{*-} . Upon strong coupling of the functionalized SWCNTs, the resulting LP branch could be radiatively pumped by the luminescent sp^3 defects at negative detunings (< -150 meV, Figure 4.8) and increase the polariton population compared to pristine SWCNTs. Furthermore, demonstrating polariton population by sp^3 defects serves as a control experiment for radiative pumping, as the defects can only contribute radiatively to the polariton population.

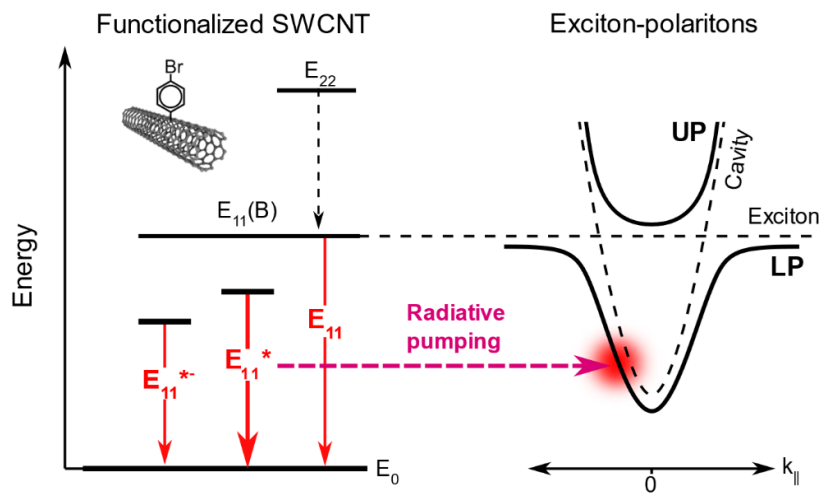


Figure 4.8 Schematic of the polariton population in sp^3 -functionalized SWCNT exciton-polaritons for a cavity tuned to the E_{11}^* defect emission.

For this, a set of oxide spacer microcavities was prepared, identical to the set presented in section 4.3 but with 4-bromophenyl-functionalized SWCNTs⁵⁰ as an active layer. The functionalization was performed on the same polymer-sorted (6,5) SWCNTs dispersion that used for the samples in section 4.3, to exclude batch to batch variations (Experimental, section 3.1.1). The functionalization degree was chosen to be moderate in order to maximize the total SWCNT PLQY, since high defect densities may reduce the PLQY again.⁵⁰ The reactant concentration

screening is shown in Figure 4.9a, depicting emission spectra of the respective SWCNT dispersions functionalized using 4-bromobenzenediazonium tetrafluoroborate. Based on the screening, a reactant concentration of $0.369 \text{ mmol L}^{-1}$ was chosen to functionalize the SWCNTs. For the employed moderate defect density, it can be assumed, that the overall SWCNT lattice is only slightly disturbed.⁵⁰ Upon functionalization, the contribution of mobile E_{11} excitons to the SWCNT absorption is reduced ($\approx 40 \%$, Figure 4.9b), as they are efficiently channelled to the sp^3 defects, while no additional sp^3 defect absorption can be observed (region around 1.086 eV , Figure 4.9b), due to the low defect concentration. The cavities containing functionalized SWCNTs are discussed in the following paragraph.

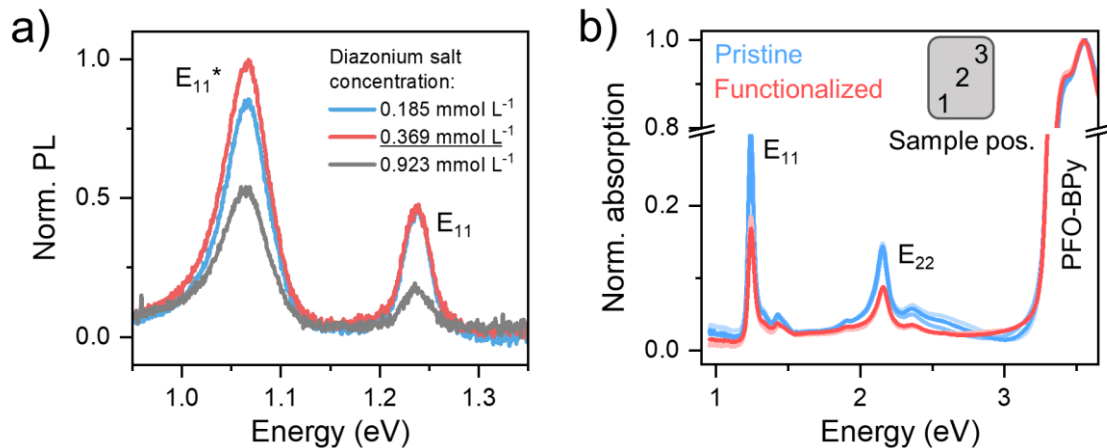


Figure 4.9 Functionalization of (6,5) SWCNTs. **a)** Screening of the diazonium salt concentration. The optimum concentration is underlined. **b)** Absorption spectra of the reference SWCNT films with pristine and functionalized SWCNTs at each three different positions on the sample. The spectra were normalized to the PFO-BPy absorption to account for film thickness variations.

The angle-resolved reflectivity and PL data of the oxide spacer cavities with functionalized SWCNTs is shown in Figure 4.10. The reflectivity data obtained for functionalized SWCNTs exhibits a clear splitting at the E_{11} exciton energy (Figure 4.10), indicating strong coupling. At the defect energy around 1.05 eV , no splitting is observed, in accordance with the absence of defect absorption in the reference film spectra (Figure 4.9b). Hence, the sp^3 defects are weakly coupled, which is the required prerequisite for radiative pumping. As for strongly coupled pristine

SWCNTs, emission is only observed from the LP branch (Figure 4.10). The LP emission varies strongly for different oxide spacer thicknesses or detunings, respectively. Especially around 1.05 eV, that is the energy of the E_{11}^* emission, the LP emission intensity is strongly increased. This already indicates radiative pumping from defect states and the corresponding time-dependent data is presented later in section 4.8.

The angle resolved data in Figure 4.10 was analysed analogously to the data presented in section 4.3. Figure 4.11 shows the corresponding results of a CO-fit to the angle-resolved reflectivity. The cavity energy was calculated from the average effective refractive index from the CO-fit (Figure 4.11, black dashed line) and again agrees well with cavity positions obtained by the fit. The average Rabi splitting for cavities with functionalized SWCNTs is about 80 % of that obtained for cavities with pristine SWCNTs. The reduced coupling strength for the functionalized SWCNTs can be attributed to the reduction of E_{11} excitons, due exciton trapping at defects (Figure 4.9). The Rabi splitting scales with the square root of the number of strongly coupled emitters. Using the reduction of E_{11} absorption upon functionalization (40 %, Figure 4.9b) as a measure for the reduction of strongly coupled emitters, the reduction in Rabi splitting for the functionalized SWCNT can be estimated to be $\sqrt{60} \% \approx 77 \%$ of pristine value. The observed Rabi splitting reduction of 80 % agrees well with this estimation.

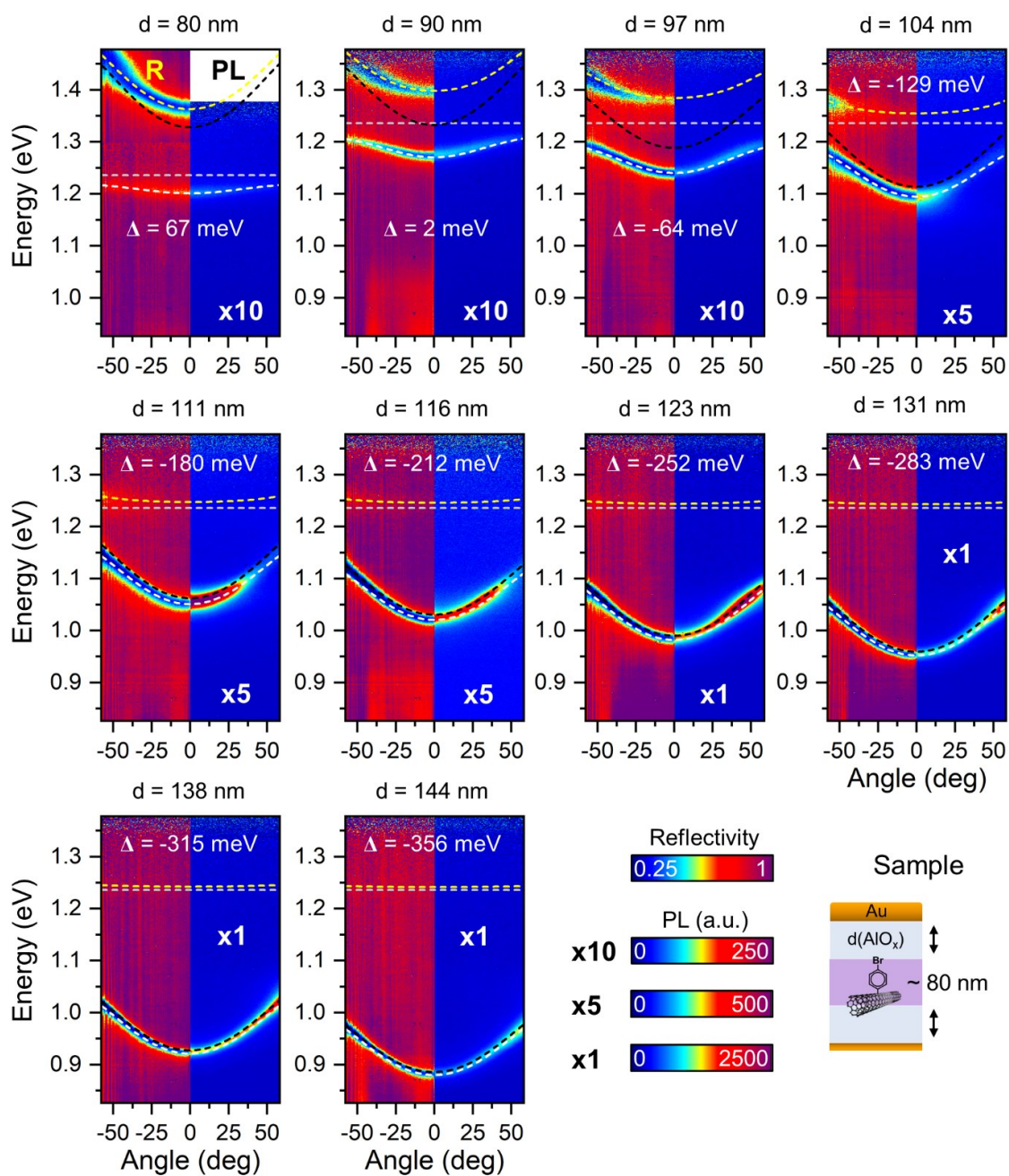


Figure 4.10 Angle-resolved reflectivity (R) and photoluminescence (PL) spectra of ten strongly coupled oxide spacer cavities filled with functionalized SWCNTs. Spacer thickness d and detuning Δ are given for each data set. The data was fitted to the CO-model (dashed lines) and the results are shown in Figure 4.11.

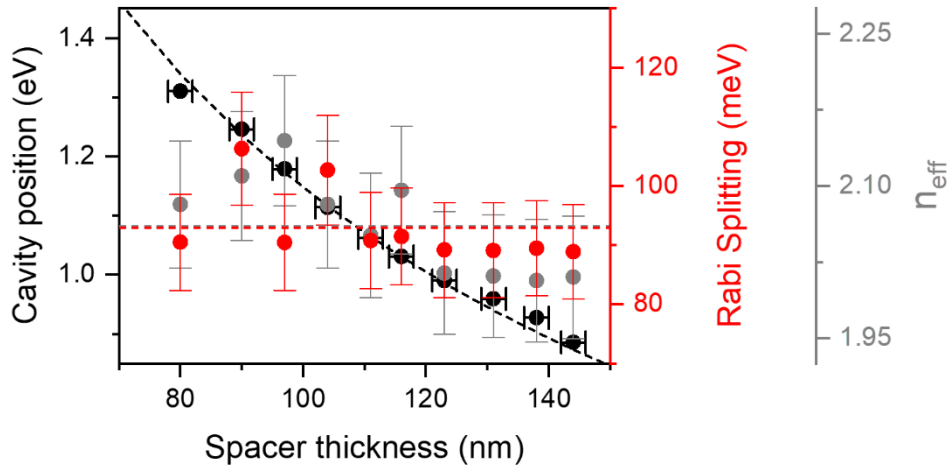


Figure 4.11 CO-fit results of the angle-resolved reflectivity of the oxide spacer cavities with functionalized SWCNTs shown in Figure 4.10. The calculated cavity position is given as black dashed line. The average values of the Rabi splitting and the effective refractive index are given as red and grey dashed lines, respectively.

4.7 Pristine vs. sp^3 -functionalized SWCNTs in the strong coupling regime

In this section strongly coupled pristine SWCNTs are compared with functionalized SWCNTs in detail. For this purpose, the focus lies on the zero-detuning case, in which the cavities are tuned to the E_{11} transition, and a scenario, in which the cavities are tuned to a phonon sideband and a sp^3 defect emission band, respectively.

Figure 4.12a and c depict the angle-resolved reflectivity and PL spectra of microcavities containing the two types of SWCNTs tuned to the E_{11} transition ($\Delta \approx 0$). Both samples exhibit strong coupling, which is apparent from the splitting of the cavity mode into UP and LP modes at the exciton resonance, as mentioned before. The CO-fit yields a Rabi splitting of 128 meV for pristine and of 106 meV for functionalized SWCNTs ($\approx 80\%$ of the pristine value). As mentioned in the previous section, this can be attributed to the lower E_{11} absorption (Figure 4.9). Both, pristine and functionalized SWCNTs, only exhibit PL from the LP branch. For the zero-detuning case, the sample with functionalized SWCNTs shows about 43% less emission than the sample

with pristine SWCNTs. This reduction can be attributed to the lower E_{11} emission intensity for functionalized SWCNTs, which scales with the reduction in E_{11} absorption (compare Figure 4.9).

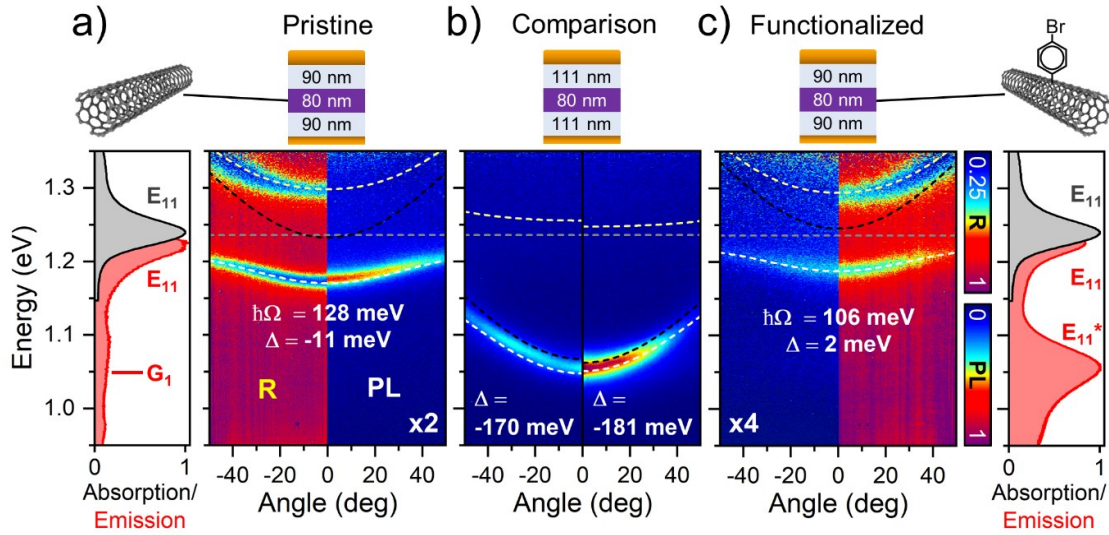


Figure 4.12 Comparison between pristine and functionalized SWCNTs in the strong coupling regime. **a)** Emission and absorption of a reference film (**left**) and angle-resolved cavity reflectivity (R) and PL spectra of a microcavity (**right**) containing pristine SWCNT. **b)** Angle-resolved LP spectra for cavities containing pristine (**left**) and functionalized SWCNTs (**right**), tuned to G_1 and E_{11}^* transition, respectively. **c)** Angle-resolved PL and reflectivity spectra of a microcavity (**left**) and emission and absorption of a reference film (**right**) containing functionalized SWCNTs. The cavity stack is given at the top of each data set.

Figure 4.12b shows the angle-resolved PL of microcavities with pristine and functionalized SWCNTs tuned to the G_1 and E_{11}^* bands, respectively, corresponding to a detuning of $\Delta \approx -180$ meV. The angle-resolved reflectivity is omitted for clarity and can be found in the corresponding full data sets (Figure 4.3 and Figure 4.10). For this detuning the LP emission from the microcavity with functionalized SWCNTs is three times stronger than the LP emission from the cavity with pristine SWCNTs. Because the E_{11}^* transition can only contribute to the polariton population radiatively, the enhanced intensity at this spectral position of the LP branch is indicative of radiative pumping. The considerably higher intensity of the LP emission for functionalized SWCNTs compared to pristine SWCNTs implies an increase in polariton

population and more details on this are given section 4.10. To give definitive evidence for radiative pumping by sp^3 defects, time-resolved data is presented in the next section.

4.8 Time-dependent data of strongly coupled sp^3 -functionalized SWCNTs

In the previous section, strongly coupled cavities with sp^3 -functionalized SWCNTs were presented. In the angle-resolved PL data the polariton emission increased, when the LP was tuned to the sp^3 defect emission. To show, that the underlying mechanism is radiative pumping, in this section, the time-dependent fluorescence decay of cavities with functionalized SWCNTs is presented. The data was recorded analogously to section 4.5. The kinetic arguments made previously also apply for luminescent defects, that is, that the fluorescence dynamics of the defects are rate limiting to polariton population in case of radiative pumping.

The fluorescence dynamics of the E_{11}^* and E_{11}^{*-} transitions of functionalized (6,5) SWCNTs with sufficiently low sp^3 defect densities, as is the case here, can be considered to be decoupled from the E_{11} exciton dynamics. The sp^3 defect fluorescence decay also exhibits a biexponential decay similar to SWCNT, but with elongated lifetimes due to suppression of diffusive quenching (for a detailed information see Background, section 2.3.3). The short lifetime component has been interpreted as the redistribution between trapped bright and dark excitons and the long lifetime component as the subsequent decay through radiative and non-radiative channels^{153, 181}

Figure 4.13 presents the analysis of the time-dependent fluorescence data of the oxide spacer microcavities with functionalized SWCNTs introduced in section 4.6 and the reference data recorded for a weakly coupled reference film of functionalized SWCNTs. All fluorescence timetraces were well-described by a biexponential decay convoluted with the instrument response function (IRF). Figure 4.13a and b show representative histograms and fits of a cavity tuned to the E_{11}^* transition and a reference film, respectively. For the microcavities, the extracted lifetimes ranged from 20 to 100 ps for the short lifetime component and from 200 to 300 ps for the long lifetime component (Figure 4.13c) for varying LP positions or detunings respectively. For the

reference film of functionalized SWCNTs, the short lifetime components of the E_{11}^* and E_{11}^{*-} transitions were found to be around 60 and 100 ps, while the long lifetime components were found to be around 200 and 300 ps (Figure 4.13d).

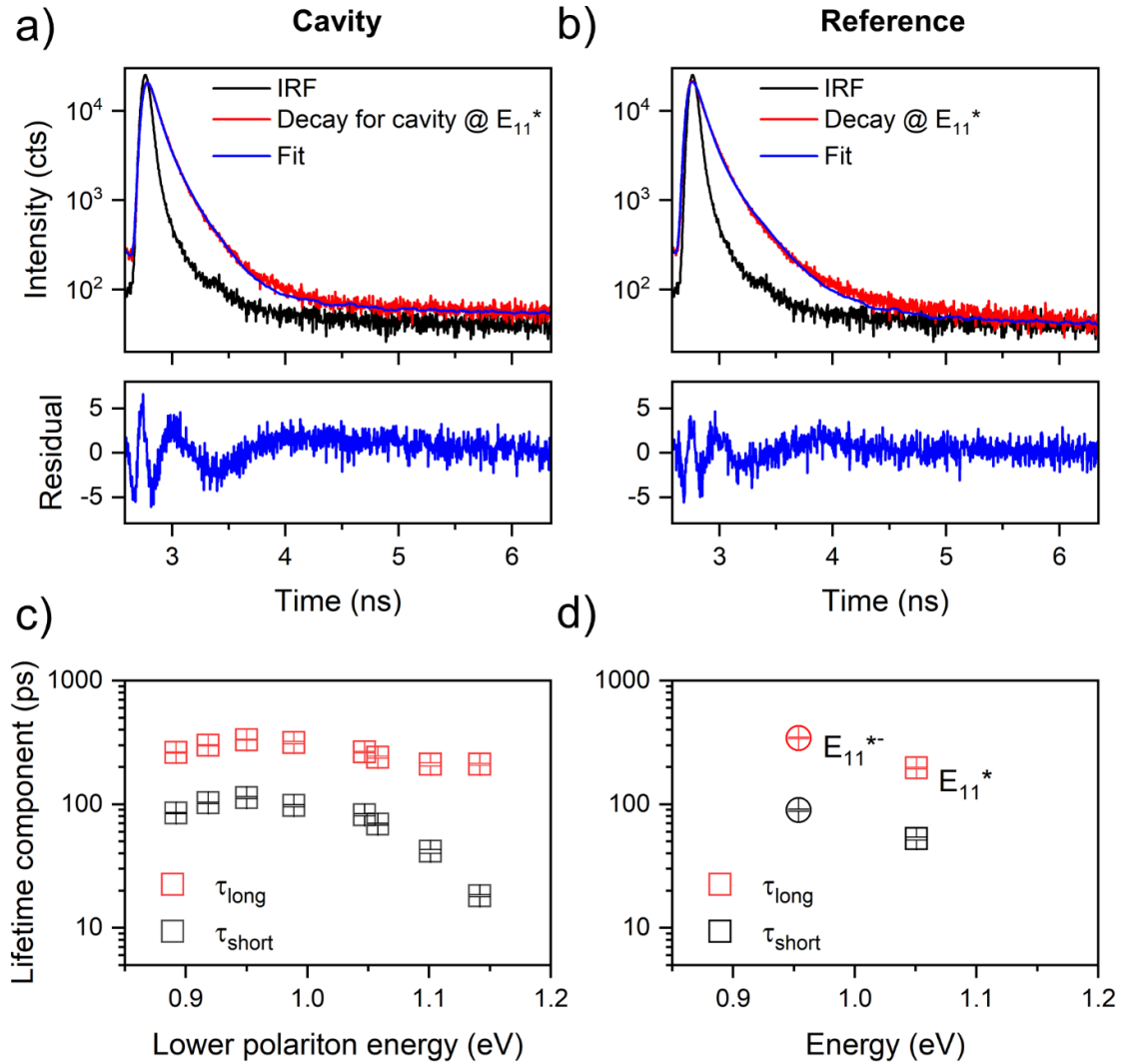


Figure 4.13 TCSPC timetraces (red lines) for a cavity tuned to the E_{11}^* emission (a) and the respective decay of a reference film (b). Indicated are the IRF (black line) and the biexponential deconvolution with residual (blue lines). c) Long and short fluorescence lifetime components obtained for the oxide spacer microcavities with detunings from -64 to -356 meV. d) E_{11}^* and E_{11}^{*-} fluorescence lifetimes measured for the reference. Error bars represent the uncertainty of the biexponential deconvolution.

In Figure 4.14 the lifetime data presented in Figure 4.13 is correlated to the lifetime data of the reference based on the energy of the LP emission maximum. The top panel in Figure 4.14a shows the emission spectrum of the weakly coupled reference film. The defect emission peaks E_{11}^* and E_{11}^{*-} are indicated as the components of a multi-Lorentzian fit to the spectrum for clarity. The centre panel of Figure 4.14a shows the $k_{||}=0$ emission spectrum for the different cavity samples and the bottom panel shows the cavity fluorescence timetraces recorded at the respective emission maximum. Figure 4.14b presents the thusly correlated short lifetime components of the cavity decay (red diamonds) and the E_{11}^* and E_{11}^{*-} defect emission. The fluorescence decay in the VAS limit (black circles) and the intrinsic polariton lifetime calculated by linewidth (grey triangles) are given for comparison. Within the error of the TCSPC experiment, the LP fluorescence lifetimes approximately equal those recorded for the weakly coupled reference. Similar to the results of pristine SWCNTs (section 4.5), also the biexponential decay behaviour of the weakly coupled reference is retained (Figure 4.13a and b). The similarity between cavity and reference fluorescence decays strongly suggests radiative pumping by luminescent sp^3 defects. This result further shows, that for strongly coupled SWCNT, the emitter fluorescence dynamics are clearly rate limiting to the polariton emission, even for more long-lived luminescent defect states. Also, it is important to note, that again no lifetime shortening due to the VAS process is observed.

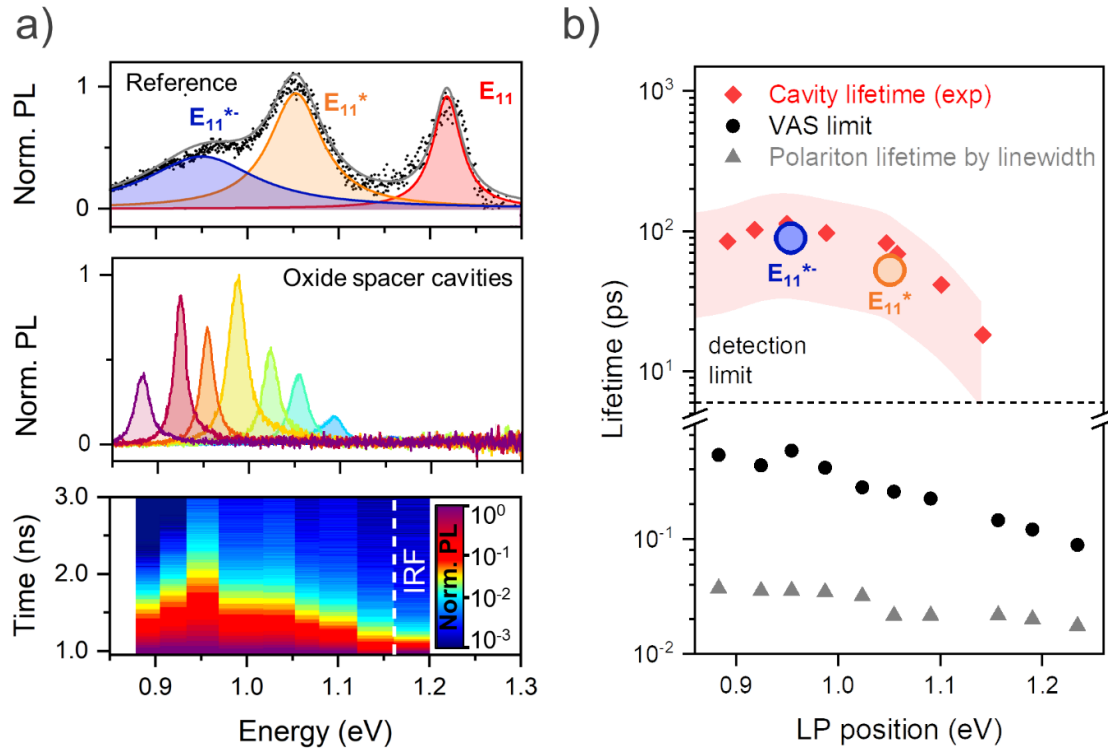


Figure 4.14 a) Correlation between reference and cavity fluorescence decay **Top panel:** Multi-Lorentzian fit to the PL of a functionalized SWCNT film. **Centre panel:** $k_{||}=0$ emission of the oxide spacer cavities (solid lines). The emission is normalized to the detuning with maximum intensity. **Lower panel:** fluorescence transients of the cavity emission shown in the centre panel. The instrument response function (IRF) is given for comparison. **b)** Comparison between experimental and calculated fluorescence lifetimes as a function of LP position. The red shaded area error indicates the measurement accuracy based on the IRF.

4.9 Absence of the Purcell effect

Thus far, it was assumed that the emission attributed to the LP branch only arises from the radiative decay of occupied polariton states. However, polaritons are composite particles and their photonic fraction is an electromagnetic mode in the classical sense. Therefore, the LP mode could enhance radiative transitions of the exciton reservoir *via* the Purcell effect, which would lead to similar emission patterns as polariton population by radiative pumping. Definite experimental evidence for the absence of the Purcell effect could only be obtained from cavities with sp^3 -functionalized SWCNT data, as their slow fluorescence decay is more sensitive towards small increases of the radiative decay. Hence, the following discussion was postponed until now.

In order to show the absence of the Purcell effect, the hypothetical Purcell-induced shortening of the LP fluorescence lifetime was estimated and compared to the experimentally obtained fluorescence lifetime. For this, the LP is treated as a pure electromagnetic mode and the Purcell factor F_P^{2D} is calculated for the cavity tuned to either the X_1 or E_{11}^* transition using⁶⁰

$$F_P^{2D} = \frac{1}{4\pi} \frac{\lambda_{\text{res}}}{n_{\text{eff}} L_c} Q, \quad (45)$$

where λ_{res} (1.1 eV) is the LP wavelength, n_{eff} (2.08) is the effective refractive index, Q_{exp} (44.9) the quality factor of the LP and L_c (271 nm) is the physical length of the cavity. The values were extracted from the experimental angle-resolved reflectivity data of the respective cavities for pristine and functionalized SWCNTs. With this, a theoretical 7-fold increase of the radiative decay for the X_1 and E_{11}^* transitions, respectively, is obtained. To calculate the effect on the fluorescence lifetime, the non-radiative decay is estimated using the sideband PLQY measured for the reference film ($X_1 = 0.2\%$ and $E_{11}^* = 0.5\%$) and the amplitude averaged fluorescence lifetime obtained from the biexponential fit, using

$$\tau_{PL, Purcell} = \left(\left(\frac{1 - \Phi_{\text{ref}}}{\tau_{PL}} \right) + F_P^{2D} \left(\frac{\Phi_{\text{ref}}}{\tau_{PL}} \right) \right)^{-1}, \quad (46)$$

where $\tau_{PL, Purcell}$ is the estimated cavity fluorescence lifetime in case of Purcell enhancement, Φ_{ref} is the PLQY of the pumping sideband measured from the reference film and τ_{PL} is the amplitude averaged lifetime of the fluorescence decay of the respective sideband. Details on the PLQY measurement can be found in Experimental, section 3.2.8. The results are discussed in the following.

Figure 4.15a and b show fluorescence decay transients of the LP tuned to X_1 and E_{11}^* transitions (black solid lines) and the corresponding transients of the reference sample at the same emission energy (red dashed lines). For both transients, the amplitude averaged lifetime is given in the bar chart to the right of each timetrace-plot, together with the calculated lifetime for hypothetical Purcell enhancement by the LP calculated using equation (46). Error bars indicate the uncertainty

of TCSPC measurement (8 ps). For both cavity samples (pristine and functionalized), the LP exhibits a slightly longer fluorescence lifetime (grey bar) compared to the reference (red bar), whereas in case of Purcell-enhancement (green bar) the lifetime should be unchanged (pristine SWCNT) or slightly shorter (functionalized SWCNT) compared to the reference. Especially for LP populated by the long-lived E_{11}^* state, Purcell enhancement is clearly absent (Figure 4.15b).

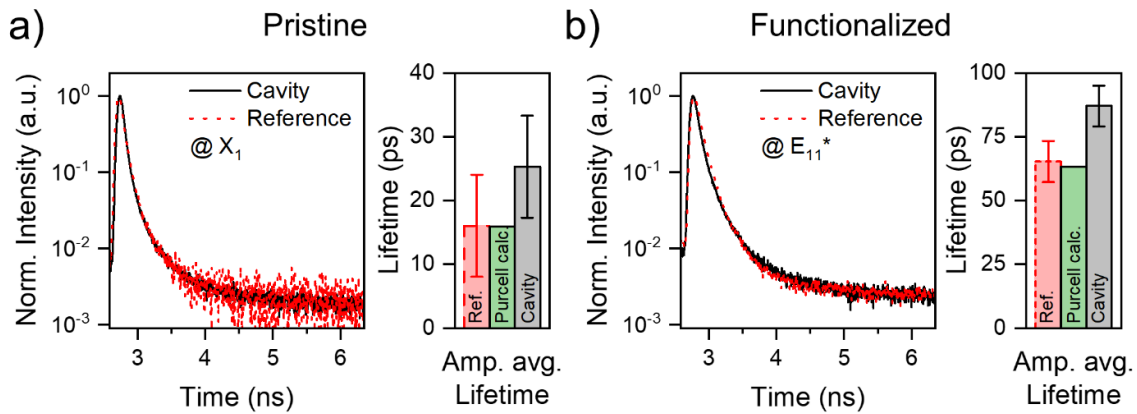


Figure 4.15 Fluorescence decay of microcavities (solid lines) and references (dashed lines) with pristine (a) and functionalized (b) SWCNTs tuned to the at X_1 and E_{11}^* transition, respectively. The amplitude averaged lifetimes for cavity (grey) and reference (red) together with the calculated cavity fluorescence lifetime in case of Purcell enhancement are given for comparison.

Furthermore it should be noted, that all sub-bandgap transitions, resolvable by the TCSPC setup, exhibit slightly longer fluorescence lifetimes in strongly coupled cavities compared to the weak coupling regime (compare Figure 4.7 and Figure 4.14), not only to the cavity samples presented in this section. The absence of the Purcell effect is in accordance with the description of radiative pumping as non-adiabatic coupling between the emitter’s fluorescing state and the LP, as in this picture, no true emission event is involved.⁶⁶ The relaxation towards the fluorescing state is unaffected by strong coupling and coupling from the fluorescing state to the polaritons still competes with the usual non-radiative deactivation processes present in the emitter layer. Assuming that the fluorescing states belong to the polariton dark state manifold,⁶⁶ the observed slight elongation of the cavity fluorescence decay compared to the weakly coupled reference

indicates, that the radiative decay in free space is slightly faster than the population transfer rate to the bright LP.

Absence of the Purcell effect also excludes the occasionally applied notion, that emission might directly leak out of the cavity, e.g. through the transparent part of the polariton mode. Based on this section, it can be concluded that the observed LP emission solely arises from occupied polariton states, which is important for the analysis conducted in the next section.

4.10 Manipulating the polariton population with luminescent sp^3 defects

In the preceding sections, radiative pumping was identified as the dominating population mechanism in SWCNT exciton-polaritons, based on their fluorescence dynamics and angle-dependent emission patterns. In this section, a quantitative assessment of the relative contributions of radiative pumping by the different PSBs and the sp^3 defects to the polariton population is conducted. For this, the polariton population of the LP as a function of detuning is analysed. The polariton population can be extracted from the angle-resolved emission spectra of the cavities, as described in the following.

In order to compare polariton populations between different samples and detunings, the data is corrected for the excitation efficiency of each sample. Firstly, the electric field intensity within each structure is simulated for the employed excitation wavelength (640 nm) using the transfer matrix method and the field intensity within the SWCNT layer is integrated. The thusly calculated overlap between excitation field and active layer is proportional to the change in excitation efficiency between samples of different detuning and includes the intensity loss at the top mirror of each structure. Figure 4.16a shows the simulated E-field intensity within the cavity stack for a sample with small and a sample with large overlap, respectively (top and bottom panel). The different layers are indicated by coloured shadings. For simulation, the SWCNT layer thickness was chosen to match the experimental reflectivity of each sample, which was in average achieved for 80 ± 1.8 nm SWCNT layer thickness. The excitation efficiency correction factors for each

sample were obtained by taking the ratio between the value for the sample with minimum overlap and the sample in question, shown in Figure 4.16b. This procedure has a certain mapping error, because the correction factors from the simulation are assigned to the experimental data based on the nominal oxide layer thickness. The error introduced for the LP position is estimated by multiplying the standard deviation of the SWCNT layer thickness (± 1.8 nm) with the slope of a Bézier interpolation of the data points (Figure 4.16b), yielding the error of the LP position in wavelength units. This error is converted into energy units by calculating the corresponding uncertainty in optical pathlength for the cavity's fundamental mode. Because the dependence of the overlap on detuning cannot be expressed analytically, the error of the correction factor itself was determined heuristically by taking the difference between each correction factor and a B-spline interpolation of the correction factors (Figure 4.16b). A summary of all overlap simulations and the error calculation can be found in the Appendix, section 8.1.4.

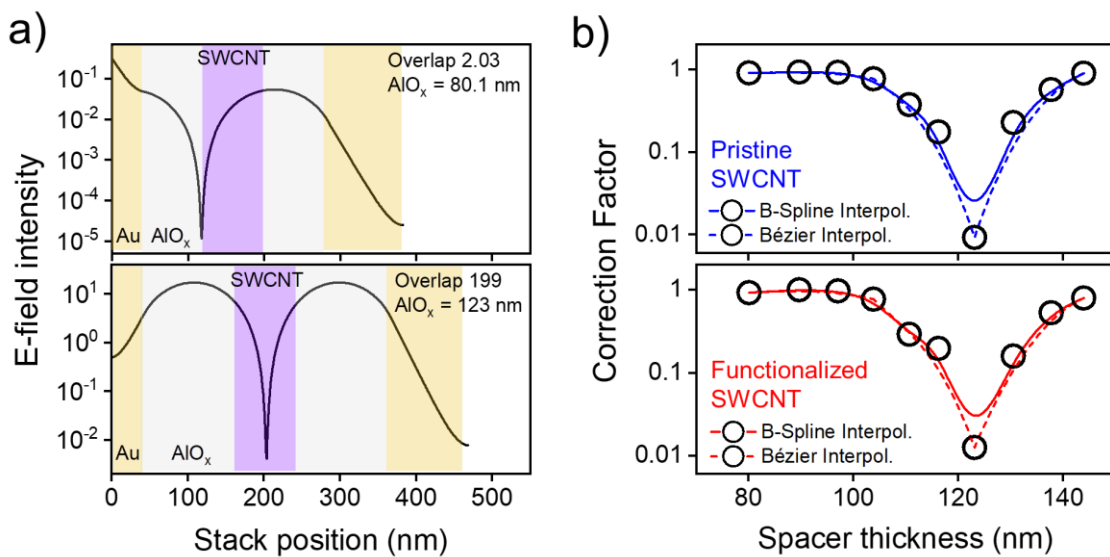


Figure 4.16 a) E-field intensity at the excitation wavelength as a function of stack position within SWCNT filled microcavities for $k_{\parallel} = 0$ with different oxide spacer thicknesses (top and bottom panel). **b)** Correction factors calculated from the overlap between E-field intensity and the active layer for the microcavity sets with pristine (top panel) and functionalized (bottom panel) SWCNTs.

Due to their composite nature, the polariton population N_P is not directly proportional to the emission intensity I_P but to I_P/α^2 , where α is the photon fraction.⁵⁷ The photon fractions α were extracted from the CO-fit results of the experimental reflectivity data and with this the LP population was calculated from LP emission averaged over $\pm 1.5^\circ$ around $k_{\parallel} = 0$. By multiplying the population with respective correction factor, the relative changes between samples can be attributed solely to a change in population efficiency.

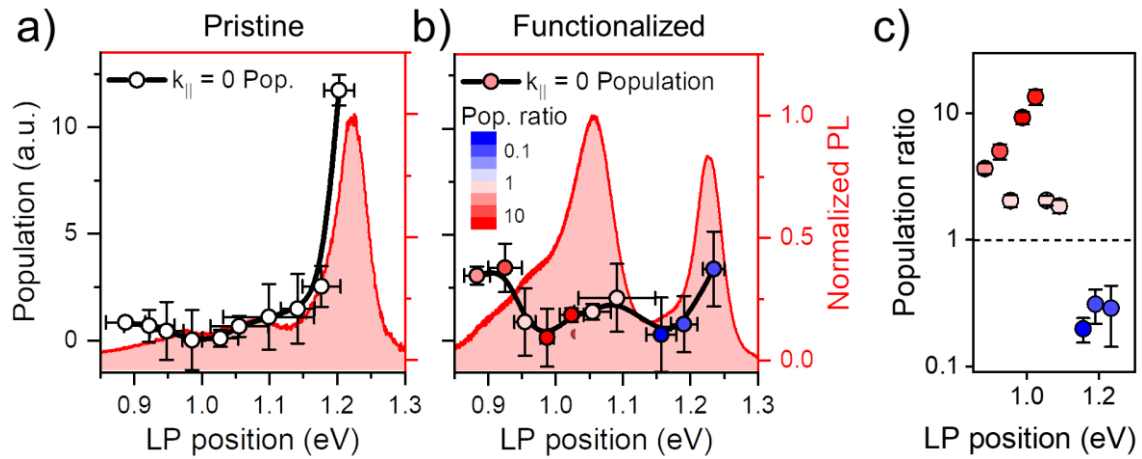


Figure 4.17 Calculated polariton population for SWCNT filled microcavities at $k_{\parallel} = 0$ as a function of LP position for **a)** pristine SWCNTs and **b)** for functionalized SWCNTs. The black solid line is a guide for the eye. For the functionalized SWCNTs, the population change with respect to the pristine sample is shown in red for an increase and in blue for a decrease and the respective values are shown in **(c)**. The PL spectra (red shaded areas) of pristine and functionalized SWCNT films are presented for comparison.

The following section turns to the analysis of the population data. Figure 4.17a and b depict the LP population as a function of LP position for microcavities with pristine and functionalized SWCNTs, respectively. The error bars given in Figure 4.17 account for averaging over $\pm 1.5^\circ$ around $k_{\parallel} = 0$ and the aforementioned error of the excitation efficiency correction. For the functionalized SWCNTs, the relative change in population compared to the respective pristine sample is indicated in red for an increase and in blue for a decrease. The reference PL spectra of pristine and functionalized SWCNT films are given for comparison. A plot of the relative change

in population for cavities with functionalized SWCNTs compared to cavities containing pristine SWCNTs is shown in Figure 4.17c.

In Figure 4.17, the detuning dependent LP populations of both data sets resemble the spectral shape of pristine and functionalized SWCNT emission, except for a deviation below 1.0 eV. This similarity implies that radiative pumping accounts for the majority of the polariton population within the observable emission angles. In the case of microcavities with pristine SWCNTs, the polariton population at $k_{||} = 0$ is maximized when the LP is tuned to the E_{11} emission (Figure 4.17a). While for the functionalized SWCNTs (Figure 4.17b), the population at the same detuning is reduced to approximately one third compared to the pristine SWCNTs. This reduction corresponds to the decrease in E_{11} emission for the functionalized reference films compared to pristine SWCNTs and agrees well with a radiative pumping mechanism. Thus, radiative pumping also dominates the population at small and positive detunings in case of SWCNTs. However, definite evidence would require the temporal resolution of the fluorescence decay of the E_{11} transition, which was not feasible with the available TCSPC setup. Below 1.0 eV, the LP population of the pristine SWCNTs increases slightly and does not follow the emission spectrum. For functionalized SWCNTs, this deviation is even more pronounced (Figure 4.17b). Yet, this deviation cannot be confidently interpreted on the basis of the available data, as the lifetime data shows no significant change at these wavelengths and the ultrafast component of the polariton decay was accounted for using the experimentally determined photon fraction. Therefore, this aspect of the population data remains elusive on the basis of the available data.

Comparing the population of cavities with functionalized SWCNTs to cavities with pristine SWCNTs (Figure 4.17b and c, color-coded symbols), an increase in polariton population for all detunings at which the LP overlaps with the sp^3 defect emission bands is observed. For LPs overlapping with the E_{11} emission, a decrease with respect to the pristine SWCNTs is observed. This reflects the relative change in the emission spectrum from pristine to functionalized SWCNTs, as described earlier. The highest population is found for highly emissive polaritons

(photon fractions > 98%), which is 5-fold higher compared to the corresponding pristine sample (~ 0.92 eV, Figure 4.17). For detunings around 1.0 eV, the highest relative enhancements are found with ratios of about 10-fold (photon fractions > 90%).

The population analysis gives further evidence that radiative pumping dominates the polariton population of pristine and functionalized SWCNTs. Hence, the polariton population is limited by the low SWCNT PLQY. However, this limitation can be overcome by introducing luminescent sp^3 defects which can increase the total SWCNT PLQY up to two-fold.⁵⁰ The population analysis shows, that this may relate to an up to 10-fold increase in the polariton population, depending on the spectral position. Functionalization of SWCNTs with luminescent sp^3 defects therefore offers a unique approach to manipulate and increase the polariton population.

4.11 Summary and conclusion

In this chapter, the population and relaxation of SWCNT exciton-polaritons with focus on radiative states was investigated. It was found that radiative pumping constitutes the dominant population mechanism in this system. The polariton fluorescence decay closely resembles the biexponential decay of the weakly coupled SWCNT reference at various wavelengths, thus excluding vibrationally assisted scattering. The spectral emission shape of both, pristine and functionalized SWCNTs, can account for the majority of the observed polariton population within the investigated range of detunings. Furthermore, the dominant role of radiative pumping indicates that polariton population is mainly limited by the low PLQY of SWCNTs. The introduction of moderate densities of luminescent sp^3 defects to the SWCNTs increases the PLQY while only slightly reducing the absorption of the fundamental E_{11} transition and without producing new absorption bands in film. Therefore, microcavities containing functionalized SWCNTs exhibit strong coupling with the same polariton branch-structure as those with pristine nanotubes and at only a slightly reduced Rabi splitting (~ 20 %). It was found that functionalized SWCNTs can be employed to increase the polariton population at highly emissive detunings (photon fractions > 90%) up to 10-fold. Furthermore, the defect emission can be spectrally tuned

by changing the substituents and the binding pattern,^{182, 183} and thus, may serve as a viable route to tune and increase the polariton population.

5 Ultrafast dynamics of SWCNT exciton-polaritons

In the previous chapter it was found, that SWCNT exciton-polaritons are predominantly populated radiatively, following the fluorescence dynamics of the underlying emitter. In this chapter, strongly coupled (6,5) SWCNTs are investigated with pump-probe spectroscopy to increase the time resolution towards the intrinsic polariton lifetime and observe ultrafast dynamics on the femtosecond timescale. By measuring the cavity transient transmission response, also non-emissive states are observed, revealing a polariton intrinsic feature that is found to be a direct UP to biexciton transition. Furthermore, the dynamics of this transition shed light on the population transfer from the dark polariton states to the UP state. The time-dependent data presented in this chapter were recorded by Dr. Zhouran Kuang and analysis of the data was conducted under the supervision of Dr. Tiago Buckup. A manuscript based on the work presented here is in preparation.

5.1 Introduction

In the previous section, the polariton fluorescence decay was found to be similar to the fluorescence decay of the weakly coupled emitter. This can be explained by the radiative pumping mechanism, that is, that the emitter dynamics are not changed in the strong coupling regime within the time-resolution of the TCSPC experiment (~ 8 ps) and the excited state relaxes down to the fluorescing state with the dynamics of the weakly coupled emitter (see Background, section 2.2.2 for details). For radiatively pumped polaritons, one would therefore expect, that the modification of the emitter dynamics should be confined to the timescale of the polariton intrinsic lifetime, during which bright polaritons and dark states coherently exchange energy. In this chapter, the time-resolution is therefore increased by measuring the cavity transient transmission by pump-

probe spectroscopy, in order to explore, whether the SWCNT dynamics are modified by strong coupling at shorter timescales.

The timescale of coherent energy exchange between dark and bright states can be estimated from the typical dephasing time of photon and emitter.¹⁸⁴ In metalclad cavities, the fast photon decay is the major contribution to dephasing. Considering photon lifetimes of few to tens of femtoseconds, the coherent regime is difficult to resolve, even with the shortest available laser pulses in the relevant spectral range.¹⁸⁵ However, multiscale molecular dynamics simulations of rhodamine molecules in a cavity showed reversible population transfer between long-lived dark states and bright polaritons, leading to an extension of the bright polariton lifetime to over 100 fs.⁵⁸ This could be confirmed by two-dimensional Fourier transform pump-probe experiments, which allow for ultrashort broadband pump pulses (~ 20 fs), revealing coherent energy exchange between UP, LP and dark states during the first 150 fs after excitation. This experiment demonstrated the modification of the emitter dynamics by a strongly coupled metalclad cavity beyond the ultrashort photon lifetime.¹⁸⁶

Beyond the extended coherent timescale (~ 150 fs, accessible by conventional transient transmission (TT) and transient reflectivity (TR)), the polariton transient response was found to follow that of the underlying emitter by all studies conducted so far.^{91-93, 187-189} Even for J-aggregates, in which the polariton fluorescence decay should be faster than that of the emitter, owing to vibration assisted scattering¹⁰⁰, the polariton transient response is essentially emitter like.^{92, 187} The reason for this might be the low PLQY of strongly coupled J-aggregates ($\sim 0.1-1$ %).¹⁸⁷ If the PLQY of the strongly coupled cavity is low, the contribution of excitons populating polaritons and decaying radiatively only constitutes a minor contribution to the whole exciton population monitored in transient transmission or reflectivity. Consequently, a change in emitter-dynamics caused by radiative decay may only be observed for exciton-polaritons possessing high PLQYs and that are not populated radiatively. For systems not meeting these criteria, only polariton intrinsic transitions may show spectral signatures that are not simply explained by the

relaxation of the underlying emitter. This can be either a transition into a polariton excited state or a transition from a bright polariton state into a weakly coupled emitter state. Transitions into excited polariton states have so far only been reported in the coherent regime^{190, 191}, and the only report¹⁹² beyond this timescale suffers from conceptual issues, which is explained in section 5.3. A transition from a polariton state into a weakly coupled excited state has so far not been observed for polaritons based on disordered semiconductors.^{91-93, 187-189} However, such a transition is known for quantum-well (QW) exciton-polaritons. ZnSe exhibits a polariton to biexciton transition under excitation with circular polarized light at cryogenic temperatures,^{193, 194} given the cavity normal-mode splitting is smaller than the biexciton binding energy.¹⁹³ Owing to the large biexciton binding energy of 130 meV⁵³ in (6,5) SWCNT such a transition may be observable for strongly coupled SWCNTs under excitation with linearly polarized light.¹³⁴

In the following, a pump-probe technique is employed to record the transient transmission of strongly coupled SWCNT metalclad cavities. Firstly, this technique provides the required time resolution to investigate the ultrafast polariton dynamics, but it also allows detection of non-emissive states such as the SWCNT biexciton.¹³⁴ Transfer matrix (TM) simulations are used to account for non-polaritonic changes in cavity transmission caused by the transient refractive index change induced by the SWCNT bleach. Thus, it becomes possible to distinguish possible polariton excited state absorption from SWCNT bleach induced features, such as a polariton to biexciton transition. By comparing transient dynamics for resonant polariton and off-resonant E_{22} excitation, the direct nature of polariton to excited emitter state transitions can be confirmed.

5.2 Transparent metalclad cavity

In order to perform pump-probe measurements in a conventional transient absorption setup, the SWCNT cavity design was chosen to be transparent, that is, a symmetric cavity stack without a highly reflective bottom mirror and a transparent glass substrate (Figure 5.1a). For both cavity mirrors, a 30 nm gold layer was chosen, allowing for sufficient transmission through the sample, yet providing enough reflectivity for strong light-matter coupling. The SWCNT layer, (6,5)

SWCNT in a PFO-BPy matrix, was chosen to be 30 nm thick, in order to reduce the Rabi-splitting sufficiently below the biexciton binding energy. Furthermore, thin SWCNT films allow for a reduced cavity wedge, which is necessary due to the large spot size of the focused pump beam ($\sim 250 \mu\text{m}$, FWHM) as well as limited positioning precision in the pump-probe setup (described in the Experimental, section 3.2.10). The SWCNT film was centred by symmetric aluminium oxide spacers (120 nm) at the field maximum of the $\lambda/2$ cavity, minimizing the amount of uncoupled SWCNTs, which could contribute to the cavity transient response and mask the dark state nature of the exciton reservoir. The cavity tuning was chosen to be negative, in order to increase overlap between the exciton reservoir and UP and allow for sufficient coupling in case of off-resonant excitation. A detailed description of the cavity preparation can be found in the Experimental, section 3.1.3.

Figure 5.1b depicts the steady state angular resolved reflectivity (R) and photoluminescence (PL) for the sample described above as recorded by Fourier imaging in p -polarization (see Experimental, section 3.2.2). The sample was in the strong coupling regime as evident from the anti-crossing at the exciton energy in reflectivity (Figure 5.1b, R). A coupled oscillator fit to the UP and LP mode in reflectivity yielded a Rabi splitting of 80 meV. From the LP linewidth the quality-factor was estimated to be around 25, which corresponds to a bright polariton lifetime of 15 fs and which will be referred to as the intrinsic polariton lifetime in the following. The PL was recorded under off-resonant excitation (640 nm) with a continuous wave laser diode. As in the previous chapter, emission is only observed from the LP (Figure 5.1b, PL) with maxima at the red flank of the E_{11} emission and the X_1 sideband, indicative of radiative pumping, whereas no emission from the UP is observed. Note that although both, LP and UP, overlap with the E_{11} emission, in case of the UP, the concurrent overlap with the E_{11} absorption leads to efficient non-radiative relaxation of the UP (compare Figure 5.1d).⁵⁸

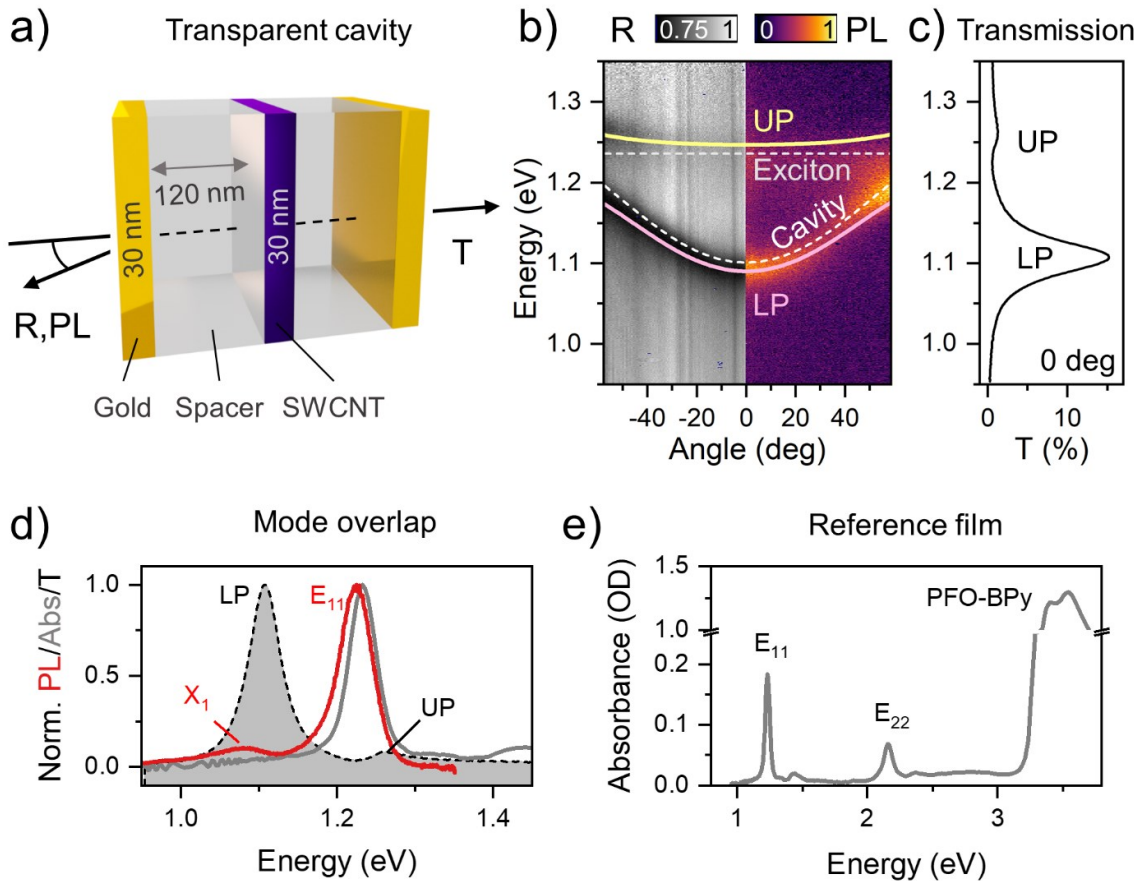


Figure 5.1 **a)** Schematic of the transparent cavity stack, glass substrate is omitted for clarity. **b)** Angle-resolved steady state reflectivity (R) and photoluminescence (PL) of strongly coupled (6,5) SWCNT. **c)** Steady state transmission spectrum of the sample in (b) under normal incidence. **d)** Mode overlap between polaritons shown in (c) with weakly coupled SWCNT emission and absorption. **f)** SWCNT reference film absorption spectrum.

In order to illustrate how the angle-resolved polariton modes relate to the transmission modes recorded under normal incidence, Figure 5.1c depicts the transmission of the transparent cavity sample recorded in a commercial absorption spectrometer (see Experimental, section 3.2.1). Figure 5.1c serves as a reference for the polariton mode positions for the transmission pump probe measurements.

As a reference sample, a (6,5) SWNT film was deposited on a glass substrate from the same SWCNT dispersion used to prepare the cavity sample in Figure 5.1a-c and covered with 120 nm aluminium oxide. The SWCNT emission and absorption around the E_{11} transition are shown in

Figure 5.1d, together with cavity transmission at normal incidence. The full absorption spectrum of the SWCNT reference film is shown in Figure 5.1e. The same film was used to record reference transient absorption (TA) data for weakly coupled SWCNTs. The following section introduces pump-probe measurements on cavity samples and the different contributions to their transient response.

5.3 Cavity transient transmission and reflectivity

The difficulty in transient transmission and reflectivity spectroscopy of strongly coupled microcavities is that the information on the polariton population, that is, polariton photoinduced bleaching and absorption, is convoluted with the reflectivity of the cavity sample. Consequently, the observed peaks cannot be analysed as in conventional transient absorption spectroscopy, where the sample reflectivity can be neglected under normal incidence.¹⁹⁵ Note that Virgili *et al.*⁹³ and DelPo *et al.*¹⁹² neglect this issue. In principle, all cavity materials can exhibit transient changes of the refractive index depending on the pump wavelength and fluence, which leads to a change in cavity reflectivity that is not of polaritonic origin.¹⁸⁴ In the following, these contributions are discussed.

Both, the metal mirrors and SWCNTs are electronically excited by the pump wavelengths used here (575 to 1000 nm), whereas the polymer matrix and the oxide spacers are transparent at these wavelengths and cannot be excited directly. Note that the pump fluences after reflection at the top mirror is around $40 \mu\text{J cm}^{-2}$, which is why multi-photon absorption of the polymer matrix and oxide spacer can be neglected.

In the following, the contributions of the transient changes of the gold mirror and SWCNT refractive index upon pump-pulse arrival are assessed. The cavity transient response is simulated using the transfer matrix (TM) scheme to separate the different contributions. This is done for the experimental parameters used here and the simulation results are used as a reference to interpret the experimental data presented later.

5.3.1 Gold mirror thermo-reflectivity

Thin gold or metal layers in general, are known to be thermally excited by near-infrared femtosecond pump-pulses owing to the broad absorption of electron gas (or plasma). This leads to the so-called thermo-reflectance response of metals.¹⁹⁶ The thermal excitation of metals can be described by a two temperature model, dividing the metal's heat capacity into electronic C_e ($66 \text{ J m}^{-3} \text{ K}^{-2}$ for Au)¹⁹⁶ and lattice C_l ($2.43 \cdot 10^6 \text{ J m}^{-3} \text{ K}^{-1}$ for Au)¹⁹⁶ contributions. The temperature of the electron gas T_e is raised by the energy deposited by the pump pulse $E_{pump}(t)$ and coupled to the temperature of the lattice T_l by electron-phonon coupling g_{e-ph} ($2.1 \cdot 10^{16} \text{ J fs}^{-1} \text{ K}^{-1} \text{ m}^{-3}$ for Au)¹⁹⁷. The temporal evolution of the heat transfer is then given by the following coupled differential equations:¹⁷⁶

$$C_e T_e \frac{\partial T_e}{\partial t} = -g_{e-ph}(T_e - T_l) + E_{pump}(t), \quad (47)$$

$$C_l \frac{\partial T_l}{\partial t} = g_{e-ph}(T_e - T_l). \quad (48)$$

The deposited pump energy is given by

$$E_{pump}(t, \lambda) = J_{pulse} \cdot A(\lambda) \cdot S_{pulse}(t)/d \quad \text{with} \quad S_{pulse}(t) = \frac{2\sqrt{\ln 2}}{\sqrt{\pi} \cdot t_p} \exp \left[-4 \cdot \ln \left(\frac{\sqrt{2}t}{t_p} \right)^2 \right], \quad (49)$$

where J_{pulse} is the pump fluence, A is the absorbance, $f_{pulse}(t)$ is the temporal pulse profile, d is the metal thickness and t_p the pulse width. Figure 5.2a shows the time evolution of electron and lattice temperature calculated with equations (19) and (48) for the top gold mirror of the transparent cavity introduced in section 5.2 (30 nm, with $A_{Au} \approx 2.6 \%$) and the pump pulse parameters used for the experiments presented later in section 5.5 ($J_{pulse} = 61 \text{ } \mu\text{J}/\text{cm}^2$, $t_p = 150 \text{ fs}$). The results show that only the electron gas should be considerably heated by the pump pulse ($\Delta T_e \approx 23 \text{ K}$), whereas the lattice temperature increase should be small ($\Delta T_l \approx 0.2 \text{ K}$). Considering the linear thermal expansion coefficient of the neighbouring aluminium oxide layer

(10^{-6} K^{-1}), heating effects should not lead to detectable changes in terms of thermal expansion. Therefore, the following discussion focuses on thermo-reflection.

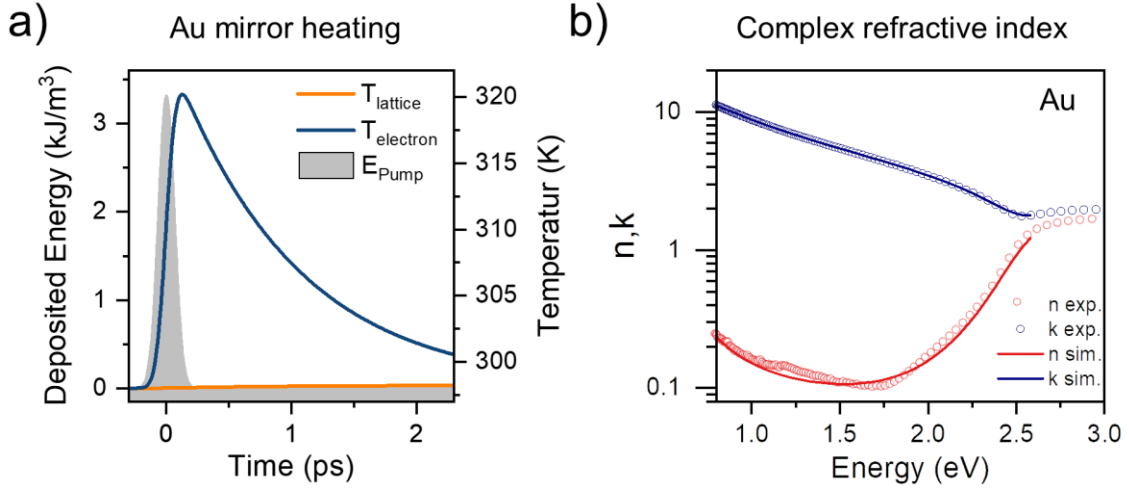


Figure 5.2 a) Calculated, pump-induced change of electron and lattice temperature of a 30 nm gold film excited at 1000 nm. **b)** Complex refractive index of gold calculated with the Lorentz-Drude model (solid lines) and experimental data¹⁹⁸ for comparison (empty circles).

The pump-induced change of electron and lattice temperature introduces a time dependence to the damping rate of electron plasma, which in turn leads to a transient change in the metal dielectric function or refractive index, respectively (see Background, section 2.1.1). The temperature dependence of the electron plasma damping rate can be described by the expression:¹⁹⁷

$$\Gamma_0(T, t) = A_{ee}T_e(t)^2 + B_{eph}T_l(t). \quad (50)$$

The first term accounts for damping by electron-electron scattering and the second term for electron-phonon scattering, with the empirical constants $A_{ee} = 1.7 \cdot 10^7 \text{ s}^{-1} \text{ K}^{-2}$ and $B_{eph} = 1.45 \cdot 10^{11} \text{ s}^{-1} \text{ K}^{-1}$ for Au.¹⁹⁷ Here, the intraband or free electron part of the gold dielectric function is described by the Drude model and higher frequency interband contributions are described by a sum of Lorentz oscillators:¹⁷⁷

$$\varepsilon(\omega) = 1 - \frac{f_0 \omega_p^2}{\omega(\omega - i\Gamma_0)} + \sum_{j=1}^m \frac{f_j \omega_p^2}{(\omega_j^2 - \omega^2) + i\omega\Gamma_j}, \quad (51)$$

where ω_p is the plasma frequency, m is the number of oscillators with frequency ω_j , strength f_j and lifetime Γ_j . The term $f_0 \omega_p^2$ denotes the squared plasma frequency of intraband transitions with oscillator strength f_0 and damping rate Γ_0 , Using the relationship

$$n/k = \left(\frac{1}{2} \left(\sqrt{\text{Re}(\varepsilon(\omega))^2 + \text{Im}(\varepsilon(\omega))^2} \pm \text{Re}(\varepsilon(\omega)) \right) \right)^{-\frac{1}{2}}, \quad (52)$$

the complex refractive index of gold can be calculated with tabulated values¹⁷⁷ for the Lorentz-Drude model of gold. The obtained values agree well with the experimental complex refractive index measured at room temperature¹⁹⁸ (Figure 5.2b). Assuming that interband transitions remain unaffected by the pump pulse heating, which is a reasonable approximation for small heat transfer to the lattice, the time-dependent change of the complex refractive index can be calculated using equations (50) and (51). The results obtained at the energy of the (6,5) SWCNT E₁₁ exciton are shown in Figure 5.3a with the conditions used to calculate the pump-induced heating presented in Figure 5.2a. For these conditions the change in the complex refractive index components n and k is on the order of 2 %. By incorporating the transient change of the gold refractive index into the TM scheme, the cavity transmission can be simulated as a function of time.¹⁷⁶ Time zero is defined as the pump pulse arrival time (maximum of the temporal pulse shape). For a comparison between simulated and the experimental data shown later, the cavity transient difference transmission is plotted as $-\lg(T(t)/T_0)$, where T_0 represents the cavity transmission spectrum calculated for the plasma damping rate at room temperature $\Gamma_0(RT)$. In order to purely assess the thermo-reflectivity contribution, the refractive indices of spacer and SWCNT layer were held constant. For simplicity, the same time-dependent refractive index was used for both metal mirrors, which overestimates the effect as most of the pump-fluence is reflected at the first mirror. The results are shown in Figure 5.3b. The thermo-reflectance of the gold mirrors leads to a transmission increase of the transparent polariton modes, most dominant within the first 3

picoseconds. Also note, that this effect does not affect the polariton mode positions. However, for the sample and excitation conditions used here, the effect is small (maximum at LP ~ 0.001 OD) compared to the transient change caused by the SWCNT bleach calculated for the same excitation conditions (maximum at LP ~ 0.07 OD, see section 5.3.2 for details). As the thermo-reflectivity does not produce additional spectral features or lead to a polariton mode shift, together with its small overall contribution, the effect is neglected in the following sections.

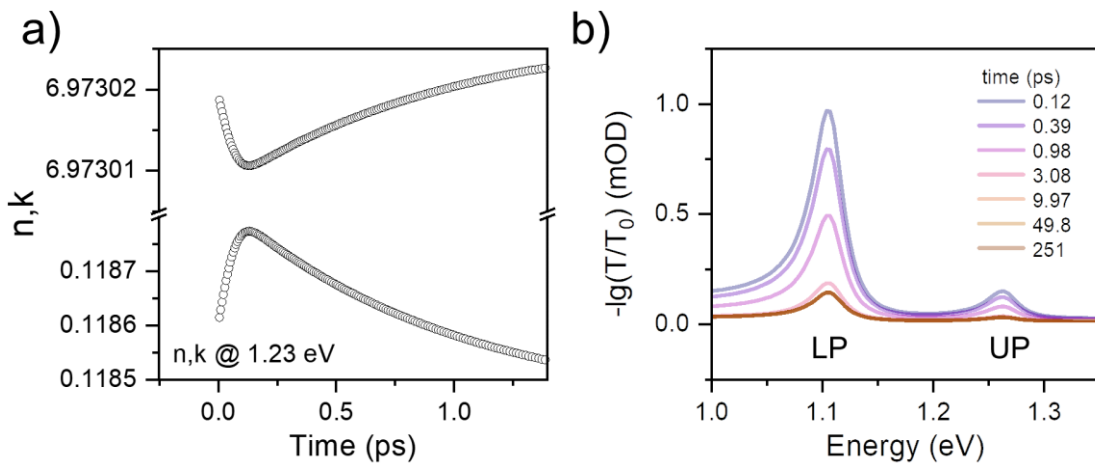


Figure 5.3 a) Calculated, pump-induced change of the metal mirror complex refractive index b) Transient transmission of a strongly coupled SWCNT cavity, simulated for thermally excited metal mirrors. The SWCNT layer excitation was not included for clarity.

5.3.2 Cavity response by SWCNT refractive index change

The predominant contribution to the transient response of strongly coupled cavities, including metalclad and dielectric mirror cavities, is the transient change of the refractive index of the underlying emitter.^{91,92} Note that this is regardless of whether emitter or polaritons are excited.^{91,}

⁹² In order to assess the emitter-contribution to the transient transmission response of the cavity, the cavity transmission is calculated using the complex refractive index extracted from the transient transmission spectrum of the weakly coupled SWCNT reference (Figure 5.4a). A detailed discussion of the SWCNT transient absorption can be found in the Background, section 2.3.2. To account for the reduced pump fluence inside the cavity due to top mirror reflection ($\sim 95\%$ loss at 1000 nm), the reference data was recorded for a 2 nJ pump pulse to later

compare the simulation results with cavity data collected at 30 nJ pulse energy. Further details on the pump-probe measurement can be found in the Experimental, section 3.2.10.

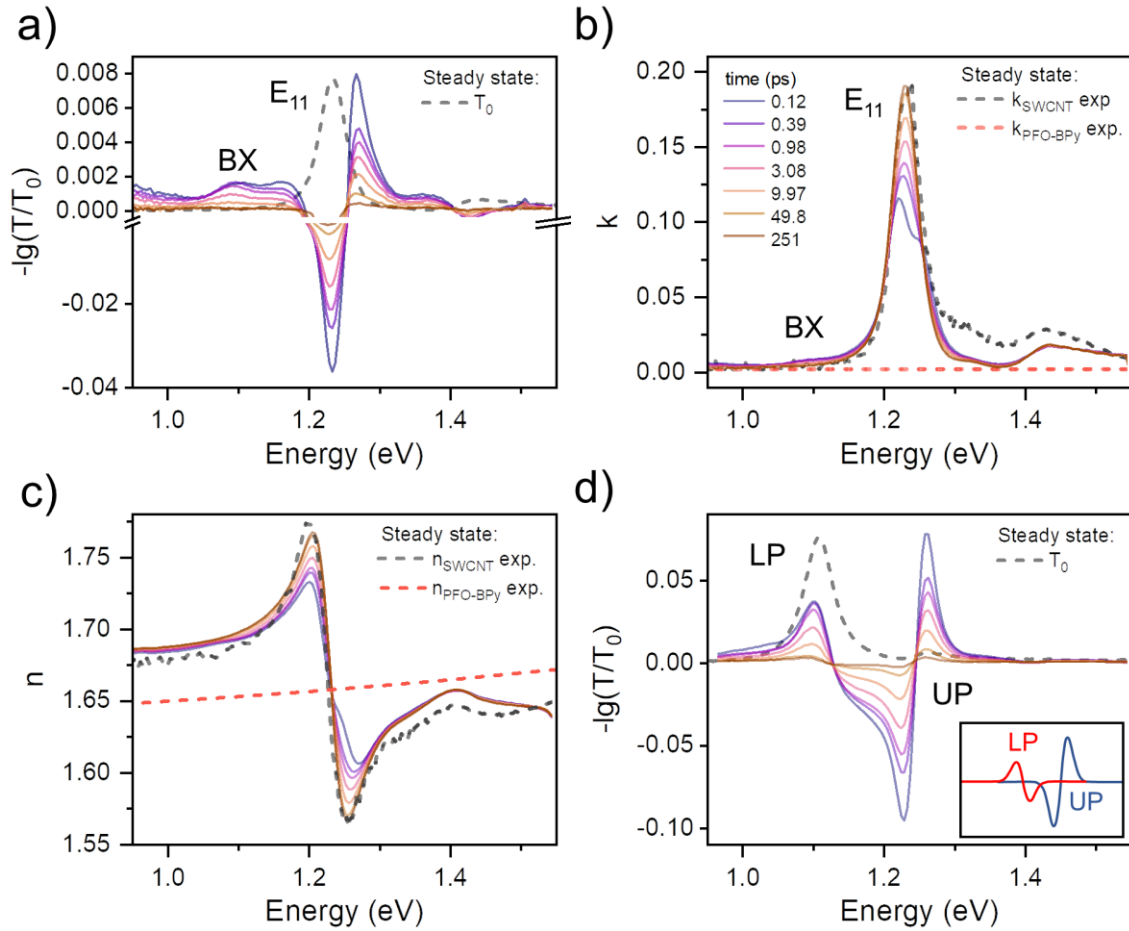


Figure 5.4 **a)** SWCNT transient absorption or transmission, respectively, of the SWCNT reference film. The scaled steady state transmission is shown as a dashed line for comparison. **b)** Imaginary part (k) of the complex refractive index calculated from the SWCNT reference data. **c)** Real part of the complex refractive index (n) calculated by the Kramers-Kronig. Respective imaginary and real part of the complex refractive index for a (6,5) SWCNT/PFO-BPy film (grey dashed line) and a PFO-BPy film (red dashed line) measured by ellipsometry⁴⁰ are given for comparison in (b) and (c). **d)** Simulated cavity transient transmission based on the transient refractive index data shown in (b) and (c). The scaled experimental steady state transmission of the transparent cavity is given for comparison (grey dashed line).

First, the transient transmission $T(t)$ was extracted from the difference spectrum, given as $-lg(T(t)/T_0)$, by adding the steady state transmission T_0 of the SWCNT reference sample:

$$lg(T(t)) = lg(T_0) + lg(T(t)/T_0). \quad (53)$$

Using the approximation that sample reflectivity can be neglected for the reference ($A \approx 1 - T$), the transient transmission can be converted to the imaginary part of the complex refractive index k with

$$k(t) = \frac{lg(A(t)) \cdot \lambda}{lg(e) \cdot 4\pi \cdot d(SWCNT)}, \quad (54)$$

where $d(SWCNT)$ is the average thickness of the SWCNT reference film as obtained by profilometry. The results are shown in Figure 5.4b. For increasing pump-probe delay (approaching steady state), the extracted extinction coefficient approaches values determined experimentally for a (6,5) SWCNT film by Graf *et al.*⁴⁰ (Figure 5.4b, grey dashed line). The real part n was then calculated by the Kramers-Kronig relation for the complex refractive index (see Background, section 2.1.1 for details), again showing good agreement with experiment (Figure 5.4c, grey dashed line). The refractive index components for the matrix polymer PFO-BPy are shown in Figure 5.4 b and c for comparison.

Using the transient refractive index extracted from the SWCNT transient transmission or absorption, respectively, the effect of the SWCNT bleach on the cavity transient transmission spectrum can be calculated using the TM scheme. For simulation, the layer thicknesses were chosen based on the cavity stack introduced in section 5.2. The simulated cavity transient transmission spectrum is shown in Figure 5.4d. In the following, the important emitter-bleach related transient transmission features are discussed. Whereas the weakly coupled SWCNT spectrum (Figure 5.4a) is dominated by the E_{11} bleach (5 times more intense than all other signals), the spectrum of the strongly coupled cavity exhibits two overlapping spectral features with derivative-like lineshapes (see inset Figure 5.4d for illustration). The low energy feature can be attributed to the LP ground state response and the high energy feature to the UP ground state

response. Due to the pump induced bleach of the SWCNT E_{11} exciton absorption, the Rabi-splitting is reduced, and as a consequence, LP and UP are spectrally closest to each other at pump-pulse arrival. Upon ground state recovery, the SWCNT absorption and Rabi splitting recover, leading to increasing LP-UP separation at later times. In the transient difference spectrum, the polariton mode shift produces the characteristic derivative-like line shape.

This is illustrated in Figure 5.5, depicting the simulated cavity transmission without subtraction of the steady state data. The isosbestic points of the LP (1.13 eV) and UP (1.25 eV) feature in the difference spectrum (Figure 5.4d), coincide with isosbestic points in the transmission spectra shown in Figure 5.5a and b. The LP mode is shifted towards lower energies during excitation, leading to an increase in transmission (purple area Figure 5.5a, corresponding to negative signal in Figure 5.4d) above 1.13 eV and a decrease in transmission (orange area Figure 5.5a, corresponding to positive signal in Figure 5.4d) below 1.13 eV. The same process occurs for the UP around 1.25 eV with inverse signs (Figure 5.5b). During relaxation, LP and UP shift back towards their equilibrium positions (Figure 5.5 blue to brown lines), corresponding to a reduction in signal intensity in the difference spectrum (Figure 5.4d).

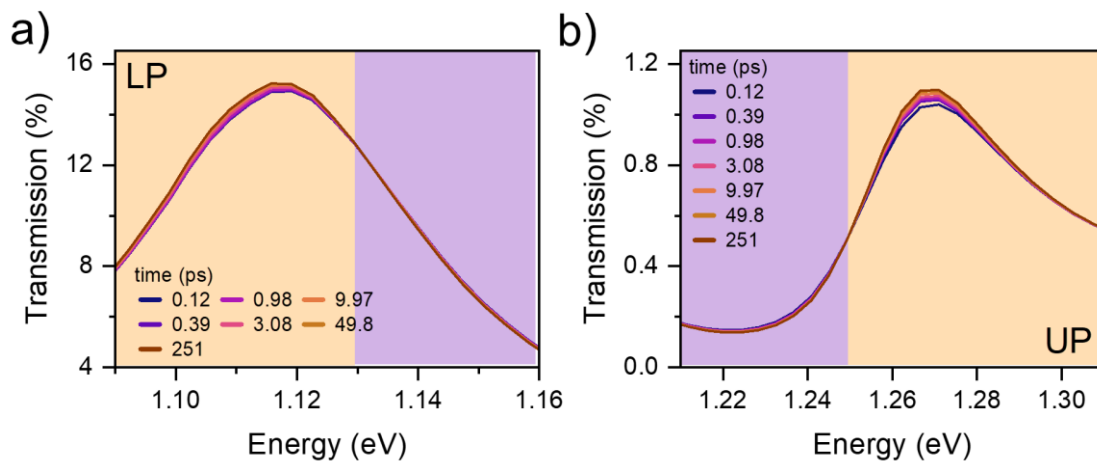


Figure 5.5 Simulated LP (a) and UP (b) mode transmission spectra for increasing pump-probe delay. The data was simulated using the same parameters as used in Figure 5.4d, but without subtraction of the steady state cavity transmission. Increased and decreased transmission is indicated in orange and purple, respectively.

After establishing the non-polaritonic contributions to the cavity transient transmission, the next section proceeds with an approach to fit the TM simulation of the cavity transient transmission to experimental data. This will serve as a tool to identify polariton intrinsic excited state dynamics in real pump-probe experiments.

5.4 Genetic algorithm fit

In order to identify polariton excited state features by comparing experimental transient transmission data with simulation data of only non-polaritonic features, the simulation requires highly accurate input parameters. The input parameters with the highest uncertainty are the structural data for the cavity sample, here that is the different layer thicknesses and the root mean square (RMS) roughness. These parameters can only be estimated by local profilometry measurements (also see Experimental, section 3.3.1), which may not precisely represent the much larger sample area investigated by the pump-probe experiment. This also affects the calculation of the transient refractive index of the emitter, in which it is assumed, that the average thickness of the sample area investigated in the pump-probe measurement equals the average sample thickness measured in steady state transmission (compare section 5.3.2, equations (53) and (54)). This reduces the quantitative agreement between simulated and experimental cavity TA data, as can be seen in previous reports.^{91,92} Here, this limitation is overcome by fitting the TM simulation to the experimental transient transmission data. The problem of fitting cavity data with the TM scheme is, that usually no analytic expression for the target spectrum exists. For example, the polariton modes can only be described analytically close to zero detuning.⁷⁵ Hence, conventional regression methods cannot be employed. This is why a commercial genetic algorithm (GA)¹⁷⁵ is chosen to fit the data.

Figure 5.6a shows a schematic of the GA-TM fitting routine. The GA is used to stochastically create combinations of input parameters. The possible input parameter values have to be given as vectors,¹⁷⁵ with the smallest entry being the lower bound and the largest entry being the upper bound of the parameter. As changing the SWCNT layer thickness affects the imaginary part of

the refractive index (see equation (54)), the refractive index is recalculated with the new value. The input (parameter or SWCNT transient refractive index) is then transferred to the TM scheme and a difference transmission spectrum is calculated. The resulting spectrum is compared to the experimental target spectrum (fitness function). This is done for a set of different input parameter combinations (population). After each iteration (generation), successful combinations (selection) are changed (mutated) or combined (crossover) minimizing the difference to the target function (increasing the fitness of the population). The optimization is terminated if the fitness is not improved over the number of stall generations. Here, the standard settings of the commercial GA were employed (Table 5.1). It is important to note, that in contrast to a conventional regression method, the best fit value is limited by the coarseness of the parameter values. As the GA randomly tests the parameter space, the final result may also slightly differ for each run.¹⁷⁵

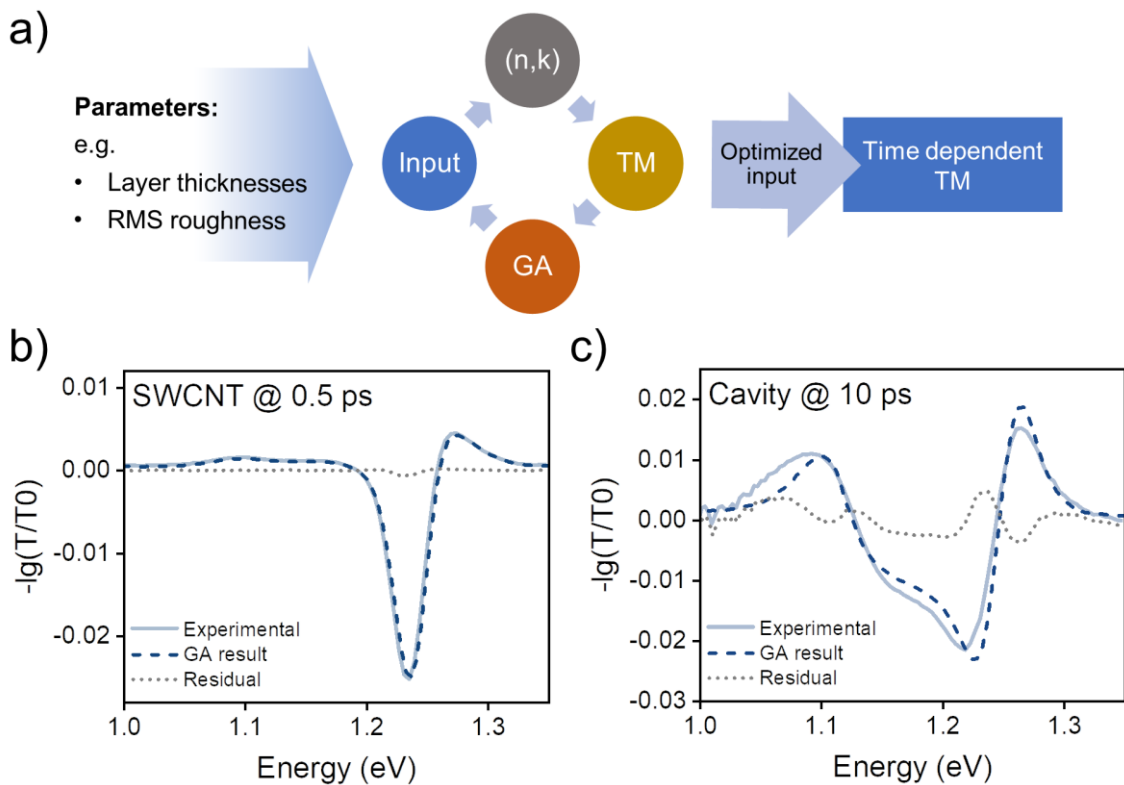


Figure 5.6 **a)** Schematic illustration of the GA-TM fitting routine. **b)** GA-TM simulation of the SWCNT TA spectrum from the transient refractive index data of the same film. **c)** GA-TM simulation of the cavity transient transmission spectrum under UP excitation. The GA results for the input parameters are shown in Table 5.2.

Table 5.1 Genetic Algorithm settings.

Parameter	Population size	Generations	Crossover fraction	Stall generations
Value	200	100	0.5	40

The approach is demonstrated by simulating the transient spectrum of the reference SWCNT film using at 0.5 ps pump-probe delay (Figure 5.6b). The GA chose a SWCNT film thickness of 40.3 nm, that lies within the thickness uncertainty estimated by profilometry (30 ± 15) nm. Note, that for calculating the transient spectrum without GA optimization, that is for 30 nm film thickness, the residual between simulated and experimental data was significantly higher, due to the uncertainties of the structural input parameter.

For the cavity simulation two further parameters were added. To account for the wavelength dependence of the SWCNT excitation, a scaling parameter was added to scale the transient spectrum calculated in equation (53) with regard to the film absorption. This bleaching parameter serves as handle to adjust for variations in the bleach intensity for a given SWCNT layer thickness. To reduce computation time, a global scaling parameter was introduced. For this, the parameter was chosen to scale the result by 5 orders of magnitude. In the initial optimization phase, only combinations with a scaling parameter close to one have a good chance of survival, as combinations with a large global scaling parameter will not improve much upon change of the physical parameters. Close to the end of the optimization, the global scaling parameter enhances the probability for the population entering the stall generation phase, slightly improving parameter combinations with lower fitness. Note however, that this reduces the physical accuracy of the resulting parameter values. Figure 5.6c shows the simulated and experimental cavity transient transmission data. Experimental data for a 10 ps pump-probe delay was used as the target spectrum. At this late time, the experimental spectra should be governed by the recovery of the SWCNT bleach and polariton intrinsic contributions should be low. Note that at even later times, the polariton intrinsic contributions should be even lower, however, the signal to noise ratios at spectral areas of low transmission was considerably higher, making the fit less precise. For

parameter bounds well beyond the experimental uncertainty of the respective parameter, the algorithm converged at values close to the experimental values (Table 5.2).

Table 5.2 Summary of GA results for the simulation of the TT cavity data for UP excitation at 10 ps pump-probe delay.

Parameter	SWCNT thickness (nm)	Spacer thickness (nm)	Mirror thickness (nm)	RMS roughness (nm)	Bleach scaling parameter	Global scaling parameter
Lower bound	15	145	20	1	0.01	0.01
Upper bound	55	95	35	200	100	100
Interval	0.5	0.5	0.5	1	0.01	0.01
GA Result	46	116	28.5	22	1.53	0.95
Experimental	30 ± 15	125 ± 2	$30 \pm 1^*$	10	1.41^\dagger	

*From internal evaporator calibration, †From E11 to E22 absorption ratio.

The uncertainty of the SWCNT layer thickness corresponds to the variation found for the SWCNT reference film shown in section 5.2 and was calculated from three height measurements at sample positions spaced over a distance of 1 cm. The RMS roughness was determined for the same film from a $5 \times 5 \mu\text{m}$ atomic force micrograph. All profilometry data were obtained from atomic force micrographs (see Experimental, section 3.3.1). The mirror layer thickness (asterisk) was estimated from the internal calibration of the thermal evaporator with a uniformity of $\pm 3\%$. The higher deviation of the RMS roughness compared to the other structural parameters may be caused by the fact, that intralayer scattering was not included into the TM simulation and the RMS roughness is a handle to compensate for this fact, as both RMS roughness and intralayer scattering lead to line broadening of the cavity mode. Also note that the RMS roughness was included as a global parameter (see Background, section 2.1.2). The bleach scaling parameter equals approximately the ratio between the E₁₁ and E₂₂ peaks in absorption (Table 5.2, dagger), which agrees with the notion, that the cavity was excited closer to the E₁₁ transition. The global scaling

parameter only deviates 5 % from unity, indicating that the overall experimental spectrum is approximated well by refining the structural input parameters.

5.5 Polariton transient transmission

In section 5.3, non-polaritonic origins of the cavity transient transmission were discussed and the pump-induced change of the SWCNT refractive index was identified as the major contribution, leading to characteristic derivative-like features of the LP and UP. In section 5.4, a method was introduced to match the non-polaritonic simulated transient cavity response to experimental data in order to identify polariton excited state features, which are not included in the simulated data. Based on these considerations, the experimental data on the strongly coupled (6,5) SWCNT cavities can be analysed and discussed.

The transparent cavity sample (introduced in section 5.1) was excited with 30 nJ ($\sim 61 \mu\text{J}/\text{cm}^2$) pump pulses at the E_{22} (2.16 eV) and the UP (1.27 eV) energy (see Experimental, section 3.2.10 for details). The supercontinuum probe beam was linearly polarized at the magic angle (54.7°) relative to the pump polarization. Note that under normal incidence, the p - and s -cavity modes are degenerate (see Background, section 2.1.3). The input parameters for the simulation were adjusted by a fit to the experimental cavity difference spectrum under UP excitation at 10 ps pump-probe delay.

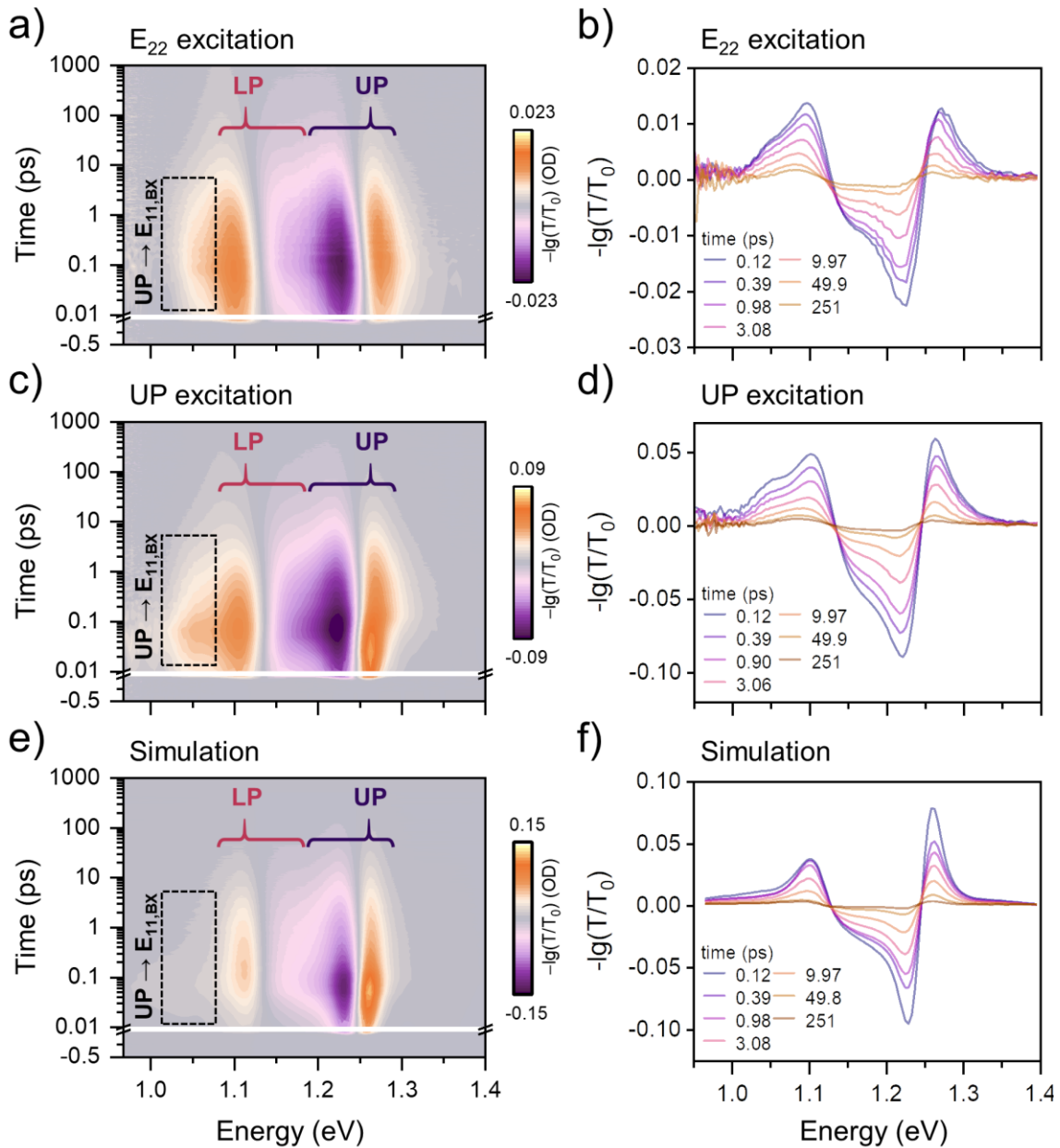


Figure 5.7 **a)** and **b)** Transient transmission (TT) data for off-resonant E_{22} excitation of a strongly coupled SWCNT cavity. **c)** and **d)** TT data of the same cavity resonantly excited at the UP mode. **e)** and **f)** Simulated TT data based on the transient refractive index extracted from the SWCNT reference film. LP (red) and UP (dark purple) ground state responses are indicated with the bracket tip pointing at the isosbestic point. The proposed UP to biexciton transition ($UP \rightarrow E_{11,BX}$) is indicated by a dashed square.

Figure 5.7a and b depict the experimental TT data for off-resonant E_{22} excitation as contour plot (a) and as spectra for selected delay times (b). LP ground state response occurs in the region

centered around 1.13 eV and UP ground state response is centered around 1.25 eV. These features are reproduced by the simulation (Figure 5.7e and f) and can be attributed to the SWCNT bleach as discussed in section 5.3.2. The LP response appears broadened owing to a shoulder at its red flank. This shoulder is absent in the simulation data (compare Figure 5.7e and f). Its spectral position at 1.05 approximately equals the separation between the UP and E_{11} biexciton (BX) of the (6,5) SWCNTs⁵³, which suggests a direct UP to biexciton transition. To confirm this assignment, the cavity transient transmission was recorded for resonant UP excitation. The corresponding data is shown in Figure 5.7c and d. Under these conditions, the same red-shifted shoulder appears immediately, that is, within the HWHM of the pump-pulse width (~ 75 fs), and with increased intensity. In contrast to off-resonant E_{22} excitation, the UP is directly populated, which agrees well with a direct UP to biexciton transition.

In order to further validate, that the observed feature at 1.05 eV arises from photo-induced absorption, the simulated data is superimposed onto the experimental for UP excitation for closer comparison (Figure 5.8). In Figure 5.8a, the largest deviation between simulation and experiment is found for early pump-probe delays ($\Delta t < 1$ ps). These differences may arise from the more prominent role of equilibration between UP, LP and exciton reservoir, as was observed previously with two-dimensional Fourier transform spectroscopy.¹⁸⁶ Another potential cause for mismatch are coherent interactions between pump- and probe-pulse ($\Delta t < 0.5$ ps), which are not included in the TM simulation. Apart from the aforementioned deviation, the experimental data exhibits slightly broader lineshapes than the simulation, most likely because the interface roughness was modelled by a global scalar scattering parameter (see Background, section 2.1.2) and scattering within the layers was neglected. At later times ($\Delta t > 1$ ps), the simulation and experimental data agree well (Figure 5.8a), apart from the red-shifted shoulder identified as the UP to biexciton transition. The origin of this shoulder cannot be explained by a transient change of transmission, as it is lower in energy than the equilibrium position of the LP polariton (Figure 5.8b) and therefore can be attributed to photo-induced absorption with certainty.

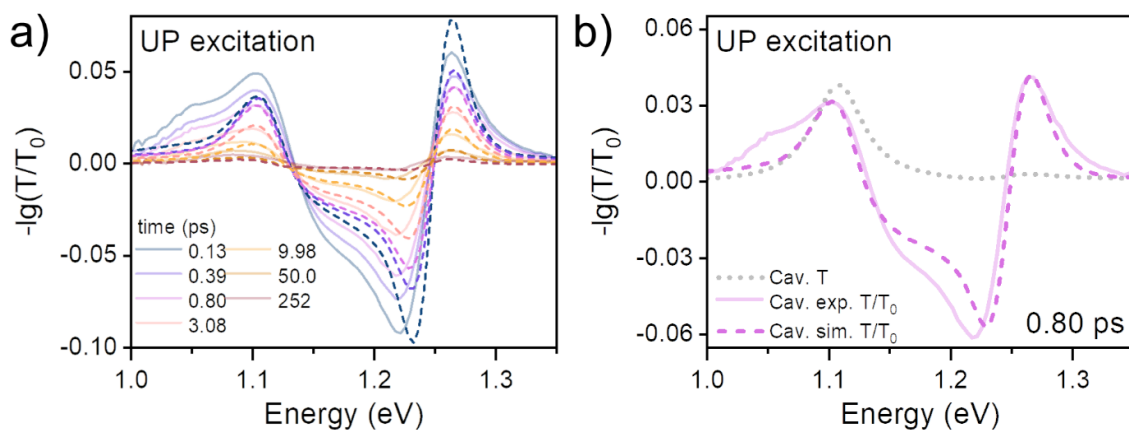


Figure 5.8 a) Superposition of experimental (solid lines) and simulated (dashed lines) transient transmission data for UP excitation. **b)** Experimental (solid lines) and simulated (dashed lines) transient spectra shown in (a) at 0.8 ps pump-probe delay. The steady state cavity transmission is given for comparison (grey dotted line).

5.6 Decay associated difference spectra (DADS)

In order to further analyse the dynamics of the experimental and simulated transient data presented in the previous section, global analysis is employed. This analysis method allows to fit transient spectra without assuming a detailed kinetic or spectral model by a sum of exponentials with wavelength dependent amplitudes. Owing to the wavelength dependent amplitudes, the data is fitted over the whole spectral range simultaneously, also referred to as globally. Commonly, the number of exponentials is chosen to equal the number of spectrally different components, such as different electronic states or molecular species. The spectral amplitudes of the different exponentials are called decay associated difference spectra (DADS).¹⁹⁹ Fitting the three datasets presented in section 5.5 with minimum error and residual required five exponentials and one offset for measurement noise. The DADS are shown in Figure 5.9 and the time constants of the exponentials are given in Table 5.3.

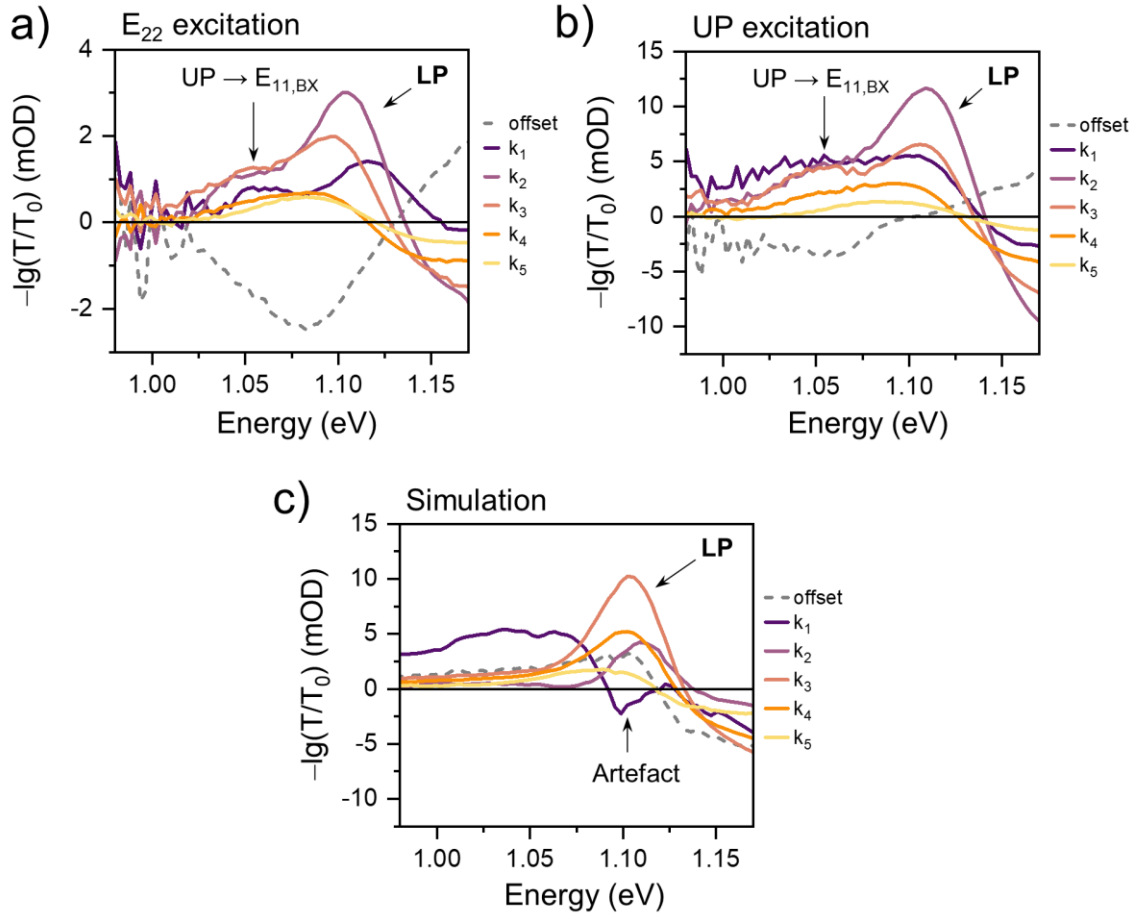


Figure 5.9 Spectral region of the biexciton absorption feature in decay associated difference spectra. a) Cavity excited off-resonantly at E_{22} . b) Cavity excited resonantly at the UP mode. c) Corresponding TM simulation. The lifetimes calculated from the extracted time constants ($k_1 - k_5$) can be found in Table 5.3.

The UP to biexciton transition ($UP \rightarrow E_{11,BX}$) can be seen around 1.05 eV in the DADS of the experimental data, for both E_{22} and UP excitation (Figure 5.9a and b). The feature is most clearly visible in the second and third decay components (k_2 and k_3). Global analysis reveals, that the first three decays are about twice as fast for UP excitation than for E_{22} excitation (Table 5.3). The slower decay in case of E_{22} excitation can be attributed to the required delay for UP population, including internal relaxation to the E_{11} state (~ 100 fs)¹¹⁰ and subsequent population transfer from exciton reservoir to the UP state. Furthermore, the DADS reveal, that the evolution of the UP to biexciton transition approximately follows the evolution of the LP feature (around 1.1 eV, Figure 5.9a and b). As demonstrated in section 5.3.2, the LP feature is produced by the SWCNT ground

state bleach. Therefore, the similar spectral evolutions of LP signal and UP to biexciton signal indicate, that the polariton-mediated biexciton transition follows the evolution of the ground state bleach. This notion agrees with previous experiments on weakly coupled (6,5) SWCNTs, in which the biexciton population was found to follow the exciton population.⁵³ It further corroborates the biexciton character of the observed transition at 1.05 eV.

Table 5.3 Summary of lifetimes ($1/k$) obtained by global analysis.

Lifetime component	$1/k_1$ (ps)	$1/k_2$ (ps)	$1/k_3$ (ps)	$1/k_4$ (ps)	$1/k_5$ (ps)
E_{22} excitation	0.53 ± 0.06	2.0 ± 0.2	10 ± 1	47 ± 6	380 ± 40
UP excitation	0.20 ± 0.02	1.15 ± 0.05	5.3 ± 0.2	38 ± 2	543 ± 40
Simulation	0.127 ± 0.003	0.78 ± 0.03	4.06 ± 0.06	20.9 ± 0.2	328 ± 3

Global analysis of the simulated data, shown in Figure 5.9c, gives additional evidence for the polariton intrinsic nature of the UP to biexciton transition. As the simulated data does not contain any polariton intrinsic features, the DADS in Figure 5.9c do not exhibit a red shoulder at 1.05 eV. In case of the global analysis of the simulated data, it is however important to note that the TM simulation does not include coherent interaction between pump- and probe-pulse. This affects the early time delays ($\Delta t < 0.5$ ps) and consequently the first decay k_1 must be considered with caution. For example, the negative feature at the LP position (~ 1.1 eV, Figure 5.9c) is obviously an artefact, as a negative signal at the red-flank of the LP is unphysical (compare experimental data in Figure 5.7a-d). However, later times are not affected and slower components ($k_2 - k_5$, Figure 5.9c) can be interpreted safely, which is done in the following.

Similar to previous reports^{91, 92}, the lifetimes calculated from the k_2 to k_5 components of the simulated data approximately resemble the lifetimes extracted from global analysis of the UP excitation data (Table 5.3). As mentioned earlier, the dynamics of the simulated data arise directly from SWCNT bleach in the weak-coupling regime. Hence, the timescale covered by k_2 to k_5 is

dominated by the emitter dynamics with regard to the polariton ground state response (compare LP feature in Figure 5.9). However, the decay components of the simulated data are consistently faster than the decays obtained from experimental data. This suggests, that population exchange between dark states or the exciton reservoir, respectively, and bright polaritons is efficient enough to slightly delay the overall decay of the polaritons compared to the weakly coupled emitter. This hypothesis is taken up in the next section for the interpretation of the UP to biexciton kinetics.

5.7 Polariton mediated biexciton transition

In the previous sections, it was shown that strongly coupled SWCNT exhibit a UP to biexciton transition in their cavity transient transmission spectra. This transition constitutes a polariton excited state transient feature beyond the polariton intrinsic lifetime. In the following, the kinetics and efficiency of the polariton mediated biexciton transition are compared to the exciton to biexciton transition in weakly coupled SWCNT.

Figure 5.10a presents the proposed transitions and states based on the discussion in sections 5.5 and 5.6. In the weak-coupling regime, the SWCNT E_{22} state is excited by the pump-pulse (brown), fast internal relaxation (100 fs) populates the E_{11} state and the probe-pulse excites excitons into the biexciton state (BX). In the strong coupling regime under off-resonant excitation, excitations relax from the weakly coupled E_{22} state to the exciton reservoir or dark states (DS) of the strongly coupled E_{11} state. From there, population is transferred to the UP and excited by the probe-pulse to the biexciton (pink). For resonant UP excitation, biexcitons are created immediately at probe-pulse arrival. LP and ground state (GS) are shown for comparison (blue). Figure 5.10b shows the respective normalized time-traces. The data for weakly coupled SWCNTs was taken from the transient data of the SWCNT reference film at the exciton to biexciton transition (section 5.3.2) and the corresponding data for strongly coupled SWCNTs was taken from the cavity transient data at the UP to biexciton transition (section 5.5). For resonant UP excitation, the maximum biexciton population is reached at around 60 fs (Figure 5.10b, blue curve). This time corresponds to full absorption of the probe-pulse (HWHM \sim 75 fs) and is in agreement with a direct UP to

biexciton transition as proposed in the kinetic schematic (Figure 5.10a). For off-resonant E_{22} excitation, the biexciton population reaches its maximum at around 130 fs (Figure 5.10b, pink curve). The delay between resonant and off-resonant excitation can be attributed to internal relaxation and population of the UP. For UP excitation, the biexciton exhibits an ultrafast decay within the first 150 fs, whereas this decay is absent for off-resonant E_{22} excitation.

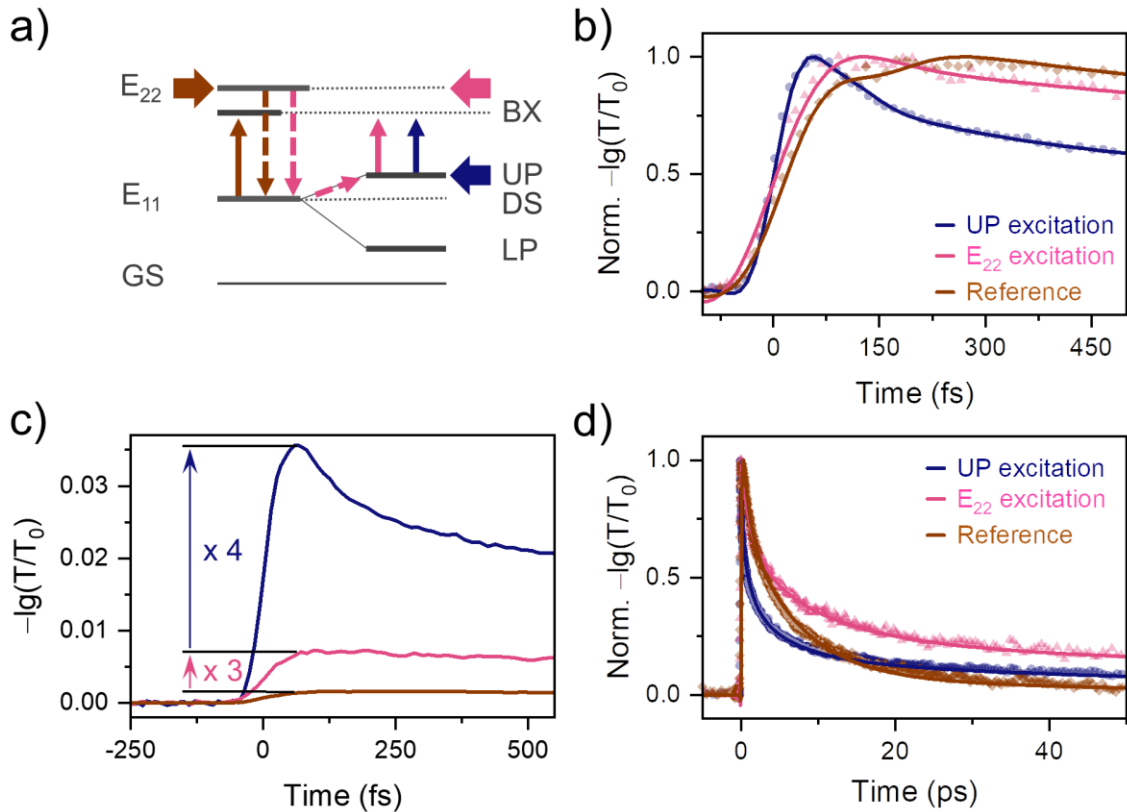


Figure 5.10 **a)** Kinetic schematic for polariton mediated biexciton transition. **b)** Normalized time-traces of the biexciton absorption of strongly coupled SWCNT by resonant (UP, blue) and off-resonant excitation (E_{22} , pink) in comparison to the biexciton absorption in weakly coupled SWCNT (brown). The global analysis fits are given as solid lines. **c)** Absolute difference transient signal of the data shown in (b) and (c). **d)** Extended time window for the data shown in (b).

The ultrafast decay can be associated with polariton population directly injected into the UP, from which the biexciton is populated efficiently at early times. However, after 150 fs, considerable UP population is lost owing to efficient relaxation into the dark states as inferred from PL measurements (see Figure 5.1b). The observed timescale of 150 fs corresponds well with the

polariton lifetime during the coherent energy exchange between UP, LP and dark states.¹⁸⁶ Afterwards, the UP to biexciton feature evolves similar to off-resonant E_{22} excitation, yet, with a higher absolute biexciton population (Figure 5.10c).

Comparing the polariton-mediated biexciton transition to the biexciton transition in weakly coupled SWCNTs in Figure 5.10b, shows, that the maximum biexciton population is delayed by about 40 fs for the weakly coupled reference. This further underlines the efficiency of the dark state to UP coupling, considering that in both cases the excitations have to undergo internal relaxation from the E_{22} to the E_{11} state. Comparing the absolute signal intensities between cavity and reference sample for off-resonant E_{22} excitation (Figure 5.10c), the biexciton transition can be estimated to be three times more efficient than in the weak coupling regime. The comparison of the absolute signal intensities further reveals, that by bypassing the dark states under resonant UP excitation, the biexciton transition can be increased up to 4-fold.

Lastly, it should be noted that the situation on the picosecond-timescale is quite different: Whereas the rise and decay time on the femtosecond-timescale are faster for the UP to biexciton feature than for the corresponding transition in the weak-coupling regime, at later times, the biexciton population of the cavity samples decays slower than for the reference (Figure 5.10d). A similar observation was made in section 5.6. In the global analysis of experimental and simulated cavity transmission spectra, the decay components for the simulation based on the weakly coupled emitter were consistently faster than those obtained from the experimental data. It seems therefore likely, that the dark states are not merely a sink for excitations, as it appears at the femtosecond-timescale, in which they drain population from the short-lived bright states, but that these states have slightly longer lifetimes than the excited emitter states, as can be seen in Figure 5.10d. This is also in line with the cavity fluorescence lifetimes presented in the previous chapter, which were slightly longer compared to the reference decays.

5.8 Summary and Conclusion

In this chapter, the ultrafast dynamics of SWCNT exciton-polaritons were presented based on transient transmission measurements of metal-clad cavities. By simulating the non-polaritonic transient response of the cavities a direct UP to biexciton transition could be identified. Polariton to biexciton transitions are known for quantum-well exciton-polaritons at cryogenic temperatures,^{193, 194} under the condition, that the exciton binding energy exceeds the cavity normal-mode splitting.¹⁹³ The large biexciton binding energy in (6,5) SWCNT of 130 meV⁵³ allowed to observe such a transition for the first time at room temperature and for a cavity sample with a Rabi splitting of 80 meV. The polariton-mediated biexciton transition was found to be three times more efficient than the biexciton transition in a weakly coupled reference. The polariton intrinsic nature of the transition allowed for the demonstration of efficient dark state to UP coupling, as the UP to biexciton transition is even observed under off-resonant E_{22} excitation. At the picosecond-timescale, the slow decay of the UP to biexciton feature compared to the weakly coupled reference further confirmed the dark state nature of the exciton reservoir. By bypassing the dark state dynamics under resonant UP excitation, the biexciton transition could be additionally increased by 4-fold compared to off-resonant excitation. The prospect of enhanced biexciton formation in strongly coupled SWCNTs, might make them an ideal candidate to study correlated many-body states, that are predicted for excitonic molecules in strongly coupled, high quality cavities.²⁰⁰

6 Spectroscopic photodetectors based on SWCNT exciton-polaritons

Strong light-matter coupling changes profoundly the optical properties of the hybridized material component, which may be exploited to improve device performance or add new functionalities to existing optoelectronic devices. In this chapter, the manipulation of the absorption edge of semiconducting SWCNTs by strong light-matter coupling to create tuneable, wavelength-sensitive photodetectors is presented. By using two metal electrodes in a planar organic photodiode structure, a near-infrared (NIR) cavity photon mode is created, that is hybridized with the (6,5) SWCNT E_{11} exciton. The resulting lower polariton band leads to an additional, red-shifted peak in the external quantum efficiency (EQE) of the photodiode, indicating polariton-mediated modification of the SWCNT absorption edge. The photodetector concept is applied to hybrid-organic PC₇₀BM/SWCNT/P3HT bulk and flat heterojunctions (BHJ and FHJ). By tuning the heterojunction thickness, the photodiode operates at application relevant wavelengths up to 1300 nm, far beyond the E_{11} absorption.

Parts of this chapter were published in Mischock *et al.*, J. Chem. Phys. **153**, 201104 (2020).²⁷ Modified reprints are presented with permission of AIP Publishing. This work was carried out in collaboration with Andreas Mischock.

6.1 Introduction

Over the last two decades, donor(D)–acceptor(A) composites of organic materials have proven to be a promising approach for converting light into electrical current, with DA-based organic solar cells (OSCs) achieving around 17% efficiency²⁰¹ and organic photodiodes (OPDs) reaching nanosecond response times²⁰². For both device classes, research efforts aim to increase the NIR sensitivity, by synthesizing absorber materials with small optical gaps¹⁵⁹. For solar cells, this is

motivated by the Shockley-Queisser limit, which predicts a maximum power-conversion efficiency between 1000 and 1500 nm for single-junction solar cells.²⁰³ For photodetectors, the NIR is relevant for various applications in optical communication, environmental monitoring, biomedical imaging and sensing.¹⁵⁸ Although in both device classes inorganic materials generally surpass organic materials in lifetime and performance, OSCs and OPDs may excel in terms of manufacturing cost¹⁶¹, mechanical flexibility¹⁵⁸ or operating temperature²⁰⁴, making them commercially interesting.

Most organic donor–acceptor (D:A) blends of small bandgap compounds typically possess a rather broad NIR absorption,²⁰⁵ which is problematic for OSC and OPD devices. For OSC devices, this leads to large Urbach energies and a consequently reduced power-conversion compared to inorganic NIR absorbers (see Background, section 2.4 for details).^{26, 164} For OPDs, tuneable narrowband absorption is of interest.²⁰⁶ Narrow band low-dimensional materials such as monochiral SWCNTs²⁰⁷ or two-dimensional transition metal dichalcogenides (TMDs)²⁰⁸ can be used instead of organic materials, as they exhibit a steep absorption edge, however, the absorption is fixed to the employed material e.g. a certain nanotube chirality.²⁰⁷ Alternatively cavities can be used to modify the absorption of broadband organic absorbers to yield tuneable narrowband absorption¹⁶⁹, however, the tunability is usually limited by the spectral width of the underlying charge-transfer state.²⁰⁹ Strong coupling of cavity integrated OSCs and OPDs to narrow-band absorbers is a recent approach, to lift the aforementioned limitations. In strongly coupled OSCs, the lower polariton (LP) defines the new absorption edge of the device, exhibiting significantly lower Urbach energies than the underlying emitter.²⁶ Furthermore, in strongly coupled devices, LP absorption depends on its exciton fraction²⁵ and therefore the tunability is not limited by the absorption of a charge-transfer state, as is the case for OPDs based on weakly coupled cavities.²⁰⁹ A promising platform for light-harvesting in the strong coupling regime are SWCNT-based photodiodes^{167, 210-212}, because SWCNTs provide room-temperature stable, low energy excitons

with high oscillator strength and their lower polariton branch can be tuned into the telecom-relevant NIR.⁴⁰

In the following, the concept of strongly coupled SWCNT photodetectors is demonstrated for photodiodes based on organic bulk and flat PC₇₀BM:SWCNT:P3HT heterojunctions. The light-matter coupling of the photodiode active layer is characterized by angle-resolved reflectivity measurements and evaluated by the coupled oscillator (CO) model. The device performance is assessed in terms of EQE and diode behavior.

6.2 Photodiode and heterojunction design

Photocurrent generation from polaritons is believed to occur by dissociation of their exciton-component,²⁵ and hence for conventional OPDs, the heterojunction must be designed to dissociate the underlying exciton. Here, that is the (6,5) SWCNT E₁₁ exciton. The ambipolar nature of SWCNTs allows for two coupled type II heterojunctions, one for hole and one for electron extraction. The molecular structures of the heterojunction materials are given in Figure 6.1a together with the respective energy level diagram in Figure 6.1c. For hole extraction, a P3HT-donor/SWCNT-acceptor junction was employed. The advantage of P3HT (poly[3-hexylthiophene-2,5-diyl]) is its ability to wrap SWCNTs,²¹³ which enables polymer exchange of the insulating PFO-BPy, that is used to select the (6,5) chirality (Experimental, section 3.1.2). Here, regio-regular P3HT (rr-P3HT) was employed. Figure 6.1b shows the absorption spectra of a film of PFO-BPy wrapped and P3HT wrapped SWCNTs. For both films, free, residual wrapping polymer forms a matrix for the SWCNTs. The E₁₁ absorption is red-shifted from 998 nm (PFO-BPy) to 1020 nm (P3HT) indicating successful substitution, accompanied by a linewidth increase of about 10 nm. For electron extraction, a SWCNT-donor/PC₇₀BM-acceptor junction was formed by adding PC₇₀BM (3'-Phenyl-3'H-cyclopropa[8,25]-[5,6]fullerene-C70-D5h(6)-3'-methyl butanoate) to the SWCNT-P3HT dispersion.

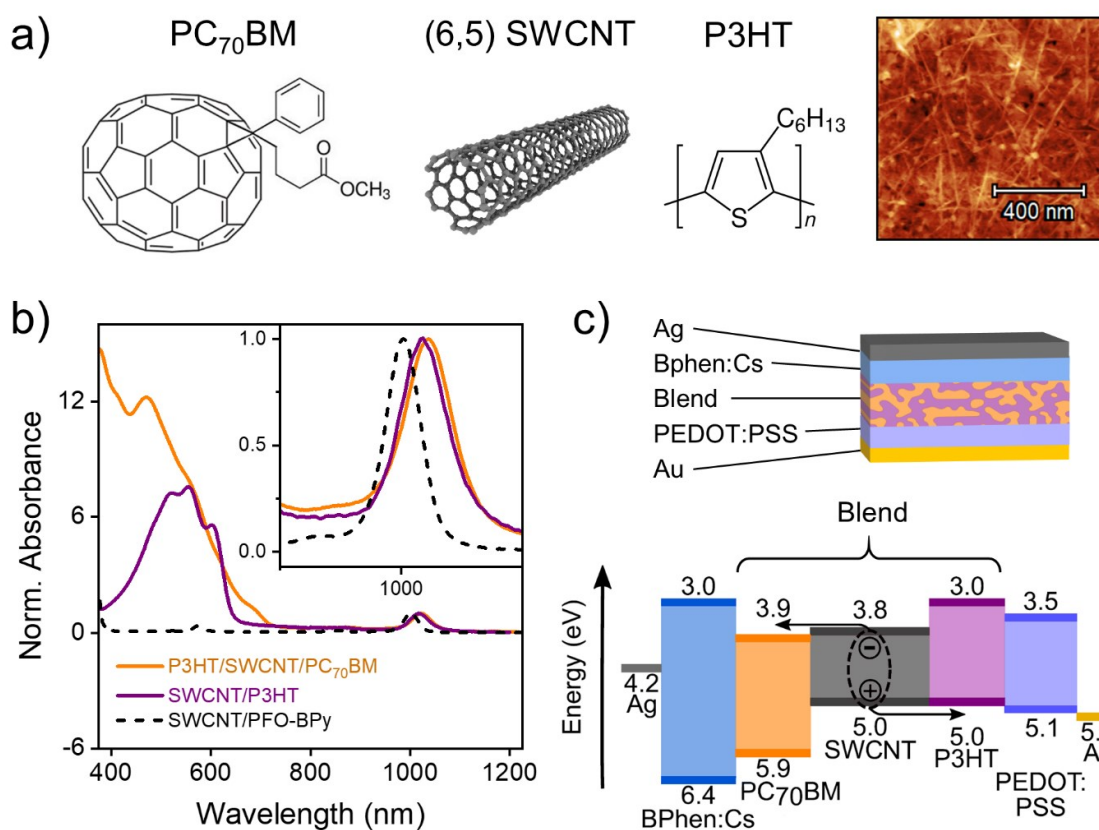


Figure 6.1 a) Molecular structures of the heterojunction materials PC₇₀BM, SWCNT and rr-P3HT and AFM micrograph of the blend film. b) Film absorbance spectra for PFO-BPy wrapped (6,5) SWCNTs (black dashed line), P3HT wrapped SWCNTs (purple solid line) and P3HT wrapped SWCNTs in a P3HT/PC₇₀BM blend (purple solid line) normalized to the E₁₁ transition. The inset shows the spectral area around the E₁₁ exciton resonance. c) Molecular energy levels and device stack of the employed p-i-n diode: Polaritons are resonantly excited by near infrared (NIR) illumination on the SWNTs, and their excitonic component is dissociated at either the SWCNT/PC₇₀BM or SWCNT/P3HT interface. PEDOT:PSS and BPhen:Cs layers serve as hole transport and electron transport material, respectively.

For organic DA heterojunctions the film morphology is crucial. P3HT/PC₆₀BM show a uniform phase separation for 50:50 mixtures, which is optimal for device performance, due to a large DA interface for charge separation and sufficiently large donor and acceptor percolation paths for charge extraction.²¹⁴ Here, the film morphology for PC₇₀BM:SWCNT:P3HT blends was found to be optimal for a 3:4 P3HT:PC₇₀BM composition with 1.4 wt% SWCNT in chlorobenzene. AFM micrographs show moderate PC₇₀BM-aggregation (circular structures with 20-40 nm diameter)

with SWCNTs penetrating the entire film (Figure 6.1a). This composition also provides smooth and homogeneous films, whereas higher SWCNT concentrations (5 wt%) yielded rougher films compromising the cavity quality (for a detailed description see Experimental, section 3.1.2). For the full blend, the E_{11} absorption is only slightly shifted (1022 nm) upon addition of PC₇₀BM, whereas the linewidth remains unchanged compared to the SWCNT:P3HT film (Figure 6.1b). Lastly, P3HT and PC₇₀BM exhibit only weak absorption around 1000 nm, i.e. the E_{11} transition, which is beneficial for strong light-matter coupling to the SWCNT exciton.

Evaporated layers of gold (Au) and silver (Ag) were used as anode and cathode, respectively. The electrodes also function as cavity mirrors for the photodiode, forming a so-called strong cavity. For the reference diodes, the Ag mirror was replaced by transparent indium tin oxide (ITO), forming a so-called weak cavity. To improve energy level alignment with electrodes and mirrors, poly(3,4-ethylenedioxythiophene) polystyrene sulfonate (PEDOT:PSS) was used as hole transport layer and cesium (Cs) doped bathophenanthroline (BPhen:Cs) as electron transport layer (Figure 6.1c). A detailed description of the device fabrication can be found in Experimental, section 3.1.4. The resulting photodetector can be considered to be a p-i-n diode with the ambipolar SWCNT representing the intrinsic layer (i).

6.3 Strongly coupled heterojunctions

In this section, the light-matter coupling of the strong cavity diode is compared to the weak cavity reference diode. The cavity tuning is given by the distance between the electrodes or mirrors, respectively, which is controlled by the thickness of the heterojunction layer, while the hole transport layer (HTL) and electron transport layer (ETL) are kept constant. To assess the light-matter coupling of the SWCNTs within the bulk heterojunction formed by the PC₇₀BM/SWCNT/P3HT blend, angle-resolved reflectivity spectra of the photodetectors were recorded.

Figure 6.2a shows the reflectivity data collected for a weak cavity. The cavity is formed by a 100 nm Ag and a 90 nm ITO electrode. One dispersionless mode around 1.22 eV is observed matching the SWCNT E_{11} absorption line of the blend around 1020 nm (dashed black line, Figure 6.2a) and indicating weak light-matter coupling. By exchanging the ITO electrode with a 25 nm Au contact, the cavity quality is increased ($Q = 22$, Figure 6.2b). Two dispersive modes arise with a characteristic splitting at the exciton energy, indicating strong light-matter coupling (Figure 6.2b). The lower mode is attributed to the LP (dashed, white line) and the upper mode to the UP (dashed, yellow line). Upon increasing the blend layer thickness from 160 to 205 nm, the minimum energy of the LP shifts to lower energies (Figure 6.2c), with the UP becoming fainter and dispersionless (exciton-like) and the LP becoming stronger and more dispersive (photon-like). Note that the quality of the reflectivity data shown here is lower compared to the data presented in previous chapters. This can be attributed to the lower homogeneity of the blend film compared to SWCNTs in a PFO-BPy matrix, owing to phase separation between PC₇₀BM and P3HT in the blend. In all data sets, a set of narrow, faint modes is observed. This is caused by a cavity formed by the 1 mm glass substrate. The data in Figure 6.2a and b can be fitted with the CO-model, yielding the underlying cavity modes (solid grey line), the effective refractive index ($n_{\text{eff}} \approx 2.05$) and the Rabi splitting ($\hbar\Omega \approx 68$ meV). The refractive index is significantly higher than the RMS value of the employed cavity material refractive indices $n(\text{BPhen:CS/Blend/PEDOT:PSS}) \approx 1.7$. However, it matches the refractive index of the blend at respective cavity energies $n_{\text{Blend}}(1020\text{-}1180 \text{ nm}) \approx 1.95$, indicating that the blend dominates the linear optical response within the cavity. The full linear optical properties of the blend can be found in Appendix, section 8.2.1. The exciton fraction of the LP is 60 % for the thin blend layer and 5 % for the thick blend layer, as extracted from the CO-fit. With this, the cavity enhanced diodes meet the prerequisite of strong coupling and exhibit reasonably large exciton fractions for the LP. In the next section, the EQE and diode behavior of the strongly coupled OPDs is assessed.

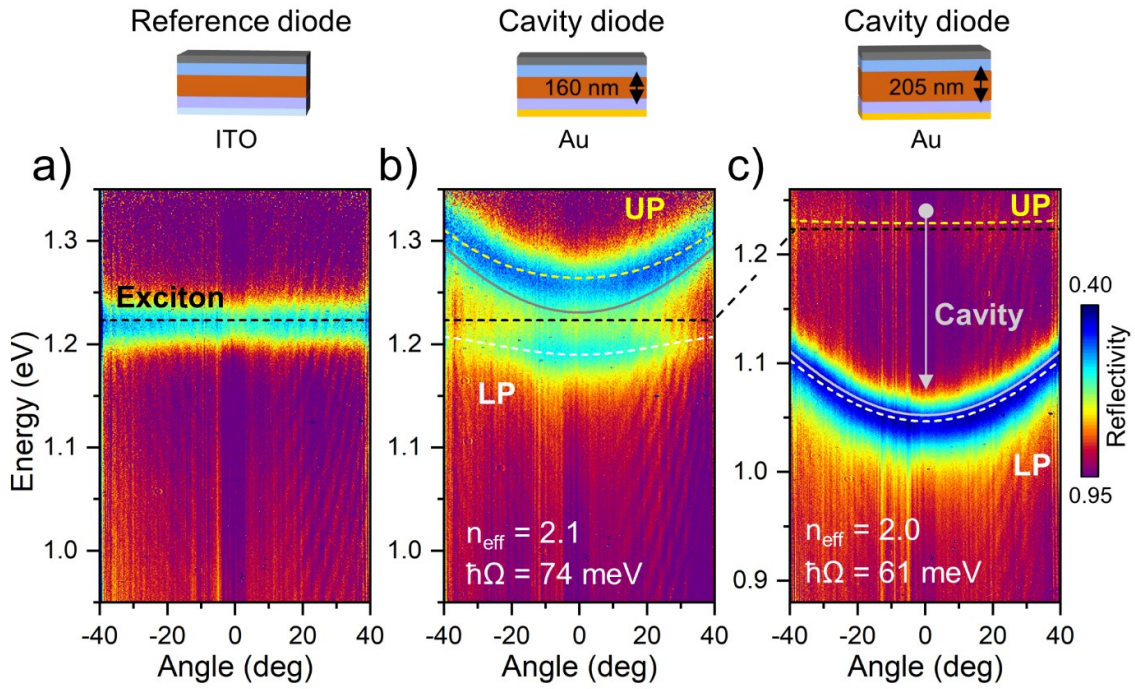


Figure 6.2 Angle-resolved reflectivity of a PC₇₀BM/SWCNT/P3HT bulk heterojunction (BHJ). **a)** For a reference device in a weak Ag-ITO cavity, **b)** for a strongly coupled photodiode in an Ag-Au cavity with a thin heterojunction layer and **c)** with a thick heterojunction layer. The sample structure is shown above each data set. The dark grey layer represents the Ag electrode, the light blue layer the Bphen:CS film, the brown layer the heterojunction blend and the light purple layer the PEDOT:PSS film. The blend layer thickness was calculated from a CO-fit to the experimental data. Dashed black lines indicate the exciton energy, grey solid lines give the cavity mode, dashed yellow lines show the upper and dashed white lines the lower polariton modes obtained from the CO-fit.

6.4 Tunable, strongly coupled photodetectors

In this section, photocurrent generation beyond the intrinsic SWCNT E₁₁ absorption in strongly coupled photodiodes is investigated. The photodiodes are characterized in terms of their EQE around the SWCNT E₁₁ absorption and their diode behavior. To tune the LP absorption, the natural wedge of the blend layer along the sample is exploited. Each sample structure contains 8 diode pixels, of which the center pixels comprise a large blend layer thickness and the outer pixels a small blend layer thickness. The data obtained for the cavity diodes is compared to a weakly coupled reference sample. A sketch of the sample structures is given in Figure 6.3.

Figure 6.3a depicts the EQE curves in the NIR, measured on 3 different pixels of a cavity sample, each corresponding to a different blend layer thickness (solid lines). The curves are color coded to indicate the $J-V$ curves for the respective pixel given in Figure 6.3b (see Experimental, section 3.3.2). The grey shaded area represents the EQE of three different pixels of a reference device with a blend layer of similar thickness. The EQE was collected under monochromatic light illumination without external bias (see Experimental, section 3.3.2). The modification of the SWCNT band edge should occur for negative detunings with the lower polariton being red-shifted with respect to the exciton. For the devices shown here, this should be the case for a thick blend layer (185-230 nm, center pixels Figure 6.3b).

In Figure 6.3a, two distinct EQE maxima are observed for the cavity diodes in the NIR region, whereas all reference diodes exhibit only one maximum around the SWCNT E_{11} absorption at 1022 nm (figure 6.3a, black arrow). The low energy EQE maxima of the cavity sample are shifted to higher wavelengths with increasing blend layer thickness (compare sample schematic in Figure 6.3b). This indicates that low energy EQE maxima arise from the LP mode. As the EQE maxima represent an increase of electrical charge generation, this is evidence for photocurrent generation from the LP. The high energy EQE maximum of the cavity sample coincides with reference E_{11} EQE peak and is most likely produced by uncoupled SWCNTs. The UP mode strongly overlaps with the E_{11} exciton (compare Figure 6.1c) and therefore cannot be distinguished from the E_{11} EQE peak with certainty. Note that due to the semi-transparent Au mirror and the distribution of SWCNTs throughout the blend, a high E_{11} contribution of uncoupled SWCNTs to the cavity EQE is expected.

The weakly coupled reference exhibits measurable EQE on the red flank of the E_{11} transition, which can be attributed to (6,5) SWCNT trions and impurities such as (10,5) SWCNTs (Figure 6.3a, grey arrows). These impurities, especially the trion, also contribute to the EQE of the strongly coupled photodiodes (e.g. broad peak of the red curve at 1160 nm, Figure 6.3a).

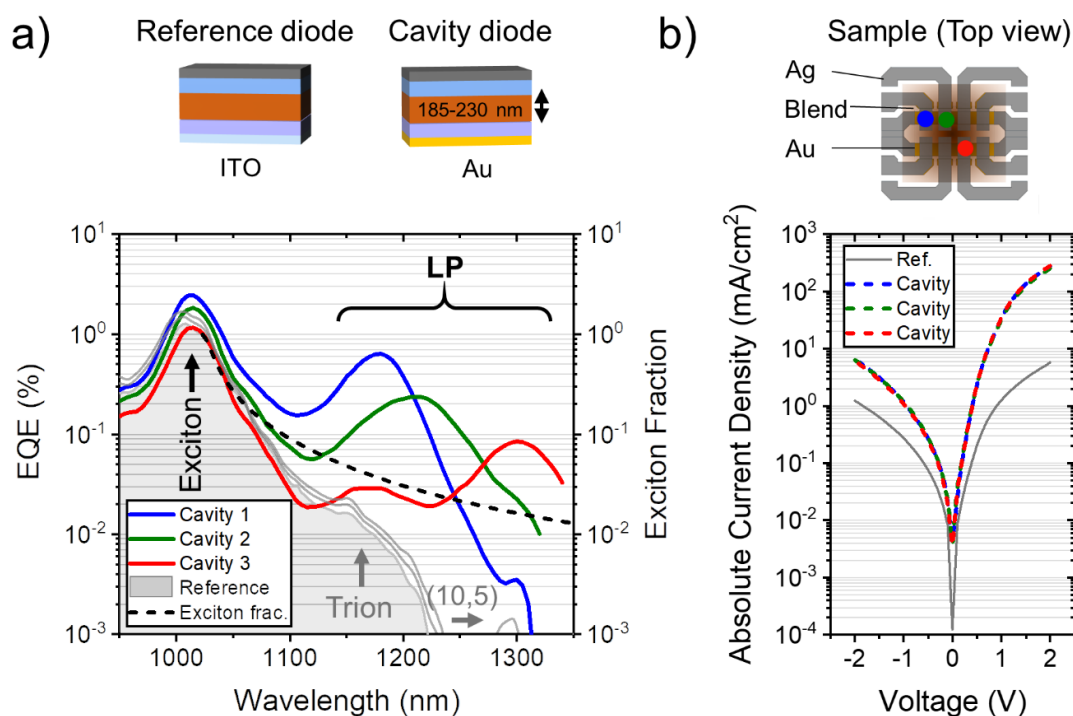


Figure 6.3 Device characteristics of strongly coupled photodetectors based on a PC₇₀BM:SWCNT:P3HT bulk heterojunction (BHJ). **a)** NIR-EQE of strongly coupled photodiodes (solid curves) in comparison to weakly coupled reference diodes (grey shaded area). The exciton fraction is indicated as black dashed line. **b)** J - V curves of the photodiodes depicted in **(a)** without illumination. On the top, the device structure is indicated with a top-view image to illustrate the pixel positions. The increasing blend layer thickness is represented by darker brown values.

Although the absolute EQE values for all photodiodes are low,²⁰⁷ the EQE spectra clearly support tunable modification of the SWCNT absorption edge by strong coupling. The LP EQE closely follows the exciton fraction (Figure 6.3a, black dashed line), confirming the previously made assumption, that the charge generation is connected to the exciton content of the polaritons.²⁵ This indicates, that extension of the absorption edge by strong coupling towards longer wavelengths becomes increasingly inefficient. Nevertheless, strongly coupled photodiodes should be able to operate further away from the intrinsic absorption than weakly coupled, cavity enhanced photodiodes, in which the efficiency scales directly with the underlying absorption¹⁷⁰, because the

exciton fraction decreases slower with increasing wavelength than the intrinsic SWCNT absorption (compare black dashed line to reference EQE spectra, Figure 6.3a).

An important device characteristic for photodiodes is the dark-current under reverse bias (see Background, section 2.4 for details). Figure 6.3b depicts the J - V curves of the photodiodes recorded without illumination. The zero bias dark current density of the reference device is comparable to values reported for P3HT:PC₇₁BM diodes, whereas the dark current density is more than one order of magnitude higher for the cavity diode.²¹⁵ There are indications, that the dark current in fullerene-polymer OPDs may be dominated by hole current.²¹⁶ Hence, the reduced barrier for holes at the HTL/Au interface of the cavity diode compared to the HTL/ITO interface of the reference device, might be the cause for the increased dark current.

Under reverse bias, all diodes exhibit high current densities and do not compare well to SWCNT-free OPDs.^{215, 216} Potentially, this is connected to SWCNTs bridging the HTL and ETL across the BHJ layer, as SWCNT-based photodiodes with FHJ layers, in which the SWCNTs are predominantly oriented parallel with respect to the electrodes, exhibit significantly lower dark currents under reverse bias.¹⁶⁷ Under forward bias, the dark currents are comparable to SWCNT-containing OSC,^{207, 217} which suggests that the bulk heterojunction device architecture is more suitable for photovoltaic applications.

In conclusion, the EQE spectra clearly show modification of the absorption edge of the (6,5) SWCNT by strong coupling enabling the generation of photocurrent up to 300 nm beyond the original E₁₁ absorption, however with low absolute EQE values. The device performance, especially with regard to the reverse bias dark current, is inferior to previously published SWCNT-free P3HT:PC₇₁BM devices.²¹⁵ In the next section, an alternative device structure is presented, employing a FHJ, that should reduce the negative impact of the SWCNTs on the diode behaviour and optimize the system for spectroscopic photodetection.

6.5 Strongly coupled flat heterojunction photodiodes

In order to create PC₇₀BM:SWCNT:P3HT FHJ, the active layer components were spin-coated subsequently on top of each other from orthogonal solvents (see Experimental, section 3.1.4 for details). This enables the use of higher spin-speeds for the individual layers, which should reduce the amount of SWCNTs protruding from the laterally oriented network. The final PC₇₁BM layer is meant to further flatten the SWCNTs and prevent direct contact to the ETL. However, subsequent spin-coating of three layers increases the surface roughness. Especially because the SWCNTs were spin-coated from toluene, in which P3HT is still partly soluble. Since the ETL and Ag mirror were evaporated, the roughness of the active layer could not be reduced in following layers. An illustration of the device structures is given on the top in Figure 6.4.

In the following, the optical and electrical device characteristics of strongly coupled photodetectors based on an FHJ and a BHJ layer will be compared. Figure 6.4a depicts the angle-dependent reflectivity spectrum of an FHJ cavity photodiode. As in the case of the BHJ, the spectra show splitting of the cavity mode into UP and LP, verifying strong coupling for the FHJ. Fitting the data with a CO-model reveals an even larger Rabi-splitting of 123 meV. This can be attributed to the increased SWCNT concentration at the field maximum of the cavity. The larger Rabi splitting leads to an increased exciton fraction of the LP for the same detuning compared to the BHJ. However, the modulation depth of the polariton modes is reduced by about 50% and the Q-factor based on the LP is reduced to $Q_{\text{FHJ}} = 15$. Both can be attributed to the increased film roughness of the FHJ and hence, reduction of the top mirror reflectivity. In Figure 6.4b, the EQE data of a cavity diode comprising an FHJ is presented (blue curve). Compared to the BHJ (brown curve), the EQE is increased about 3-fold. Potentially, this is caused by separating the exciton generation within the SWCNT from the exciton dissociation at the PC₇₀BM:SWCNT and SWCNT:P3HT interfaces. However, the EQE of the weakly coupled absorption is increased as well, resulting in less clearly resolved polariton EQE peaks as compared to the BHJ. This can be attributed to the decreased modulation depth of the polariton modes as observed in the device

reflectivity. Figure 6.4c shows the diode behaviour of the FHJ in comparison to the BHJ. Indeed, the dark current under reverse bias is reduced by one order of magnitude for employing the FHJ. However, it is still two orders of magnitude above values reported for state of the art OPDs²¹⁶ without SWCNTs.

As shown above, it was demonstrated that strongly coupled photodiodes based on FHJs improve the absolute EQE and diode behavior compared to BHJ photodiodes based on the same materials. However, the cavity quality is reduced by the increased layer roughness, which might also explain, why the device performance still remains below state of art OPDs.

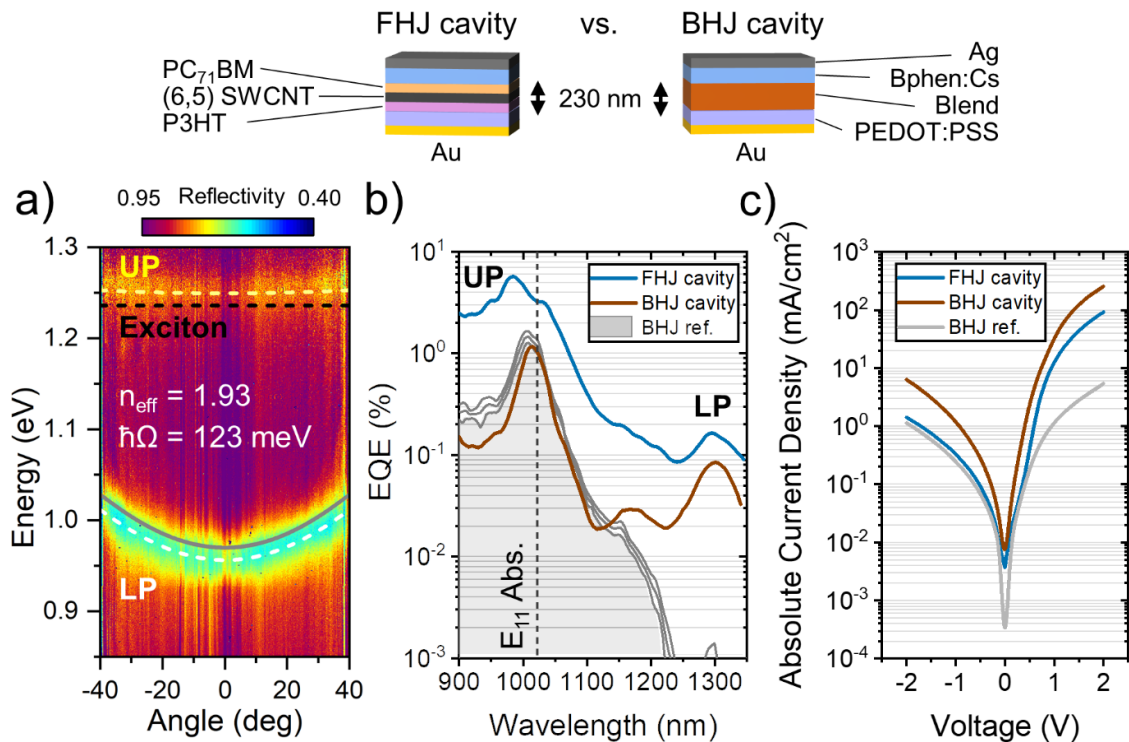


Figure 6.4 Comparison of strongly coupled photodetectors based on a flat heterojunction (FHJ) vs. a bulk heterojunction (BHJ). On the top, the corresponding device structures are indicated. **a)** Angle-resolved reflectivity of a cavity diode based on an FHJ. **b)** NIR-EQE of strongly coupled photodiodes based on an FHJ and BHJ (solid curves) with same detuning. The EQE of weakly coupled reference diodes (grey shaded area) is given for comparison. **c)** *J-V* curves of the photodiodes depicted in (a) without illumination.

6.6 Summary and conclusion

In summary, strong coupling can be used to manipulate and extend the absorption edge of photodiodes further into the NIR. The LP EQE approximately follows the exciton fraction, confirming previously made assumptions on the photoinduced charge generation from exciton-polaritons.²⁵ Employing strongly coupled SWCNTs, that possess excitons with narrow absorption bands in the NIR and large oscillator strengths, the absorption edge could be extended up to unprecedented 1300 nm for strongly coupled photodiodes^{25, 26} and far beyond the intrinsic nanotube band edge.

Strongly coupled photodiodes were demonstrated for BHJ and FHJ active layers based on a hybrid organic PC₇₀BM:SWCNT:P3HT system. The BHJ cavity photodiodes exhibit excellent tunability and reasonable quality factors considering the low reflectivity metal mirrors used to form the cavity. The dark current under reverse bias is inferior compared to state of the art SWCNT free OPDs^{215, 216}, but comparable to state of the art SWCNT based OSCs^{207, 217}, indicating that a BHJ active layer is more suitable for photovoltaic applications. Improving the energy alignment of the electron side of the device using a Ca layer and Al cathode layer could enable performances equal to state of the art SWCNT based OSCs²⁰⁷ with extended NIR absorption. This approach may reduce the zero bias dark current as well.²¹⁶ However for spectroscopic photodiodes, the lower Al reflectivity would have to be compensated by an additional mirror, to retain the LP linewidths presented here. Spectroscopic photodiodes, based on an FHJ layer may be more promising. For the FHJ layer EQE and dark currents under reverse bias are significantly improved and therefore the specific detectivity should be increased compared to the BHJ devices (see Background, section 2.4 for details). For strongly coupled FHJ photodiodes, the probability of SWCNTs bridging the ETL and HTL is reduced, which is supposedly the major reason for the high dark currents under external bias compared to SWCNT free OPDs.^{215, 216} To improve the FHJ device performance further, the active layer roughness and film homogeneity has to be improved. This could either be achieved by optimizing the orthogonal solvent system for the three sequential

spin-coating steps or by adapting the device stack to C_{60} as an acceptor material, which can be evaporated.

In conclusion, strong light-matter coupling can be a viable route to extend the absorption of OPDs further into the NIR, circumventing the lack of suitable organic absorbers. Although, this approach is limited at very large detunings by the low exciton fraction, using larger diameter SWCNTs may enable reasonably large EQEs above 1300 nm.

7 Conclusion and Outlook

At the start of this thesis, SWCNTs had been established as an excellent material for strong light-matter coupling.^{40-45, 56} However, in contrast to other disordered semiconductors, including small organic molecules^{7, 13, 14}, conjugated polymers^{15, 16} and fluorescent proteins^{17, 18} as well as other nanomaterials, such as transition metal dichalcogenides²¹⁸ or 2D perovskites²¹⁹, polariton condensation has not been observed for SWCNTs yet. This raised the question on how SWCNT exciton-polaritons are populated. Exploring the population mechanisms and dynamics between emitters and exciton-polaritons is indeed of general interest to the field of room-temperature polaritonics. So far, there are only a few experimental studies on the exciton-polariton dynamics in disordered semiconductors, concerning both emissive^{57, 80, 86, 87, 220} and non-emissive states^{91-93, 186-189, 221, 222}. Especially the lack of a comparative study of the polariton fluorescence dynamics testing multiple different proposed mechanisms, underlines the need for more systematic investigations.

In this thesis polymer-sorted (6,5) SWCNT were used for the first comparative study of population mechanisms in exciton-polaritons, establishing radiative pumping as the dominant mechanism for strongly coupled SWCNTs and using luminescent sp^3 defects to increase the polariton population (Chapter 4). A polariton-mediated biexciton transition was identified by ultrafast pump-probe experiments (Chapter 5) and strongly coupled, tunable SWCNT photodetectors were realized (Chapter 6).

SWCNTs possess diverse photophysics offering the possibility to investigate the influence of different material properties such as phonons or defects on the same polaritons created from the fundamental exciton. Owing to this advantage, SWCNT exciton-polaritons could be shown to be pumped radiatively and other processes, such as population by scattering with phonons, could be

excluded. The SWCNT polariton population is limited by the low SWCNT PLQY, most likely impeding polariton condensations at high-excitation densities. This limit could be overcome by functionalizing the SWCNTs with luminescent sp^3 defects, leading to a population increase up to 10-fold for highly emissive detunings (photon fractions $> 90\%$). By changing the substituents and the binding pattern, tuning of the defect emission could be further employed to access application-relevant NIR wavelengths. In summary, luminescent sp^3 defects constitute a viable and versatile approach towards bright and efficient SWCNT-based polariton devices through radiative pumping.

With these findings, the prospect of polariton condensation in SWCNT can be assessed. Although radiative pumping limits the polariton population to the PLQY of the emitter, polariton condensation has been shown for a small organic molecule¹³, for which radiative pumping was observed and that possessed a moderate PLQY of around 15 % in film⁸⁰. Future experiments on strongly coupled sp^3 -functionalized SWCNTs in high quality cavities can show whether polariton condensation is possible for SWCNTs with increased PLQY ($\sim 2\%$ in film). For this however, not only the increase in PLQY is important, but also the absence of photo-induced species at the defect emission wavelength, that lead to additional absorption at high pump-fluences. For the E_{11}^* transition transient generation of trions is believed to reduce emission efficiency at high-fluences.²²³ Hence, targeting the red-shifted E_{11}^* configuration should be most promising.⁵¹

The non-polaritonic transient cavity response caused by the pump-induced SWCNT bleach was modeled using TM simulations and fitted to the experimental data by a genetic algorithm. This enabled identification of an absorptive feature, which was shown to be a direct UP to biexciton transition. So far, this transition had been only observed for inorganic semiconductors at cryogenic temperatures¹⁹³. The biexciton transition efficiency was shown to be increased three times compared to weakly coupled SWCNTs and could be increased further up to fourfold under resonant UP excitation, effectively bypassing the dark state dynamics. The observation that a UP to biexciton transition exist even under off-resonant excitation of the underlying SWCNT can be

taken as evidence for fast population transfer from the dark states to the UP polariton beyond the exciton and photon dephasing times. The efficient biexciton transition of strongly coupled SWCNT may enable to study correlated many-body states at room temperature, that are predicted for excitonic molecules in strongly coupled high quality cavities.²⁰⁰

For the study of ultrafast dynamics of exciton-polaritons, the major hurdle is the dominance of non-polaritonic effects in the cavity transient transmission and reflectivity spectra.^{176, 184} In absence of a polariton intrinsic transition, such as the UP to biexciton feature, the one-dimensional transient spectra contain no direct information on the polariton transient absorption. This problem could be overcome by carefully referencing the different contributions of the non-polaritonic cavity response in experiment to achieve a small uncertainty of the fitted TM simulation. Alternatively, the transient transmission and reflectivity could be measured simultaneously. Both methods would then allow to calculate the full polariton transient absorption spectrum. These data on ultrafast dynamics of non-emissive states is relevant to many other applications of strong light-matter coupling, such as photocurrent-generation²⁵⁻²⁷ and spin conversion²⁸⁻³², with the latter one remaining to be explored for strongly coupled SWCNTs.

SWCNTs are also a promising material for light-harvesting in the NIR, due to their high oscillator strength and carrier mobilities.^{204, 207, 217, 224, 225} For such applications, strong light-matter coupling can be used to tune the absorption further into the NIR²⁵ and reducing the Urbach energy in solarcells²⁶. Strongly coupled photodiodes based on a hybrid organic PC₇₀BM:SWCNT:P3HT active layer were presented. Although, the photodiode dark currents were found to be very high (up to 1 mA cm⁻² under reverse bias), shifting the SWCNT absorption edge up to 1300 nm into the NIR was demonstrated, a value unprecedented for strongly coupled photodiodes^{25, 26}. Higher EQE values and lower dark currents were achieved for devices based on a flat heterojunction, with the SWCNTs sandwiched between the PC₇₀BM and P3HT layer. This in combination with an improved energy alignment of electrodes, charge transport layers and active layer materials, may improve strongly coupled SWCNT photodiodes to reach state-of-art performance.

In summary, this work demonstrates the complexity but also versatility of strongly coupled SWCNTs in terms of studying polariton dynamics as well as their potential for device application. Furthermore, this thesis emphasizes the importance of time-resolved spectroscopy on exciton-polaritons and its limitations. By overcoming the challenges highlighted above, SWCNT exciton-polaritons may become a candidate for real-world applications of hybrid light-matter particles.

8 Appendix

This chapter shows additional calculations and data for Chapters 4 and 6 in order of appearance.

8.1 Chapter 4

8.1.1 LP emission as a function of detuning for scattering with acoustic phonons

In the following, the kinetic model developed by Litinskaya *et al.*⁹⁸ for J-aggregates is used, to describe polariton population by scattering with acoustic phonons in the case of a microcavity containing a strongly coupled SWCNT network (see Chapter 4, section 4.4 for a justification). From this, an expression is derived that gives the change in polariton emission intensity as a function of detuning for population by acoustic phonon scattering.

Following Litinskaya *et al.*⁹⁸, a three-state kinetic model is assumed, in which the exciton reservoir population N_{ER} , is injected by a pump term P and population is scattered into the UP and LP polariton states by absorption or emission of a localized vibrations, where n_v is the phonon thermal population. In case of a SWCNT network, the vibrations would be the acoustic phonons localized by disorder. For simplicity, a continuum of phonons is assumed. Note that the density of states of delocalized acoustic phonons on the single SWCNT level exhibit singularities¹⁸⁰, that would lead to characteristic progression of PL intensity spikes, which is not observed (compare Chapter 4, section 4.3). The rate equations are

$$\frac{dN_{\text{ER}}}{dt} = P - W_{\text{LP}}N_{\text{ER}}(n_v + 1) - W_{\text{UP}}N_{\text{ER}}n_v, \quad (55)$$

$$\frac{dN_{\text{UP}}}{dt} = W_{\text{UP}}N_{\text{ER}}n_v - \gamma_{\text{UP}}N_{\text{UP}}, \quad (56)$$

$$\frac{dN_{LP}}{dt} = W_{LP}N_{ER}(n_v + 1) - \gamma_{LP}N_{LP}, \quad (57)$$

where $\gamma_{LP/UP}$ is the polariton radiative decay and $W_{LP/UP}$ are the scattering rates for LP and UP.

In steady state, the UP and LP populations reduce to

$$N_{UP} = \frac{W_{UP}}{\gamma_{UP}} N_{ER} n_v, \quad (58)$$

$$N_{LP} = \frac{W_{LP}}{\gamma_{LP}} N_{ER} (n_v + 1). \quad (59)$$

The vibrational quanta n_v introduce the temperature dependence of the polariton emission and they can be treated as a temperature dependent constant given by the UP/LP intensity ratio

$$C(T) = \frac{I_{UP}}{I_{LP}} \propto \frac{n_v}{(n_v + 1)} = e^{-\hbar\omega/kT}. \quad (60)$$

Litinskaya *et al.*⁹⁸ derived an explicit expression for $W_{LP/UP}$

$$W_{LP/UP} = \frac{D_{LP/UP}(k) |\beta_{LP/UP}|^2}{N_{agg}} O_{i,I}^{(ex-pol)} W_{agg}(\Delta E), \quad (61)$$

where $\beta_{LP/UP}$ is the exciton fraction, $O_{i,I}^{(ex-pol)}$ is the overlap the overlap between the i -th exciton of I -th aggregate and polariton state. For SWCNTs that is equivalent to the i -th exciton of the I -th nanotube. In the following, the distribution function of these states is considered and the indices are dropped. $D_{LP/UP}(k)$ is the density of polariton states. W_{agg} is an empirical function for the scattering rate in J-aggregates, that selects local vibrations that fulfill the energy conservation condition ΔE for a scattering event from the i -th exciton of I -th aggregate into a polariton state. For a continuum of phonons, W_{agg} has no detuning dependence. For a sufficiently small region around $k_{\parallel} = 0$, it can be assumed that $D_{LP/UP}(0)$ is constant with detuning. Together with the expressions for polariton decay $\gamma_{LP/UP}$

$$\gamma_{LP/UP} = \frac{\gamma_C}{|\alpha_{LP/UP}|^2} \quad (62)$$

and using the relationship $I \propto N_{LP/UP} |\alpha_{LP/UP}|^2$, the detuning dependence of the PL intensity $I_{LP/UP}(\Delta)$ can be written as

$$I_{LP/UP}(\Delta) \propto \frac{|\beta_{LP/UP}|^2}{\gamma_C} O^{(ex-pol)}(\Delta). \quad (63)$$

By measuring the PL intensity I_{LP}^0 at $k_{\parallel} = 0$ of a detuning for which the population contributions from vibrationally assisted scattering or radiative pumping are small, the LP emission intensity $I_{LP}(\Delta)$ for other detunings relative to I_{LP}^0 can be calculated by

$$I_{LP}(\Delta) = \frac{|\beta_{LP}|^2}{\gamma_C} O^{(ex-pol)}(\Delta) \frac{I_{LP}^0}{P^0}, \quad (64)$$

$$P^0 = \frac{|\beta_{LP}^0|^2}{\gamma_C} O_0^{(ex-pol)}, \quad (65)$$

where P^0 corrects I_{LP}^0 for contributions of other population mechanisms at the reference detuning. The calculation is done for the oxide spacer metalclad cavities based on the data shown in Figure 4.5a of Chapter 4. $|\beta_{LP}|^2$ can be extracted from the CO fit to the reflectivity data. For I_{LP}^0 the area of a Lorentzian-fit to the experimental LP emission at $\Delta = -355$ meV is used. To calculate the other relative PL intensities, the Lorentzian amplitude was scaled by equation (10). Linewidth and LP positions were extracted from the respective reflectivity data, to account for the broadening of the polariton states close to the exciton. The overlap between polariton branches and exciton reservoir was approximated by the overlap between the polariton mode in reflectivity and an area of the same sample without top mirror. The results are shown in Figure 4.5b of Chapter 4.

8.1.2 Estimate of mean exciton distance

In the following, the mean SWCNT exciton density for fluorescence decay measurements is estimated in order to calculate the VAS rate. The samples were excited at the E_{22} transition (575 nm) with pulsed laser light (20 MHz, ~6 ps pulse width). The average laser power was ~100 μ W corresponding to 1.4×10^7 photons per pulse. The E_{22} absorption in film was determined to be ~0.15 for the pristine and ~0.1 for the functionalized, corresponding to ~29 % and ~21 % absorption of incident photons. For simplicity, the average value is used to describe VAS for functionalized and pristine SWCNTs. The E_{22} to E_{11} conversion efficiency was found to be around 91 %.²²⁶ However, complete E_{22} to E_{11} conversion takes about 5 ps and consequently E_{11} excitons can already diffuse to quenching sites or sp^3 defects and do not lead to VAS on the timescale of the fluorescence lifetime measurement.¹¹⁰ Therefore, only the fraction of freely diffusing excitons is regarded. This fraction can be estimated *via* the absolute PLQY of the pristine film (~0.2 %). Accounting for the aforementioned, $6.4 \cdot 10^3$ of the excitons created per pulse could contribute to VAS. The excited volume is estimated from the excitation spot diameter of ~2 μ m and the SWCNT film thickness of ~80 nm, yielding 10^{-12} cm^3 and the corresponding exciton density is $6.4 \cdot 10^{15}$ cm^{-3} . From this, the mean exciton distance can be approximated by the Wigner-Seitz radius, assuming that the SWCNT are homogeneously distributed throughout the polymer matrix, which yields 155 nm. The uncertainty of the mean exciton distance mainly arises from the uncertainty in exciton density due to fluctuations of the laser pulse power and the excitation spot diameter.

8.1.3 Polariton fluorescence decay lifetime in the limit of VAS

The scattering rate for vibrationally assisted scattering W_{VAS} in the adiabatic approximation is adapted for SWCNTs in metalclad cavities is adapted in the following and given by⁹⁸

$$W_{\text{VAS}} = \left(\frac{a}{L_c}\right)^3 \frac{\pi^2 g^2 (\Omega/2)^2 E_c(k_0^2)}{\hbar E_c^2(0)} = 1/\tau_{\text{VAS}}, \quad (66)$$

where the mean distance between molecules (a) was exchanged with the mean distance of excitons in SWCNTs (155 nm, see previous section for details). The cavity length was approximated by $L_c = \frac{\lambda_{\text{res}}}{2n_{\text{eff}}}$, where λ_{res} is the resonant wavelength and n_{eff} is the cavity effective refractive index. For the dimensionless exciton-phonon coupling constant g the value for the G phonon was used ($g_G = 0.9$).²²⁷ The coupling constants for the remaining SWCNT optical phonons were only determined theoretically, but should have comparable magnitudes to g_G .⁷ To simplify the calculation, the existence of an optical phonon with suitable energy for every cavity detuning is assumed and g_G is used as the coupling constant. $E_c(k_0^2)$ is the cavity energy at $k_{\parallel} = k_0$, at which the optical phonon with energy E_{vib} matches the energy difference between exciton reservoir and LP $\Delta E = E_X - E_{\text{LP}}(k_0^2)$. $E_c(0)$ is the cavity energy at $k_{\parallel} = 0$. The cavity parameters and Rabi splitting $\hbar\Omega$, are taken from cavity data presented in Figures 4.3, 4.4, 4.10 and 4.11 in Chapter 4. With these values the lifetime is calculated to vary between $\tau_{\text{VAS}} \approx 90 - 500$ fs, depending on the cavity detuning. The results are shown in Figure 4.7 for pristine and Figure 4.14 for functionalized SWCNTs in Chapter 4.

8.1.4 Excitation efficiency correction for population analysis

Due to a shift of the cavity λ -mode at visible wavelengths, the excitation efficiency inside the oxide spacer cavities changes strongly with detuning. In order to correct for the change in excitation efficiency, the electric field intensity inside each structure was simulated for the wavelength of the excitation laser (640 nm). The spectral shape of the laser was neglected, as the laser linewidth (± 2 nm) was small compared to the cavity resonance (± 9 nm). The electric field was simulated using the TM scheme (Background, section 2.1.2). The mode positions of the experimental reflectivity data were matched by adjusting the SWCNT thickness, while keeping the mirror and oxide spacer thicknesses fixed. With this, the overlap between electric field and active layer was calculated (Figure A8.1) and normalized to the smallest field overlap (1.83) to

obtain the correction factors (Chapter 4, Figure 4.16b). The uncertainties of the correction factors were determined as described in the following.

The simulation input with the highest uncertainty is the SWCNT layer thickness. This uncertainty is given by the standard deviation of the change in SWCNT layer thicknesses (1.8 nm) used to match the TM simulation to the experimental data. This to an error in the LP position of the correction factors, because the correction factors are mapped to the sample using the nominal spacer thickness (th_{spacer}). Furthermore, close to the λ mode, even a small change in SWCNT layer thickness leads to a considerable change in excitation efficiency. To account for both effects, the standard deviation of the SWCNT layer thickness (th_{SWCNT}) was weighted with the slope of a Bézier interpolation of the correction factors (Chapter 4, Figure 4.16b):

$$\Delta(th_{SWCNT}) = STD(th_{SWCNT}) \cdot \left(1 + 100 \cdot \left| \frac{\partial \text{BézierInterpol.}}{\partial th_{spacer}} \right| \right). \quad (67)$$

This error can be converted to the error in LP position as follows: Firstly, the optical cavity length (th_{cav}) in TM-polarization is calculated for the strongly coupled $\lambda/2$ mode (assuming the refractive indices n to be constant for the spectral range in question) with

$$th_{cav} = (th_{SWCNT} \cdot 2 \cdot n_{SWCNT, TM}) + (th_{spacer} \cdot 4 \cdot n_{spacer, TM}). \quad (68)$$

Next, the error with respect to the uncertainty in SWCNT thickness is calculated by

$$\Delta th_{cav} = (\Delta th_{SWCNT} \cdot 2 \cdot n_{SWCNT, TM}). \quad (69)$$

Using error propagation, the uncertainty is converted from wavelength to energy units

$$\Delta th_{cav} [eV] = (hc/th_{cav}^2) \cdot \Delta th_{cav}. \quad (70)$$

Additionally, the correction factor has an uncertainty, owing to the assumptions made in the beginning of this section. The error is estimated heuristically by the difference of B-spline interpolation of the correction factors (Chapter 4, Figure 4.16b). This measure accounts for the

fact, that the error of the correction factor should be higher for a strong change in overlap, owing to the error in LP position.

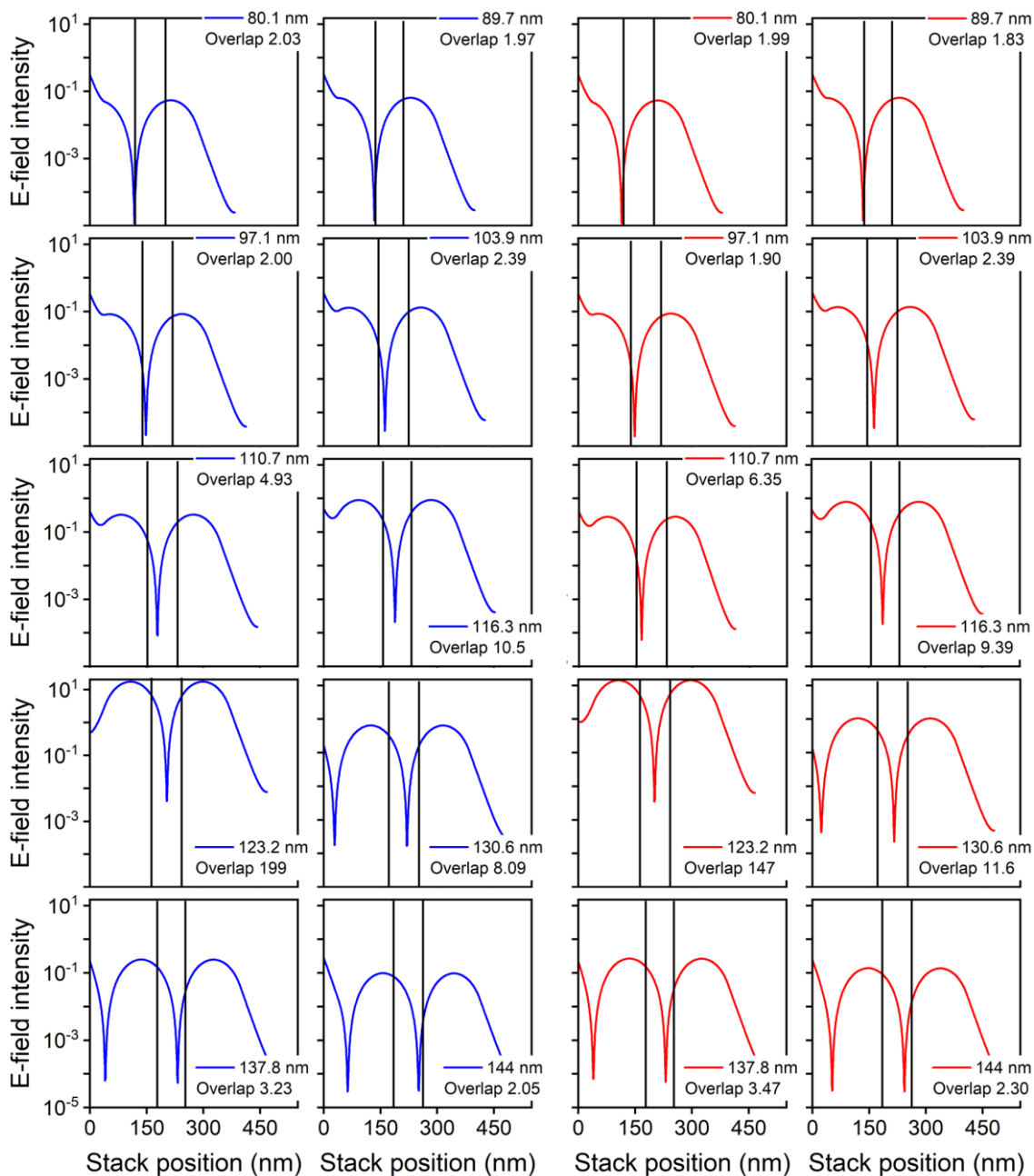


Figure A8.1. Electric field intensity simulated for different stack positions in cavities with pristine (blue) and functionalized SWCNTs (red). Black solid lines indicate the position of the SWCNT layer. The integral of the electric field intensity within the SWCNT layer was yielded the overlap.

8.2 Chapter 6

8.2.1 Linear optical properties of the PC₇₀BM/SWCNT/P3HT blend

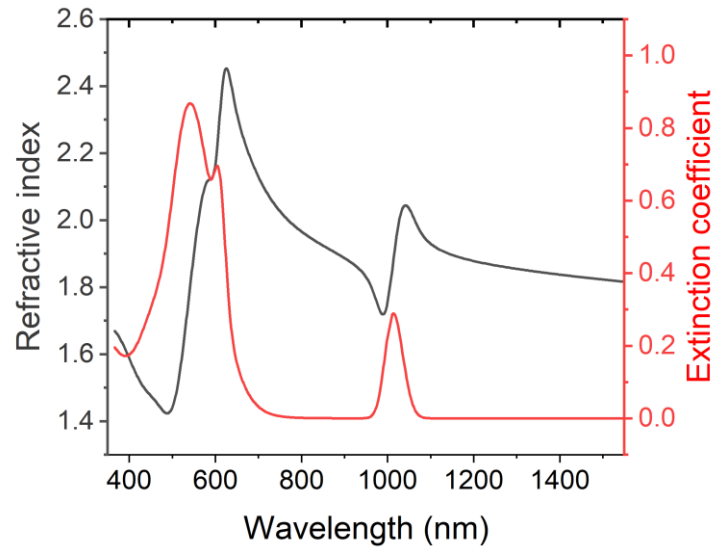


Figure A8.2. Refractive index (n) and extinction coefficient (k) of the PC₇₀BM/SWCNT/P3HT mixed layer modelled from spectroscopic ellipsometry on polished silicon using Lorentzian lineshapes. The average refractive index is approximately 1.8 in the NIR. The exact spectrum might vary slightly depending on the blend composition for the different devices shown. Data was modelled by Dr. Andreas Mischock.

9 References

1. Sanvitto, D.; Kéna-Cohen, S., The road towards polaritonic devices. *Nat. Mater.* **2016**, *15* (10), 1061-1073. doi: 10.1038/nmat4668
2. Henry, C. H.; Hopfield, J. J., Raman Scattering by Polaritons. *Phys. Rev. Lett.* **1965**, *15* (25), 964-966. doi: 10.1103/PhysRevLett.15.964
3. Morris, G. C.; Sceats, M. G., The 4000 Å transition of crystal anthracene. *Chem. Phys.* **1974**, *3* (2), 164-179. doi: 10.1016/0301-0104(74)80058-3
4. Yoshihisa Yamamoto; Francesco Tassone; Cao, H., Semiconductor Cavity Quantum Electrodynamics. *Phys. Today* **2001**, *169*, 25. doi:
5. Weisbuch, C.; Nishioka, M.; Ishikawa, A.; Arakawa, Y., Observation of the coupled exciton-photon mode splitting in a semiconductor quantum microcavity. *Phys. Rev. Lett.* **1992**, *69* (23), 3314-3317. doi: 10.1103/PhysRevLett.69.3314
6. Kasprzak, J.; Richard, M.; Kundermann, S.; Baas, A.; Jeambrun, P.; Keeling, J. M. J.; Marchetti, F. M.; Szymańska, M. H.; André, R.; Staehli, J. L.; Savona, V.; Littlewood, P. B.; Deveaud, B.; Dang, L. S., Bose–Einstein condensation of exciton polaritons. *Nature* **2006**, *443* (7110), 409-414. doi: 10.1038/nature05131
7. Kéna-Cohen, S.; Forrest, S. R., Room-temperature polariton lasing in an organic single-crystal microcavity. *Nat. Photon.* **2010**, *4* (6), 371-375. doi: 10.1038/nphoton.2010.86
8. Baumberg, J. J.; Kavokin, A. V.; Christopoulos, S.; Grundy, A. J. D.; Butté, R.; Christmann, G.; Solnyshkov, D. D.; Malpuech, G.; Baldassarri Höger von Högersthal, G.; Feltn, E.; Carlin, J. F.; Grandjean, N., Spontaneous Polarization Buildup in a Room-Temperature Polariton Laser. *Phys. Rev. Lett.* **2008**, *101* (13), 136409. doi: 10.1103/PhysRevLett.101.136409
9. Daskalakis, K. S.; Maier, S. A.; Kéna-Cohen, S., Spatial Coherence and Stability in a Disordered Organic Polariton Condensate. *Phys. Rev. Lett.* **2015**, *115* (3). doi: 10.1103/PhysRevLett.115.035301
10. Lerario, G.; Fieramosca, A.; Barachati, F.; Ballarini, D.; Daskalakis, K. S.; Dominici, L.; De Giorgi, M.; Maier, S. A.; Gigli, G.; Kéna-Cohen, S.; Sanvitto, D., Room-temperature superfluidity in a polariton condensate. *Nat. Phys.* **2017**, *13* (9), 837-841. doi: 10.1038/nphys4147
11. Schneider, C.; Rahimi-Iman, A.; Kim, N. Y.; Fischer, J.; Savenko, I. G.; Amthor, M.; Lerner, M.; Wolf, A.; Worschech, L.; Kulakovskii, V. D.; Shelykh, I. A.; Kamp, M.; Reitzenstein, S.; Forchel, A.; Yamamoto, Y.; Höfling, S., An electrically pumped polariton laser. *Nature* **2013**, *497* (7449), 348-352. doi: 10.1038/nature12036
12. Tsintzos, S. I.; Pelekanos, N. T.; Konstantinidis, G.; Hatzopoulos, Z.; Savvidis, P. G., A GaAs polariton light-emitting diode operating near room temperature. *Nature* **2008**, *453* (7193), 372-375. doi: 10.1038/nature06979
13. Cookson, T.; Georgiou, K.; Zasedatelev, A.; Grant, R. T.; Virgili, T.; Cavazzini, M.; Galeotti, F.; Clark, C.; Berloff, N. G.; Lidzey, D. G.; Lagoudakis, P. G., A Yellow Polariton Condensate in a Dye Filled Microcavity. *Adv. Opt. Mater.* **2017**, *5* (18), 1700203. doi: 10.1002/adom.201700203
14. Daskalakis, K. S.; Maier, S. A.; Murray, R.; Kéna-Cohen, S., Nonlinear interactions in an organic polariton condensate. *Nat. Mater.* **2014**, *13* (3), 271-278. doi: 10.1038/nmat3874
15. Plumhof, J. D.; Stöferle, T.; Mai, L.; Scherf, U.; Mahrt, R. F., Room-temperature Bose–Einstein condensation of cavity exciton–polaritons in a polymer. *Nat. Mater.* **2013**, *13* (3), 247-252. doi: 10.1038/nmat3825
16. Wei, M.; Rajendran, S. K.; Ohadi, H.; Tropf, L.; Gather, M. C.; Turnbull, G. A.; Samuel, I. D. W., Low-threshold polariton lasing in a highly disordered conjugated polymer. *Optica* **2019**, *6* (9), 1124-1129. doi: 10.1364/OPTICA.6.001124

17. Dietrich, C. P.; Steude, A.; Tropf, L.; Schubert, M.; Kronenberg, N. M.; Ostermann, K.; Höfling, S.; Gather, M. C., An exciton-polariton laser based on biologically produced fluorescent protein. *Sci. Adv.* **2016**, *2* (8), e1600666. doi: 10.1126/sciadv.1600666
18. Betzold, S.; Dusel, M.; Kyriienko, O.; Dietrich, C. P.; Klemmt, S.; Ohmer, J.; Fischer, U.; Shelykh, I. A.; Schneider, C.; Höfling, S., Coherence and Interaction in Confined Room-Temperature Polariton Condensates with Frenkel Excitons. *ACS Photonics* **2019**, *7* (2), 384-392. doi: 10.1021/acsp Photonics.9b01300
19. Putintsev, A.; Zasedatelev, A.; McGhee, K. E.; Cookson, T.; Georgiou, K.; Sannikov, D.; Lidzey, D. G.; Lagoudakis, P. G., Nano-second exciton-polariton lasing in organic microcavities. *Appl. Phys. Lett.* **2020**, *117* (12). doi: 10.1063/5.0019195
20. Rajendran, S. K.; Wei, M.; Ohadi, H.; Ruseckas, A.; Turnbull, G. A.; Samuel, I. D. W., Low Threshold Polariton Lasing from a Solution-Processed Organic Semiconductor in a Planar Microcavity. *Adv. Opt. Mater.* **2019**, *7* (12). doi: 10.1002/adom.201801791
21. Sannikov, D.; Yagafarov, T.; Georgiou, K.; Zasedatelev, A.; Baranikov, A.; Gai, L.; Shen, Z.; Lidzey, D.; Lagoudakis, P., Room Temperature Broadband Polariton Lasing from a Dye-Filled Microcavity. *Adv. Opt. Mater.* **2019**, *7* (17). doi: 10.1002/adom.201900163
22. Sabatini, R. P.; Maasoumi, F.; Prasad, S. K. K.; Zhang, B.; Clark, C.; Schmidt, T. W.; Wong, W. W. H.; Lakhwani, G., Organic polariton lasing with molecularly isolated perylene diimides. *Appl. Phys. Lett.* **2020**, *117* (4). doi: 10.1063/5.0012461
23. Zasedatelev, A. V.; Baranikov, A. V.; Urbonas, D.; Scafirimuto, F.; Scherf, U.; Stöferle, T.; Mahrt, R. F.; Lagoudakis, P. G., A room-temperature organic polariton transistor. *Nat. Photon.* **2019**, *13* (6), 378-383. doi: 10.1038/s41566-019-0392-8
24. Ebbesen, T. W., Hybrid Light–Matter States in a Molecular and Material Science Perspective. *Acc. Chem. Res.* **2016**, *49* (11), 2403-2412. doi: 10.1021/acs.accounts.6b00295
25. Eizner, E.; Brodeur, J.; Barachati, F.; Sridharan, A.; Kéna-Cohen, S., Organic Photodiodes with an Extended Responsivity Using Ultrastrong Light–Matter Coupling. *ACS Photonics* **2018**, *5* (7), 2921-2927. doi: 10.1021/acsp Photonics.8b00254
26. Nikolis, V. C.; Mischok, A.; Siegmund, B.; Kublitski, J.; Jia, X.; Benduhn, J.; Hörmann, U.; Neher, D.; Gather, M. C.; Spoltore, D.; Vandewal, K., Strong light-matter coupling for reduced photon energy losses in organic photovoltaics. *Nat. Commun.* **2019**, *10* (1). doi: 10.1038/s41467-019-11717-5
27. Mischok, A.; Lüttgens, J.; Berger, F.; Hillebrandt, S.; Tenopala-Carmona, F.; Kwon, S.; Murawski, C.; Siegmund, B.; Zaumseil, J.; Gather, M. C., Spectroscopic near-infrared photodetectors enabled by strong light–matter coupling in (6,5) single-walled carbon nanotubes. *J. Chem. Phys.* **2020**, *153* (20). doi: 10.1063/5.0031293
28. Stranius, K.; Hertzog, M.; Börjesson, K., Selective manipulation of electronically excited states through strong light–matter interactions. *Nat. Commun.* **2018**, *9* (1). doi: 10.1038/s41467-018-04736-1
29. Eizner, E.; Martínez-Martínez, L. A.; Yuen-Zhou, J.; Kéna-Cohen, S., Inverting singlet and triplet excited states using strong light-matter coupling. *Sci. Adv.* **2019**, *5* (12). doi: 10.1126/sciadv.aax4482
30. Berghuis, A. M.; Halpin, A.; Le-Van, Q.; Ramezani, M.; Wang, S.; Murai, S.; Gómez Rivas, J., Strong Light-Matter Coupling: Enhanced Delayed Fluorescence in Tetracene Crystals by Strong Light-Matter Coupling (Adv. Funct. Mater. 36/2019). *Adv. Funct. Mater.* **2019**, *29* (36). doi: 10.1002/adfm.201970249
31. Polak, D.; Jayaprakash, R.; Lyons, T. P.; Martínez-Martínez, L. Á.; Leventis, A.; Fallon, K. J.; Coulthard, H.; Bossanyi, D. G.; Georgiou, K.; Petty, I. I. A. J.; Anthony, J.; Bronstein, H.; Yuen-Zhou, J.; Tartakovskii, A. I.; Clark, J.; Musser, A. J., Manipulating molecules with strong coupling: harvesting triplet excitons in organic exciton microcavities. *Chem.* **2020**, *11* (2), 343-354. doi: 10.1039/c9sc04950a
32. Yu, Y.; Mallick, S.; Wang, M.; Börjesson, K., Barrier-free reverse-intersystem crossing in organic molecules by strong light-matter coupling. *Nat. Commun.* **2021**, *12* (1). doi: 10.1038/s41467-021-23481-6

33. Georgiou, K.; Michetti, P.; Gai, L.; Cavazzini, M.; Shen, Z.; Lidzey, D. G., Control over Energy Transfer between Fluorescent BODIPY Dyes in a Strongly Coupled Microcavity. *ACS Photonics* **2017**, *5* (1), 258-266. doi: 10.1021/acsp Photonics.7b01002
34. Zhong, X.; Chervy, T.; Zhang, L.; Thomas, A.; George, J.; Genet, C.; Hutchison, J. A.; Ebbesen, T. W., Energy Transfer between Spatially Separated Entangled Molecules. *Angew. Chem. Int. Ed.* **2017**, *56* (31), 9034-9038. doi: 10.1002/anie.201703539
35. Rozenman, G. G.; Akulov, K.; Golombek, A.; Schwartz, T., Long-Range Transport of Organic Exciton-Polaritons Revealed by Ultrafast Microscopy. *ACS Photonics* **2017**, *5* (1), 105-110. doi: 10.1021/acsp Photonics.7b01332
36. Hou, S.; Khatoniar, M.; Ding, K.; Qu, Y.; Napolov, A.; Menon, V. M.; Forrest, S. R., Ultralong-Range Energy Transport in a Disordered Organic Semiconductor at Room Temperature Via Coherent Exciton-Polariton Propagation. *Adv. Mater.* **2020**, *32* (28). doi: 10.1002/adma.202002127
37. Liu, X.; Galfsky, T.; Sun, Z.; Xia, F.; Lin, E.-c.; Lee, Y.-H.; Kéna-Cohen, S.; Menon, V. M., Strong light-matter coupling in two-dimensional atomic crystals. *Nat. Photon.* **2015**, *9* (1), 30-34. doi: 10.1038/nphoton.2014.304
38. Wang, J.; Su, R.; Xing, J.; Bao, D.; Diederichs, C.; Liu, S.; Liew, T. C. H.; Chen, Z.; Xiong, Q., Room Temperature Coherently Coupled Exciton-Polaritons in Two-Dimensional Organic-Inorganic Perovskite. *ACS Nano* **2018**, *12* (8), 8382-8389. doi: 10.1021/acsnano.8b03737
39. Michalsky, T.; Wille, M.; Grundmann, M.; Schmidt-Grund, R., Spatiotemporal Evolution of Coherent Polariton Modes in ZnO Microwire Cavities at Room Temperature. *Nano Lett.* **2018**, *18* (11), 6820-6825. doi: 10.1021/acs.nanolett.8b02705
40. Graf, A.; Tropf, L.; Zakharko, Y.; Zaumseil, J.; Gather, M. C., Near-infrared exciton-polaritons in strongly coupled single-walled carbon nanotube microcavities. *Nat. Commun.* **2016**, *7* (1), 13078. doi: 10.1038/ncomms13078
41. Graf, A.; Held, M.; Zakharko, Y.; Tropf, L.; Gather, M. C.; Zaumseil, J., Electrical pumping and tuning of exciton-polaritons in carbon nanotube microcavities. *Nat. Mater.* **2017**, *16* (9), 911-917. doi: 10.1038/nmat4940
42. Möhl, C.; Graf, A.; Berger, F. J.; Lüttgens, J.; Zakharko, Y.; Lumsargis, V.; Gather, M. C.; Zaumseil, J., Trion-Polariton Formation in Single-Walled Carbon Nanotube Microcavities. *ACS Photonics* **2018**, *5* (6), 2074-2080. doi: 10.1021/acsp Photonics.7b01549
43. Gao, W.; Li, X.; Bamba, M.; Kono, J., Continuous transition between weak and ultrastrong coupling through exceptional points in carbon nanotube microcavity exciton-polaritons. *Nat. Photon.* **2018**, *12* (6), 362-367. doi: 10.1038/s41566-018-0157-9
44. Zakharko, Y.; Graf, A.; Zaumseil, J., Plasmonic Crystals for Strong Light-Matter Coupling in Carbon Nanotubes. *Nano Lett.* **2016**, *16* (10), 6504-6510. doi: 10.1021/acs.nanolett.6b03086
45. Zakharko, Y.; Rother, M.; Graf, A.; Hähnlein, B.; Brohmann, M.; Pezoldt, J.; Zaumseil, J., Radiative Pumping and Propagation of Plexcitons in Diffractive Plasmonic Crystals. *Nano Lett.* **2018**, *18* (8), 4927-4933. doi: 10.1021/acs.nanolett.8b01733
46. Brady, G. J.; Way, A. J.; Safron, N. S.; Evensen, H. T.; Gopalan, P.; Arnold, M. S., Quasi-ballistic carbon nanotube array transistors with current density exceeding Si and GaAs. *Sci. Adv.* **2016**, *2* (9). doi: 10.1126/sciadv.1601240
47. Zhou, X.; Park, J.-Y.; Huang, S.; Liu, J.; McEuen, P. L., Band Structure, Phonon Scattering, and the Performance Limit of Single-Walled Carbon Nanotube Transistors. *Phys. Rev. Lett.* **2005**, *95* (14). doi: 10.1103/PhysRevLett.95.146805
48. Streit, J. K.; Bachilo, S. M.; Ghosh, S.; Lin, C.-W.; Weisman, R. B., Directly Measured Optical Absorption Cross Sections for Structure-Selected Single-Walled Carbon Nanotubes. *Nano Lett.* **2014**, *14* (3), 1530-1536. doi: 10.1021/nl404791y
49. Piao, Y.; Meany, B.; Powell, L. R.; Valley, N.; Kwon, H.; Schatz, G. C.; Wang, Y., Brightening of carbon nanotube photoluminescence through the incorporation of sp³ defects. *Nat. Chem.* **2013**, *5* (10), 840-845. doi: 10.1038/nchem.1711

50. Berger, F. J.; Lüttgens, J.; Nowack, T.; Kutsch, T.; Lindenthal, S.; Kistner, L.; Müller, C. C.; Bongartz, L. M.; Lumsargis, V. A.; Zakharko, Y.; Zaumseil, J., Brightening of Long, Polymer-Wrapped Carbon Nanotubes by sp³ Functionalization in Organic Solvents. *ACS Nano* **2019**, *13* (8), 9259-9269. doi: 10.1021/acsnano.9b03792
51. Settele, S.; Berger, F. J.; Lindenthal, S.; Zhao, S.; El Yumin, A. A.; Zorn, N. F.; Asyuda, A.; Zharnikov, M.; Högele, A.; Zaumseil, J., Synthetic control over the binding configuration of luminescent sp³-defects in single-walled carbon nanotubes. *Nat. Commun.* **2021**, *12* (1). doi: 10.1038/s41467-021-22307-9
52. He, X.; Hartmann, N. F.; Ma, X.; Kim, Y.; Ihly, R.; Blackburn, J. L.; Gao, W.; Kono, J.; Yomogida, Y.; Hirano, A.; Tanaka, T.; Kataura, H.; Htoon, H.; Doorn, S. K., Tunable room-temperature single-photon emission at telecom wavelengths from sp³ defects in carbon nanotubes. *Nat. Photon.* **2017**, *11*, 577. doi: 10.1038/nphoton.2017.119
53. Yuma, B.; Berciaud, S.; Besbas, J.; Shaver, J.; Santos, S.; Ghosh, S.; Weisman, R. B.; Cognet, L.; Gallart, M.; Ziegler, M.; Hönerlage, B.; Lounis, B.; Gilliot, P., Biexciton, single carrier, and trion generation dynamics in single-walled carbon nanotubes. *Phys. Rev. B* **2013**, *87* (20). doi: 10.1103/PhysRevB.87.205412
54. Jakubka, F.; Grimm, S. B.; Zakharko, Y.; Gannott, F.; Zaumseil, J., Trion Electroluminescence from Semiconducting Carbon Nanotubes. *ACS Nano* **2014**, *8* (8), 8477-8486. doi: 10.1021/nn503046y
55. Kuang, Z.; Berger, F. J.; Lustres, J. L. P.; Wollscheid, N.; Li, H.; Lüttgens, J.; Leinen, M. B.; Flavel, B. S.; Zaumseil, J.; Buckup, T., Charge Transfer from Photoexcited Semiconducting Single-Walled Carbon Nanotubes to Wide-Bandgap Wrapping Polymer. *J. Phys. Chem. C* **2021**, *125* (15), 8125-8136. doi: 10.1021/acs.jpcc.0c10171
56. Dhavamani, A.; Haeberlé, L.; Wang, J.; Kéna-Cohen, S.; Arnold, M. S., Cavity-Mediated Hybridization of Bright and Dark Excitons in an Ultrastrongly Coupled Carbon Nanotube Microcavity. *ACS Photonics* **2021**, *8* (8), 2375-2383. doi: 10.1021/acsp Photonics.1c00540
57. Lidzey, D. G.; Fox, A. M.; Rahn, M. D.; Skolnick, M. S.; Agranovich, V. M.; Walker, S., Experimental study of light emission from strongly coupled organic semiconductor microcavities following nonresonant laser excitation. *Phys. Rev. B* **2002**, *65* (19), 195312. doi: 10.1103/PhysRevB.65.195312
58. Groenhof, G.; Climent, C.; Feist, J.; Morozov, D.; Toppari, J. J., Tracking Polariton Relaxation with Multiscale Molecular Dynamics Simulations. *J. Phys. Chem. Lett.* **2019**, *10* (18), 5476-5483. doi: 10.1021/acs.jpcllett.9b02192
59. Klingshirn, C. F., *Semiconductor Optics*. Second ed.; Springer: Berlin, Heidelberg, 2003.
60. Kavokin, A.; Baumberg, J. J.; Malpuech, G.; Laussy, F. P., *Microcavities*. Second ed.; Oxford University Press: Oxford, 2017.
61. Pettersson, L. A. A.; Roman, L. S.; Inganäs, O., Modeling photocurrent action spectra of photovoltaic devices based on organic thin films. *J. Appl. Phys.* **1999**, *86* (1), 487-496. doi: 10.1063/1.370757
62. Yin, G.; Merschjann, C.; Schmid, M., The effect of surface roughness on the determination of optical constants of CuInSe₂ and CuGaSe₂ thin films. *J. Appl. Phys.* **2013**, *113* (21). doi: 10.1063/1.4809550
63. Holmes, R. J.; Forrest, S. R., Strong exciton-photon coupling in organic materials. *Org. Electron.* **2007**, *8* (2-3), 77-93. doi: 10.1016/j.orgel.2006.05.005
64. Liu, B.; Rai, P.; Grezma, J.; Twieg, R. J.; Singer, K. D., Coupling of exciton-polaritons in low-Q coupled microcavities beyond the rotating wave approximation. *Phys. Rev. B* **2015**, *92* (15). doi: 10.1103/PhysRevB.92.155301
65. Hobson, P. A.; Barnes, W. L.; Lidzey, D. G.; Gehring, G. A.; Whittaker, D. M.; Skolnick, M. S.; Walker, S., Strong exciton-photon coupling in a low-Q all-metal mirror microcavity. *Appl. Phys. Lett.* **2002**, *81* (19), 3519-3521. doi: 10.1063/1.1517714

66. Hulkko, E.; Pikker, S.; Tiainen, V.; Tichauer, R. H.; Groenhof, G.; Toppari, J. J., Effect of molecular Stokes shift on polariton dynamics. *J. Chem. Phys.* **2021**, *154* (15). doi: 10.1063/5.0037896
67. Coles, D. M.; Somaschi, N.; Michetti, P.; Clark, C.; Lagoudakis, P. G.; Savvidis, P. G.; Lidzey, D. G., Polariton-mediated energy transfer between organic dyes in a strongly coupled optical microcavity. *Nat. Mater.* **2014**, *13* (7), 712-719. doi: 10.1038/nmat3950
68. Guidelli, E. J.; Ramos, A. P.; Baffa, O., Unconventional Increase in Non-Radiative Transitions in Plasmon-Enhanced Luminescence: A Distance-Dependent Coupling. *Sci. Rep.* **2016**, *6* (1). doi: 10.1038/srep36691
69. Delbeke, D.; Bockstaele, R.; Bienstman, P.; Baets, R.; Benisty, H., High-efficiency semiconductor resonant-cavity light-emitting diodes: a review. *IEEE J. Sel. Top. Quantum Electron.* **2002**, *8* (2), 189-206. doi: 10.1109/2944.999172
70. Saxena, K.; Jain, V. K.; Mehta, D. S., A review on the light extraction techniques in organic electroluminescent devices. *Opt. Mater.* **2009**, *32* (1), 221-233. doi: 10.1016/j.optmat.2009.07.014
71. A. Jeantet, Y. C., C. Raynaud, Ph. Roussignol, J. S. Lauret, B. Besga, J. Estève, J. Reichel, and C. Voisin, Widely Tunable Single-Photon Source from a Carbon Nanotube in the Purcell Regime. *Phys. Rev. Lett.* **2016**, *116*, 247402. doi: 10.1103/PhysRevLett.116.247402
72. Portalupi, S. L.; Hornecker, G.; Giesz, V.; Grange, T.; Lemaître, A.; Demory, J.; Sagnes, I.; Lanzillotti-Kimura, N. D.; Lanco, L.; Auffèves, A.; Senellart, P., Bright Phonon-Tuned Single-Photon Source. *Nano Lett.* **2015**, *15* (10), 6290-6294. doi: 10.1021/acs.nanolett.5b00876
73. Senellart, P.; Solomon, G.; White, A., High-performance semiconductor quantum-dot single-photon sources. *Nat. Nanotechnol.* **2017**, *12* (11), 1026-1039. doi: 10.1038/nnano.2017.218
74. Bajoni, D., Polariton lasers. Hybrid light-matter lasers without inversion. *J. Phys. D: Appl. Phys.* **2012**, *45* (40), 313001. doi: 10.1088/0022-3727/45/40/409501
75. Savona, V.; Andreani, L. C.; Schwendimann, P.; Quattropani, A., Quantum well excitons in semiconductor microcavities: Unified treatment of weak and strong coupling regimes. *Solid State Commun.* **1995**, *93* (9), 733-739. doi: 10.1016/0038-1098(94)00865-5
76. Pau, S.; Björk, G.; Cao, H.; Hanamura, E.; Yamamoto, Y., Theory of inhomogeneous microcavity polariton splitting. *Solid State Commun.* **1996**, *98* (9), 781-784. doi: 10.1016/0038-1098(96)00204-9
77. Houdré, R.; Stanley, R. P.; Ilegems, M., Vacuum-field Rabi splitting in the presence of inhomogeneous broadening: Resolution of a homogeneous linewidth in an inhomogeneously broadened system. *Phys. Rev. A* **1996**, *53* (4), 2711-2715. doi: 10.1103/PhysRevA.53.2711
78. Lidzey, D. G.; Bradley, D. D. C.; Skolnick, M. S.; Virgili, T.; Walker, S.; Whittaker, D. M., Strong exciton-photon coupling in an organic semiconductor microcavity. *Nature* **1998**, *395* (6697), 53-55. doi: 10.1038/25692
79. Sabatini, R. P.; Zhang, B.; Gupta, A.; Leoni, J.; Wong, W. W. H.; Lakhwani, G., Molecularly isolated perylene diimides enable both strong exciton-photon coupling and high photoluminescence quantum yield. *J. Mater. Chem. C* **2019**, *7* (10), 2954-2960. doi: 10.1039/c9tc00093c
80. Grant, R. T.; Michetti, P.; Musser, A. J.; Gregoire, P.; Virgili, T.; Vella, E.; Cavazzini, M.; Georgiou, K.; Galeotti, F.; Clark, C.; Clark, J.; Silva, C.; Lidzey, D. G., Efficient Radiative Pumping of Polaritons in a Strongly Coupled Microcavity by a Fluorescent Molecular Dye. *Adv. Opt. Mater.* **2016**, *4* (10), 1615-1623 doi: 10.1002/adom.201600337
81. Grant, R. T.; Jayaprakash, R.; Coles, D. M.; Musser, A.; De Liberato, S.; Samuel, I. D. W.; Turnbull, G. A.; Clark, J.; Lidzey, D. G., Strong coupling in a microcavity containing β -carotene. *Opt. Express* **2018**, *26* (3). doi: 10.1364/oe.26.003320
82. Lidzey, D. G.; Bradley, D. D. C.; Armitage, A.; Virgili, T.; Skolnick, M. S.; Walker, S., Strong Coupling in Organic Semiconductor Microcavities Based on J-Aggregates. In

Multiphoton and Light Driven Multielectron Processes in Organics: New Phenomena, Materials and Applications, François Kajzar, M. V. A., Ed. Springer: Dordrecht, 2000; pp 357-370.

83. Chikkaraddy, R.; de Nijs, B.; Benz, F.; Barrow, S. J.; Scherman, O. A.; Rosta, E.; Demetriadou, A.; Fox, P.; Hess, O.; Baumberg, J. J., Single-molecule strong coupling at room temperature in plasmonic nanocavities. *Nature* **2016**, *535* (7610), 127-130. doi: 10.1038/nature17974

84. Keeling, J.; Kéna-Cohen, S., Bose–Einstein Condensation of Exciton-Polaritons in Organic Microcavities. *Annu. Rev. Phys. Chem.* **2020**, *71* (1), 435-459. doi: 10.1146/annurev-physchem-010920-102509

85. Ribeiro, R. F.; Martínez-Martínez, L. A.; Du, M.; Campos-Gonzalez-Angulo, J.; Yuen-Zhou, J., Polariton chemistry: controlling molecular dynamics with optical cavities. *Chem.* **2018**, *9* (30), 6325-6339. doi: 10.1039/c8sc01043a

86. Yamashita, K.; Huynh, U.; Richter, J.; Eyre, L.; Deschler, F.; Rao, A.; Goto, K.; Nishimura, T.; Yamao, T.; Hotta, S.; Yanagi, H.; Nakayama, M.; Friend, R. H., Ultrafast Dynamics of Polariton Cooling and Renormalization in an Organic Single-Crystal Microcavity under Nonresonant Pumping. *ACS Photonics* **2018**, *5* (6), 2182-2188. doi: 10.1021/acsp Photonics.8b00041

87. Mony, J.; Hertzog, M.; Kushwaha, K.; Börjesson, K., Angle-Independent Polariton Emission Lifetime Shown by Perylene Hybridized to the Vacuum Field Inside a Fabry–Pérot Cavity. *J. Phys. Chem. C* **2018**, *122* (43), 24917-24923. doi: 10.1021/acs.jpcc.8b07283

88. Coles, D. M.; Michetti, P.; Clark, C.; Adawi, A. M.; Lidzey, D. G., Temperature dependence of the upper-branch polariton population in an organic semiconductor microcavity. *Phys. Rev. B* **2011**, *84* (20). doi: 10.1103/PhysRevB.84.205214

89. Cao, H.; Jiang, S.; Machida, S.; Takiguchi, Y.; Yamamoto, Y., Collapse and revival of exciton–polariton oscillation in a semiconductor microcavity. *Appl. Phys. Lett.* **1997**, *71* (11), 1461-1463. doi: 10.1063/1.119936

90. Neuman, T.; Aizpurua, J., Origin of the asymmetric light emission from molecular exciton–polaritons. *Optica* **2018**, *5* (10). doi: 10.1364/optica.5.001247

91. Liu, B.; Menon, V. M.; Sfeir, M. Y., The Role of Long-Lived Excitons in the Dynamics of Strongly Coupled Molecular Polaritons. *ACS Photonics* **2020**, *7* (8), 2292-2301. doi: 10.1021/acsp Photonics.0c00895

92. Schwartz, T.; Hutchison, J. A.; Léonard, J.; Genet, C.; Haacke, S.; Ebbesen, T. W., Polariton Dynamics under Strong Light-Molecule Coupling. *ChemPhysChem* **2013**, *14* (1), 125-131. doi: 10.1002/cphc.201200734

93. Virgili, T.; Coles, D.; Adawi, A. M.; Clark, C.; Michetti, P.; Rajendran, S. K.; Brida, D.; Polli, D.; Cerullo, G.; Lidzey, D. G., Ultrafast polariton relaxation dynamics in an organic semiconductor microcavity. *Phys. Rev. B: Condens. Matter* **2011**, *83* (24), 245309. doi: 10.1103/PhysRevB.83.245309

94. Michetti, P.; Mazza, L.; La Rocca, G. C., Strongly Coupled Organic Microcavities. In *Organic Nanophotonics*, Zhao, Y. S., Ed. Springer: Berlin, 2015; pp 49-54.

95. Tassone, F.; Piermarocchi, C.; Savona, V.; Quattropani, A.; Schwendimann, P., Bottleneck effects in the relaxation and photoluminescence of microcavity polaritons. *Phys. Rev. B* **1997**, *56* (12), 7554-7563. doi: 10.1103/PhysRevB.56.7554

96. Michetti, P.; La Rocca, G. C., Simulation of J-aggregate microcavity photoluminescence. *Phys. Rev. B* **2008**, *77* (19), 195301. doi: 10.1103/PhysRevB.77.195301

97. Maragkou, M.; Grundy, A. J. D.; Ostatnický, T.; Lagoudakis, P. G., Longitudinal optical phonon assisted polariton laser. *Appl. Phys. Lett.* **2010**, *97* (11). doi: 10.1063/1.3488012

98. Litinskaya, M.; Reineker, P.; Agranovich, V. M., Fast polariton relaxation in strongly coupled organic microcavities. *J. Lumin.* **2004**, *110* (4), 364-372. doi: 10.1016/j.jlumin.2004.08.033

99. Mazza, L.; Kéna-Cohen, S.; Michetti, P.; La Rocca, G. C., Microscopic theory of polariton lasing via vibronically assisted scattering. *Phys. Rev. B* **2013**, *88* (7), 075321. doi: 10.1103/PhysRevB.88.075321

100. Coles, D. M.; Michetti, P.; Clark, C.; Tsoi, W. C.; Adawi, A. M.; Kim, J.-S.; Lidzey, D. G., Vibrationally Assisted Polariton-Relaxation Processes in Strongly Coupled Organic-Semiconductor Microcavities. *Adv. Funct. Mater.* **2011**, *21* (19), 3691-3696. doi: 10.1002/adfm.201100756
101. Coles, D. M.; Grant, R. T.; Lidzey, D. G.; Clark, C.; Lagoudakis, P. G., Imaging the polariton relaxation bottleneck in strongly coupled organic semiconductor microcavities. *Phys. Rev. B* **2013**, *88* (12), 121303. doi: 10.1103/PhysRevB.88.121303
102. Daskalakis, K. S.; Maier, S. A.; Kéna-Cohen, S., Polariton Condensation in Organic Semiconductors. In *Quantum Plasmonics*, Sergey I. Bozhevolnyi, L. M.-M., Francisco Garcia-Vidal, Ed. Springer: Basel, 2017; pp 151-163.
103. Ilani, S.; McEuen, P. L., Electron Transport in Carbon Nanotubes. *Annu. Rev. Condens. Matter Phys.* **2010**, *1* (1), 1-25. doi: 10.1146/annurev-conmatphys-070909-103928
104. Zaumseil, J., Semiconducting Single-Walled Carbon Nanotubes or Very Rigid Conjugated Polymers: A Comparison. *Adv. Electron. Mater.* **2019**, *5* (2). doi: 10.1002/aelm.201800514
105. Graf, A.; Zakharko, Y.; Schiebl, S. P.; Backes, C.; Pfohl, M.; Flavel, B. S.; Zaumseil, J., Large scale, selective dispersion of long single-walled carbon nanotubes with high photoluminescence quantum yield by shear force mixing. *Carbon* **2016**, *105*, 593-599. doi: 10.1016/j.carbon.2016.05.002
106. Maultzsch, J.; Pomraenke, R.; Reich, S.; Chang, E.; Prezzi, D.; Ruini, A.; Molinari, E.; Strano, M. S.; Thomsen, C.; Lienau, C., Exciton binding energies in carbon nanotubes from two-photon photoluminescence. *Phys. Rev. B* **2005**, *72* (24), 241402. doi: 10.1103/PhysRevB.72.241402
107. Amori, A. R.; Hou, Z.; Krauss, T. D., Excitons in Single-Walled Carbon Nanotubes and Their Dynamics. *Annu. Rev. Phys. Chem.* **2018**, *69* (1), 81-99. doi: 10.1146/annurev-physchem-050317-014241
108. Lefebvre, J.; Fraser, J. M.; Finnie, P.; Homma, Y., Photoluminescence from an individual single-walled carbon nanotube. *Phys. Rev. B* **2004**, *69* (7). doi: 10.1103/PhysRevB.69.075403
109. Lüttgens, J. M.; Berger, F. J.; Zaumseil, J., Population of Exciton-Polaritons via Luminescent sp³ Defects in Single-Walled Carbon Nanotubes. *ACS Photonics* **2020**, *8* (1), 182-193. doi: 10.1021/acsp Photonics.0c01129
110. Harrah, D. M.; Schneck, J. R.; Green, A. A.; Hersam, M. C.; Ziegler, L. D.; Swan, A. K., Intensity-Dependent Exciton Dynamics of (6,5) Single-Walled Carbon Nanotubes: Momentum Selection Rules, Diffusion, and Nonlinear Interactions. *ACS Nano* **2011**, *5* (12), 9898-9906. doi: 10.1021/nn203604v
111. Perebeinos, V.; Tersoff, J.; Avouris, P., Radiative Lifetime of Excitons in Carbon Nanotubes. *Nano Lett.* **2005**, *5* (12), 2495-2499. doi: 10.1021/nl051828s
112. Kim, Y.; Goupalov, S. V.; Weight, B. M.; Gifford, B. J.; He, X.; Saha, A.; Kim, M.; Ao, G.; Wang, Y.; Zheng, M.; Tretiak, S.; Doorn, S. K.; Htoon, H., Hidden Fine Structure of Quantum Defects Revealed by Single Carbon Nanotube Magneto-Photoluminescence. *ACS Nano* **2020**, *14* (3), 3451-3460. doi: 10.1021/acsnano.9b09548
113. Lin, C.-W.; Bachilo, S. M.; Weisman, R. B., Delayed Fluorescence from Carbon Nanotubes through Singlet Oxygen-Sensitized Triplet Excitons. *J. Am. Chem. Soc.* **2020**, *142* (50), 21189-21196. doi: 10.1021/jacs.0c10557
114. Palotás, J.; Negyedi, M.; Kollarics, S.; Bojtor, A.; Rohringer, P.; Pichler, T.; Simon, F., Incidence of Quantum Confinement on Dark Triplet Excitons in Carbon Nanotubes. *ACS Nano* **2020**, *14* (9), 11254-11261. doi: 10.1021/acsnano.0c03139
115. Mohite, A. D.; Santos, T. S.; Moodera, J. S.; Alphenaar, B. W., Observation of the triplet exciton in EuS-coated single-walled nanotubes. *Nat. Nanotechnol.* **2009**, *4* (7), 425-429. doi: 10.1038/nnano.2009.122

116. Stich, D.; Späth, F.; Kraus, H.; Sperlich, A.; Dyakonov, V.; Hertel, T., Triplet-triplet exciton dynamics in single-walled carbon nanotubes. *Nat. Photon.* **2013**, *8* (2), 139-144. doi: 10.1038/nphoton.2013.316
117. Mortimer, I. B.; Nicholas, R. J., Role of Bright and Dark Excitons in the Temperature-Dependent Photoluminescence of Carbon Nanotubes. *Phys. Rev. Lett.* **2007**, *98* (2). doi: 10.1103/PhysRevLett.98.027404
118. Perebeinos, V.; Tersoff, J.; Avouris, P., Electron-Phonon Interaction and Transport in Semiconducting Carbon Nanotubes. *Phys. Rev. Lett.* **2005**, *94* (8). doi: 10.1103/PhysRevLett.94.086802
119. Qiu, X.; Freitag, M.; Perebeinos, V.; Avouris, P., Photoconductivity Spectra of Single-Carbon Nanotubes: Implications on the Nature of Their Excited States. *Nano Lett.* **2005**, *5* (4), 749-752. doi: 10.1021/nl050227y
120. Blackburn, J. L.; Holt, J. M.; Irurzun, V. M.; Resasco, D. E.; Rumbles, G., Confirmation of K-Momentum Dark Exciton Vibronic Sidebands Using ¹³C-labeled, Highly Enriched (6,5) Single-walled Carbon Nanotubes. *Nano Lett.* **2012**, *12* (3), 1398-1403. doi: 10.1021/nl204072x
121. Torrens, O. N.; Zheng, M.; Kikkawa, J. M., Energy of K-Momentum Dark Excitons in Carbon Nanotubes by Optical Spectroscopy. *Phys. Rev. Lett.* **2008**, *101* (15), 157401. doi: 10.1103/PhysRevLett.101.157401
122. Kadria-Vili, Y.; Bachilo, S. M.; Blackburn, J. L.; Weisman, R. B., Photoluminescence Side Band Spectroscopy of Individual Single-Walled Carbon Nanotubes. *J. Phys. Chem. C* **2016**, *120* (41), 23898-23904. doi: 10.1021/acs.jpcc.6b08768
123. Ghosh, S.; Bachilo, S. M.; Simonette, R. A.; Beckingham, K. M.; Weisman, R. B., Oxygen Doping Modifies Near-Infrared Band Gaps in Fluorescent Single-Walled Carbon Nanotubes. *Science* **2010**, *330* (6011), 1656-1659. doi: 10.1126/science.1196382
124. Kumamoto, Y.; Yoshida, M.; Ishii, A.; Yokoyama, A.; Shimada, T.; Kato, Y. K., Spontaneous Exciton Dissociation in Carbon Nanotubes. *Phys. Rev. Lett.* **2014**, *112* (11). doi: 10.1103/PhysRevLett.112.117401
125. Ishii, A.; Machiya, H.; Kato, Y. K., High Efficiency Dark-to-Bright Exciton Conversion in Carbon Nanotubes. *Phys. Rev. X* **2019**, *9* (4), 041048. doi: 10.1103/PhysRevX.9.041048
126. Hertel, T.; Himmelein, S.; Ackermann, T.; Stich, D.; Crochet, J., Diffusion Limited Photoluminescence Quantum Yields in 1-D Semiconductors: Single-Wall Carbon Nanotubes. *ACS Nano* **2010**, *4* (12), 7161-7168. doi: 10.1021/nn101612b
127. Cagnet, L.; Tsyboulski, D. A.; Rocha, J. D. R.; Doyle, C. D.; Tour, J. M.; Weisman, R. B., Stepwise Quenching of Exciton Fluorescence in Carbon Nanotubes by Single-Molecule Reactions. *Science* **2007**, *316* (5830), 1465-1468. doi: 10.1126/science.1141316
128. Rajan, A.; Strano, M. S.; Heller, D. A.; Hertel, T.; Schulten, K., Length-Dependent Optical Effects in Single Walled Carbon Nanotubes†. *J. Phys. Chem. B* **2008**, *112* (19), 6211-6213. doi: 10.1021/jp077144l
129. Ma, Y.-Z.; Valkunas, L.; Dexheimer, S. L.; Bachilo, S. M.; Fleming, G. R., Femtosecond Spectroscopy of Optical Excitations in Single-Walled Carbon Nanotubes: Evidence for Exciton-Exciton Annihilation. *Phys. Rev. Lett.* **2005**, *94* (15). doi: 10.1103/PhysRevLett.94.157402
130. Russo, R. M.; Mele, E. J.; Kane, C. L.; Rubtsov, I. V.; Therien, M. J.; Luzzi, D. E., One-dimensional diffusion-limited relaxation of photoexcitations in suspensions of single-walled carbon nanotubes. *Phys. Rev. B* **2006**, *74* (4). doi: 10.1103/PhysRevB.74.041405
131. Wang, F.; Dukovic, G.; Knoesel, E.; Brus, L. E.; Heinz, T. F., Observation of rapid Auger recombination in optically excited semiconducting carbon nanotubes. *Phys. Rev. B* **2004**, *70* (24). doi: 10.1103/PhysRevB.70.241403
132. Ishii, A.; Yoshida, M.; Kato, Y. K., Exciton diffusion, end quenching, and exciton-exciton annihilation in individual air-suspended carbon nanotubes. *Phys. Rev. B* **2015**, *91* (12). doi: 10.1103/PhysRevB.91.125427

133. Bai, Y.; Bullard, G.; Olivier, J.-H.; Therien, M. J., Quantitative Evaluation of Optical Free Carrier Generation in Semiconducting Single-Walled Carbon Nanotubes. *J. Am. Chem. Soc.* **2018**, *140* (44), 14619-14626. doi: 10.1021/jacs.8b05598
134. Colombier, L.; Selles, J.; Rousseau, E.; Lauret, J. S.; Vialla, F.; Voisin, C.; Cassabois, G., Detection of a Biexciton in Semiconducting Carbon Nanotubes Using Nonlinear Optical Spectroscopy. *Phys. Rev. Lett.* **2012**, *109* (19). doi: 10.1103/PhysRevLett.109.197402
135. Santos, S. M.; Yuma, B.; Berciaud, S.; Shaver, J.; Gallart, M.; Gilliot, P.; Cognet, L.; Lounis, B., All-Optical Trion Generation in Single-Walled Carbon Nanotubes. *Phys. Rev. Lett.* **2011**, *107* (18). doi: 10.1103/PhysRevLett.107.187401
136. Park, J.; Deria, P.; Olivier, J.-H.; Therien, M. J., Fluence-Dependent Singlet Exciton Dynamics in Length-Sorted Chirality-Enriched Single-Walled Carbon Nanotubes. *Nano Lett.* **2014**, *14* (2), 504-511. doi: 10.1021/nl403511s
137. Sciascia, C.; Crochet, J.; Hertel, T.; Lanzani, G., Long lived photo excitations in (6, 5) carbon nanotubes. *Eur. Phys. J. B* **2009**, *75* (2), 115-120. doi: 10.1140/epjb/e2009-00374-1
138. Bai, Y.; Olivier, J.-H.; Bullard, G.; Liu, C.; Therien, M. J., Dynamics of charged excitons in electronically and morphologically homogeneous single-walled carbon nanotubes. *Proc. Natl. Acad. Sci. U.S.A.* **2018**, *115* (4), 674-679. doi: 10.1073/pnas.1712971115
139. Styers-Barnett, D. J.; Ellison, S. P.; Mehl, B. P.; Westlake, B. C.; House, R. L.; Park, C.; Wise, K. E.; Papanikolas, J. M., Exciton Dynamics and Biexciton Formation in Single-Walled Carbon Nanotubes Studied with Femtosecond Transient Absorption Spectroscopy. *J. Phys. Chem. C* **2008**, *112* (12), 4507-4516. doi: 10.1021/jp7099256
140. Zhu, Z.; Crochet, J.; Arnold, M. S.; Hersam, M. C.; Ulbricht, H.; Resasco, D.; Hertel, T., Pump-Probe Spectroscopy of Exciton Dynamics in (6,5) Carbon Nanotubes. *J. Phys. Chem. C* **2007**, *111* (10), 3831-3835. doi: 10.1021/jp0669411
141. Ma, Y.-Z.; Stenger, J.; Zimmermann, J.; Bachilo, S. M.; Smalley, R. E.; Weisman, R. B.; Fleming, G. R., Ultrafast carrier dynamics in single-walled carbon nanotubes probed by femtosecond spectroscopy. *J. Chem. Phys.* **2004**, *120* (7), 3368-3373. doi: 10.1063/1.1640339
142. Park, J.; Deria, P.; Therien, M. J., Dynamics and Transient Absorption Spectral Signatures of the Single-Wall Carbon Nanotube Electronically Excited Triplet State. *J. Am. Chem. Soc.* **2011**, *133* (43), 17156-17159. doi: 10.1021/ja2079477
143. Korovyanko, O. J.; Sheng, C. X.; Vardeny, Z. V.; Dalton, A. B.; Baughman, R. H., Ultrafast Spectroscopy of Excitons in Single-Walled Carbon Nanotubes. *Phys. Rev. Lett.* **2004**, *92* (1). doi: 10.1103/PhysRevLett.92.017403
144. Gokus, T.; Cognet, L.; Duque, J. G.; Pasquali, M.; Hartschuh, A.; Lounis, B., Mono- and Biexponential Luminescence Decays of Individual Single-Walled Carbon Nanotubes. *J. Phys. Chem. C* **2010**, *114* (33), 14025-14028. doi: 10.1021/jp1049217
145. Brozena, A. H.; Kim, M.; Powell, L. R.; Wang, Y., Controlling the optical properties of carbon nanotubes with organic colour-centre quantum defects. *Nat. Rev. Chem.* **2019**, *3* (6), 375-392. doi: 10.1038/s41570-019-0103-5
146. Shiraki, T.; Miyauchi, Y.; Matsuda, K.; Nakashima, N., Carbon Nanotube Photoluminescence Modulation by Local Chemical and Supramolecular Chemical Functionalization. *Acc. Chem. Res.* **2020**, *53* (9), 1846-1859. doi: 10.1021/acs.accounts.0c00294
147. Kwon, H.; Furmanchuk, A. o.; Kim, M.; Meany, B.; Guo, Y.; Schatz, G. C.; Wang, Y., Molecularly Tunable Fluorescent Quantum Defects. *J. Am. Chem. Soc.* **2016**, *138* (21), 6878-6885. doi: 10.1021/jacs.6b03618
148. Gifford, B. J.; He, X.; Kim, M.; Kwon, H.; Saha, A.; Sifain, A. E.; Wang, Y.; Htoon, H.; Kilina, S.; Doorn, S. K.; Tretiak, S., Optical Effects of Divalent Functionalization of Carbon Nanotubes. *Chem. Mat.* **2019**, *31* (17), 6950-6961. doi: 10.1021/acs.chemmater.9b01438
149. Kim, M.; Adamska, L.; Hartmann, N. F.; Kwon, H.; Liu, J.; Velizhanin, K. A.; Piao, Y.; Powell, L. R.; Meany, B.; Doorn, S. K.; Tretiak, S.; Wang, Y., Fluorescent Carbon Nanotube Defects Manifest Substantial Vibrational Reorganization. *J. Phys. Chem. C* **2016**, *120* (20), 11268-11276. doi: 10.1021/acs.jpcc.6b02538

150. Berger, F. Luminescent Defects in Polymer-Wrapped Carbon Nanotubes. Dissertation, Ruprecht-Karls-Universität Heidelberg, Heidelberg, 2021.
151. Spataru, C. D.; Ismail-Beigi, S.; Capaz, R. B.; Louie, S. G., Theory and Ab Initio Calculation of Radiative Lifetime of Excitons in Semiconducting Carbon Nanotubes. *Phys. Rev. Lett.* **2005**, *95* (24). doi: 10.1103/PhysRevLett.95.247402
152. He, X.; Sun, L.; Gifford, B. J.; Tretiak, S.; Piryatinski, A.; Li, X.; Htoon, H.; Doorn, S. K., Intrinsic limits of defect-state photoluminescence dynamics in functionalized carbon nanotubes. *Nanoscale* **2019**, *11* (18), 9125-9132. doi: 10.1039/c9nr02175b
153. He, X.; Velizhanin, K. A.; Bullard, G.; Bai, Y.; Olivier, J.-H.; Hartmann, N. F.; Gifford, B. J.; Kilina, S.; Tretiak, S.; Htoon, H.; Therien, M. J.; Doorn, S. K., Solvent- and Wavelength-Dependent Photoluminescence Relaxation Dynamics of Carbon Nanotube sp³ Defect States. *ACS Nano* **2018**, *12* (8), 8060-8070. doi: 10.1021/acsnano.8b02909
154. Hartmann, N. F.; Velizhanin, K. A.; Haroz, E. H.; Kim, M.; Ma, X.; Wang, Y.; Htoon, H.; Doorn, S. K., Photoluminescence Dynamics of Aryl sp³ Defect States in Single-Walled Carbon Nanotubes. *ACS Nano* **2016**, *10* (9), 8355-8365. doi: 10.1021/acsnano.6b02986
155. Aharoni, A.; Oron, D.; Banin, U.; Rabani, E.; Jortner, J., Long-Range Electronic-to-Vibrational Energy Transfer from Nanocrystals to Their Surrounding Matrix Environment. *Phys. Rev. Lett.* **2008**, *100* (5). doi: 10.1103/PhysRevLett.100.057404
156. Kim, Y.; Velizhanin, K. A.; He, X.; Sarpkaya, I.; Yomogida, Y.; Tanaka, T.; Kataura, H.; Doorn, S. K.; Htoon, H., Photoluminescence Intensity Fluctuations and Temperature-Dependent Decay Dynamics of Individual Carbon Nanotube sp³ Defects. *J. Phys. Chem. Lett.* **2019**, *10* (6), 1423-1430. doi: 10.1021/acscjpclett.8b03732
157. Nutz, M.; Zhang, J.; Kim, M.; Kwon, H.; Wu, X.; Wang, Y.; Högele, A., Photon Correlation Spectroscopy of Luminescent Quantum Defects in Carbon Nanotubes. *Nano Lett.* **2019**, *19* (10), 7078-7084. doi: 10.1021/acs.nanolett.9b02553
158. Ren, H.; Chen, J. D.; Li, Y. Q.; Tang, J. X., Recent Progress in Organic Photodetectors and their Applications. *Adv. Sci.* **2020**, *8* (1). doi: 10.1002/advs.202002418
159. Baeg, K.-J.; Binda, M.; Natali, D.; Caironi, M.; Noh, Y.-Y., Organic Light Detectors: Photodiodes and Phototransistors. *Adv. Mater.* **2013**, *25* (31), 4267-4295. doi: 10.1002/adma.201204979
160. Hiramoto, M.; Shinmura, Y., Organic Solar Cells. In *Springer Handbook of Electronic and Photonic Materials*, Second ed.; Safa Kasap, P. C., Ed. Springer: Basel, 2017; pp 1329-1338.
161. Fukuda, K.; Yu, K.; Someya, T., The Future of Flexible Organic Solar Cells. *Adv. Energy Mater.* **2020**, *10* (25). doi: 10.1002/aenm.202000765
162. Irvine, S., Solar Cells and Photovoltaics. In *Springer Handbook of Electronic and Photonic Materials*, Second ed.; Safa Kasap, P. C., Ed. Springer: Basel, 2017; pp 1097-1109.
163. Strobel, N.; Seiberlich, M.; Eckstein, R.; Lemmer, U.; Hernandez-Sosa, G., Organic photodiodes: printing, coating, benchmarks, and applications. *Flex. Print* **2019**, *4* (4). doi: 10.1088/2058-8585/ab56dd
164. De Wolf, S.; Holovsky, J.; Moon, S.-J.; Löper, P.; Niesen, B.; Ledinsky, M.; Haug, F.-J.; Yum, J.-H.; Ballif, C., Organometallic Halide Perovskites: Sharp Optical Absorption Edge and Its Relation to Photovoltaic Performance. *J. Phys. Chem. Lett.* **2014**, *5* (6), 1035-1039. doi: 10.1021/jz500279b
165. Pichler, S.; Rauch, T.; Seyrkammer, R.; Böberl, M.; Tedde, S. F.; Fürst, J.; Kovalenko, M. V.; Lemmer, U.; Hayden, O.; Heiss, W., Temperature dependent photoresponse from colloidal PbS quantum dot sensitized inorganic/organic hybrid photodiodes. *Appl. Phys. Lett.* **2011**, *98* (5). doi: 10.1063/1.3552678
166. Richter, M.; Heumüller, T.; Matt, G. J.; Heiss, W.; Brabec, C. J., Carbon Photodetectors: The Versatility of Carbon Allotropes. *Adv. Energy Mater.* **2017**, *7* (10). doi: 10.1002/aenm.201601574

167. Arnold, M. S.; Zimmerman, J. D.; Renshaw, C. K.; Xu, X.; Lunt, R. R.; Austin, C. M.; Forrest, S. R., Broad Spectral Response Using Carbon Nanotube/Organic Semiconductor/C60 Photodetectors. *Nano Lett.* **2009**, *9* (9), 3354-3358. doi: 10.1021/nl901637u
168. Lupton, J. M.; Koeppel, R.; Müller, J. G.; Feldmann, J.; Scherf, U.; Lemmer, U., Organic Microcavity Photodiodes. *Adv. Mater.* **2003**, *15* (17), 1471-1474. doi: 10.1002/adma.200301644
169. Armin, A.; Jansen-van Vuuren, R. D.; Kopidakis, N.; Burn, P. L.; Meredith, P., Narrowband light detection via internal quantum efficiency manipulation of organic photodiodes. *Nat. Commun.* **2015**, *6* (1). doi: 10.1038/ncomms7343
170. Tang, Z.; Ma, Z.; Sánchez-Díaz, A.; Ullbrich, S.; Liu, Y.; Siegmund, B.; Mischok, A.; Leo, K.; Campoy-Quiles, M.; Li, W.; Vandewal, K., Polymer:Fullerene Bimolecular Crystals for Near-Infrared Spectroscopic Photodetectors. *Adv. Mater.* **2017**, *29* (33). doi: 10.1002/adma.201702184
171. de Mello, J. C.; Wittmann, H. F.; Friend, R. H., An improved experimental determination of external photoluminescence quantum efficiency. *Adv. Mater.* **1997**, *9* (3), 230-232. doi: 10.1002/adma.19970090308
172. Ahn, T.-S.; Al-Kaysi, R. O.; Müller, A. M.; Wentz, K. M.; Bardeen, C. J., Self-absorption correction for solid-state photoluminescence quantum yields obtained from integrating sphere measurements. *Sci. Instrum.* **2007**, *78* (8). doi: 10.1063/1.2768926
173. OriginPro 2020 (Lehre); OriginLab Corporation: Northampton, Massachusetts, 2020.
174. MATLAB 9.10.0.1602886 The MathWorks Inc.: Natick, Massachusetts, 2021.
175. MATLAB *Global Optimization Toolbox 4.5*, 9.10.0.1602886 The MathWorks Inc.: Natick, Massachusetts, 2021.
176. Liu, B.; Menon, V. M.; Sfeir, M. Y., Ultrafast thermal modification of strong coupling in an organic microcavity. *APL Photonics* **2021**, *6* (1). doi: 10.1063/5.0031560
177. Rakić, A. D.; Djurišić, A. B.; Elazar, J. M.; Majewski, M. L., Optical properties of metallic films for vertical-cavity optoelectronic devices. *Appl. Opt.* **1998**, *37* (22). doi: 10.1364/ao.37.005271
178. Alagna, N.; Lustres, J. L. P.; Roozbeh, A.; Han, J.; Hahn, S.; Berger, F. J.; Zaumseil, J.; Dreuw, A.; Bunz, U. H. F.; Buckup, T., Ultrafast Singlet Fission in Rigid Azaarene Dimers with Negligible Orbital Overlap. *J. Phys. Chem. B* **2020**, *124* (41), 9163-9174. doi: 10.1021/acs.jpcc.0c07096
179. Reich, S.; Thomsen, C.; Maultzsch, J., *Carbon nanotubes : basic concepts and physical properties*. Wiley-VCH: Weinheim ; Cambridge, 2004; p 215.
180. Popov, V. N., Theoretical evidence for T1/2 specific heat behavior in carbon nanotube systems. *Carbon* **2004**, *42* (5-6), 991-995. doi: 10.1016/j.carbon.2003.12.014
181. Ma, X.; Hartmann, N. F.; Baldwin, J. K. S.; Doorn, S. K.; Htoon, H., Room-temperature single-photon generation from solitary dopants of carbon nanotubes. *Nat. Nanotechnol.* **2015**, *10*, 671. doi: 10.1038/nnano.2015.136
182. Zheng, Y.; Bachilo, S. M.; Weisman, R. B., Photoexcited Aromatic Reactants Give Multicolor Carbon Nanotube Fluorescence from Quantum Defects. *ACS Nano* **2019**, *14* (1), 715-723. doi: 10.1021/acsnano.9b07606
183. Shiraki, T.; Shiraishi, T.; Juhász, G.; Nakashima, N., Emergence of new red-shifted carbon nanotube photoluminescence based on proximal doped-site design. *Sci. Rep.* **2016**, *6* (1). doi: 10.1038/srep28393
184. Renken, S. P., R.; Georgiou, K.; Jayaprakash, R.; Gai, L.; Shen, Z.; Lidzey, D. G.; Rao, A.; Musser, A. J., Untargeted Effects in Organic Exciton-Polariton Transient Spectroscopy: A Cautionary Tale. *arXiv: 2107.05708* 2021.
185. Maiuri, M.; Garavelli, M.; Cerullo, G., Ultrafast Spectroscopy: State of the Art and Open Challenges. *J. Am. Chem. Soc.* **2019**, *142* (1), 3-15. doi: 10.1021/jacs.9b10533

186. Mewes, L.; Wang, M.; Ingle, R. A.; Börjesson, K.; Chergui, M., Energy relaxation pathways between light-matter states revealed by coherent two-dimensional spectroscopy. *Commun. Phys* **2020**, *3* (1). doi: 10.1038/s42005-020-00424-z
187. Wang, S.; Chervy, T.; George, J.; Hutchison, J. A.; Genet, C.; Ebbesen, T. W., Quantum Yield of Polariton Emission from Hybrid Light-Matter States. *J. Phys. Chem. Lett.* **2014**, *5* (8), 1433-1439. doi: 10.1021/jz5004439
188. Song, J.-H.; He, Y.; Nurmikko, A. V.; Tischler, J.; Bulovic, V., Exciton-polariton dynamics in a transparent organic semiconductor microcavity. *Phys. Rev. B* **2004**, *69* (23). doi: 10.1103/PhysRevB.69.235330
189. Savvidis, P. G.; Connolly, L. G.; Skolnick, M. S.; Lidzey, D. G.; Baumberg, J. J., Ultrafast polariton dynamics in strongly coupled zinc porphyrin microcavities at room temperature. *Phys. Rev. B* **2006**, *74* (11). doi: 10.1103/PhysRevB.74.113312
190. Takemura, N.; Trebaol, S.; Anderson, M. D.; Kohnle, V.; Léger, Y.; Oberli, D. Y.; Portella-Oberli, M. T.; Deveaud, B., Two-dimensional Fourier transform spectroscopy of exciton-polaritons and their interactions. *Phys. Rev. B* **2015**, *92* (12). doi: 10.1103/PhysRevB.92.125415
191. Wen, P.; Christmann, G.; Baumberg, J. J.; Nelson, K. A., Influence of multi-exciton correlations on nonlinear polariton dynamics in semiconductor microcavities. *New J. Phys.* **2013**, *15* (2). doi: 10.1088/1367-2630/15/2/025005
192. DelPo, C. A.; Kudisch, B.; Park, K. H.; Khan, S.-U.-Z.; Fassioli, F.; Fausti, D.; Rand, B. P.; Scholes, G. D., Polariton Transitions in Femtosecond Transient Absorption Studies of Ultrastrong Light-Molecule Coupling. *J. Phys. Chem. Lett.* **2020**, *11* (7), 2667-2674. doi: 10.1021/acs.jpcclett.0c00247
193. Neukirch, U.; Bolton, S. R.; Fromer, N. A.; Sham, L. J.; Chemla, D. S., Polariton-Biexciton Transitions in a Semiconductor Microcavity. *Phys. Rev. Lett.* **2000**, *84* (10), 2215-2218. doi: 10.1103/PhysRevLett.84.2215
194. Saba, M.; Quochi, F.; Ciuti, C.; Oesterle, U.; Staehli, J. L.; Deveaud, B.; Bongiovanni, G.; Mura, A., Crossover from Exciton to Biexciton Polaritons in Semiconductor Microcavities. *Phys. Rev. Lett.* **2000**, *85* (2), 385-388. doi: 10.1103/PhysRevLett.85.385
195. Dunkelberger, A. D.; Spann, B. T.; Fears, K. P.; Simpkins, B. S.; Owrutsky, J. C., Modified relaxation dynamics and coherent energy exchange in coupled vibration-cavity polaritons. *Nat. Commun.* **2016**, *7* (1). doi: 10.1038/ncomms13504
196. Groeneveld, R. H. M.; Sprik, R.; Lagendijk, A., Femtosecond spectroscopy of electron-electron and electron-phonon energy relaxation in Ag and Au. *Phys. Rev. B* **1995**, *51* (17), 11433-11445. doi: 10.1103/PhysRevB.51.11433
197. Smith, A. N.; Norris, P. M., Influence of intraband transitions on the electron thermoreflectance response of metals. *Appl. Phys. Lett.* **2001**, *78* (9), 1240-1242. doi: 10.1063/1.1351523
198. McPeak, K. M.; Jayanti, S. V.; Kress, S. J. P.; Meyer, S.; Iotti, S.; Rossinelli, A.; Norris, D. J., Plasmonic Films Can Easily Be Better: Rules and Recipes. *ACS Photonics* **2015**, *2* (3), 326-333. doi: 10.1021/ph5004237
199. van Stokkum, I. H. M.; Larsen, D. S.; van Grondelle, R., Global and target analysis of time-resolved spectra. *Biochim. Biophys. Acta - Bioenerg.* **2004**, *1657* (2-3), 82-104. doi: 10.1016/j.bbabi.2004.04.011
200. Levinsen, J.; Marchetti, F. M.; Keeling, J.; Parish, M. M., Spectroscopic Signatures of Quantum Many-Body Correlations in Polariton Microcavities. *Phys. Rev. Lett.* **2019**, *123* (26). doi: 10.1103/PhysRevLett.123.266401
201. Zhu, L.; Zhang, M.; Zhou, G.; Hao, T.; Xu, J.; Wang, J.; Qiu, C.; Prine, N.; Ali, J.; Feng, W.; Gu, X.; Ma, Z.; Tang, Z.; Zhu, H.; Ying, L.; Zhang, Y.; Liu, F., Efficient Organic Solar Cell with 16.88% Efficiency Enabled by Refined Acceptor Crystallization and Morphology with Improved Charge Transfer and Transport Properties. *Adv. Energy Mater.* **2020**, *10* (18). doi: 10.1002/aenm.201904234

202. Ullbrich, S.; Siegmund, B.; Mischok, A.; Hofacker, A.; Benduhn, J.; Spoltore, D.; Vandewal, K., Fast Organic Near-Infrared Photodetectors Based on Charge-Transfer Absorption. *J. Phys. Chem. Lett.* **2017**, *8* (22), 5621-5625. doi: 10.1021/acs.jpcelett.7b02571
203. Rühle, S., Tabulated values of the Shockley–Queisser limit for single junction solar cells. *Sol. Energy* **2016**, *130*, 139-147. doi: 10.1016/j.solener.2016.02.015
204. He, X.; Léonard, F.; Kono, J., Uncooled Carbon Nanotube Photodetectors. *Adv. Opt. Mater.* **2015**, *3* (8), 989-1011. doi: 10.1002/adom.201500237
205. Xie, B.; Chen, Z.; Ying, L.; Huang, F.; Cao, Y., Near-infrared organic photoelectric materials for light-harvesting systems: Organic photovoltaics and organic photodiodes. *InfoMat* **2019**, *2* (1), 57-91. doi: 10.1002/inf2.12063
206. Fang, Y.; Dong, Q.; Shao, Y.; Yuan, Y.; Huang, J., Highly narrowband perovskite single-crystal photodetectors enabled by surface-charge recombination. *Nat. Photon.* **2015**, *9* (10), 679-686. doi: 10.1038/nphoton.2015.156
207. Classen, A.; Einsiedler, L.; Heumueller, T.; Graf, A.; Brohmann, M.; Berger, F.; Kahmann, S.; Richter, M.; Matt, G. J.; Forberich, K.; Zaumseil, J.; Brabec, C. J., Absence of Charge Transfer State Enables Very Low VOC Losses in SWCNT:Fullerene Solar Cells. *Adv. Energy Mater.* **2019**, *9* (1). doi: 10.1002/aenm.201801913
208. Lee, H. S.; Ahn, J.; Shim, W.; Im, S.; Hwang, D. K., 2D WSe₂/MoS₂ van der Waals heterojunction photodiode for visible-near infrared broadband detection. *Appl. Phys. Lett.* **2018**, *113* (16). doi: 10.1063/1.5042440
209. Siegmund, B.; Mischok, A.; Benduhn, J.; Zeika, O.; Ullbrich, S.; Nehm, F.; Böhm, M.; Spoltore, D.; Fröb, H.; Körner, C.; Leo, K.; Vandewal, K., Organic narrowband near-infrared photodetectors based on intermolecular charge-transfer absorption. *Nat. Commun.* **2017**, *8* (1). doi: 10.1038/ncomms15421
210. Shastry, T. A.; Clark, S. C.; Rowberg, A. J. E.; Luck, K. A.; Chen, K.-S.; Marks, T. J.; Hersam, M. C., Enhanced Uniformity and Area Scaling in Carbon Nanotube-Fullerene Bulk-Heterojunction Solar Cells Enabled by Solvent Additives. *Adv. Energy Mater.* **2016**, *6* (2). doi: 10.1002/aenm.201501466
211. Jain, R. M.; Howden, R.; Tvrdy, K.; Shimizu, S.; Hilmer, A. J.; McNicholas, T. P.; Gleason, K. K.; Strano, M. S., Polymer-Free Near-Infrared Photovoltaics with Single Chirality (6,5) Semiconducting Carbon Nanotube Active Layers. *Adv. Mater.* **2012**, *24* (32), 4436-4439. doi: 10.1002/adma.201202088
212. Liang, S.; Ma, Z.; Wu, G.; Wei, N.; Huang, L.; Huang, H.; Liu, H.; Wang, S.; Peng, L.-M., Microcavity-Integrated Carbon Nanotube Photodetectors. *ACS Nano* **2016**, *10* (7), 6963-6971. doi: 10.1021/acsnano.6b02898
213. Lee, H. W.; Yoon, Y.; Park, S.; Oh, J. H.; Hong, S.; Liyanage, L. S.; Wang, H.; Morishita, S.; Patil, N.; Park, Y. J.; Park, J. J.; Spakowitz, A.; Galli, G.; Gygi, F.; Wong, P. H. S.; Tok, J. B. H.; Kim, J. M.; Bao, Z., Selective dispersion of high purity semiconducting single-walled carbon nanotubes with regioregular poly(3-alkylthiophene)s. *Nat. Commun.* **2011**, *2* (1). doi: 10.1038/ncomms1545
214. Siddiqui, H.; Parra, M. R.; Pandey, P.; Qureshi, M. S.; Haque, F. Z., Combined parametric optimization of P3HT: PC70BM films for efficient bulk-heterojunction solar cells. *J. Solid State Electrochem.* **2019**, *23* (12), 3267-3274. doi: 10.1007/s10008-019-04421-3
215. Ameri, T.; Dennler, G.; Waldauf, C.; Azimi, H.; Seemann, A.; Forberich, K.; Hauch, J.; Scharber, M.; Hingerl, K.; Brabec, C. J., Fabrication, Optical Modeling, and Color Characterization of Semitransparent Bulk-Heterojunction Organic Solar Cells in an Inverted Structure. *Adv. Funct. Mater.* **2010**, *20* (10), 1592-1598. doi: 10.1002/adfm.201000176
216. Simone, G.; Dyson, M. J.; Weijtens, C. H. L.; Meskers, S. C. J.; Coehoorn, R.; Janssen, R. A. J.; Gelinck, G. H., On the Origin of Dark Current in Organic Photodiodes. *Adv. Opt. Mater.* **2019**, *8* (1). doi: 10.1002/adom.201901568
217. Gong, M.; Shastry, T. A.; Xie, Y.; Bernardi, M.; Jasion, D.; Luck, K. A.; Marks, T. J.; Grossman, J. C.; Ren, S.; Hersam, M. C., Polychiral Semiconducting Carbon Nanotube–Fullerene Solar Cells. *Nano Lett.* **2014**, *14* (9), 5308-5314. doi: 10.1021/nl5027452

218. Zhao, J.; Su, R.; Fieramosca, A.; Zhao, W.; Du, W.; Liu, X.; Diederichs, C.; Sanvitto, D.; Liew, T. C. H.; Xiong, Q., Ultralow Threshold Polariton Condensate in a Monolayer Semiconductor Microcavity at Room Temperature. *Nano Lett.* **2021**, *21* (7), 3331-3339. doi: 10.1021/acs.nanolett.1c01162
219. Polimeno, L.; Fieramosca, A.; Lerario, G.; Cinquino, M.; De Giorgi, M.; Ballarini, D.; Todisco, F.; Dominici, L.; Ardizzone, V.; Pugliese, M.; Prontera, C. T.; Maiorano, V.; Gigli, G.; De Marco, L.; Sanvitto, D., Observation of Two Thresholds Leading to Polariton Condensation in 2D Hybrid Perovskites. *Adv. Opt. Mater.* **2020**, *8* (16). doi: 10.1002/adom.202000176
220. Schouwink, P.; Lupton, J. M.; von Berlepsch, H.; Dähne, L.; Mahrt, R. F., Nonequilibrium polariton dynamics in organic microcavities. *Phys. Rev. B* **2002**, *66* (8). doi: 10.1103/PhysRevB.66.081203
221. Wang, W.; Vasa, P.; Sommer, E.; De Sio, A.; Gross, P.; Vogelgesang, R.; Lienau, C., Observation of Lorentzian lineshapes in the room temperature optical spectra of strongly coupled J-aggregate/metal hybrid nanostructures by linear two-dimensional optical spectroscopy. *J. Opt.* **2014**, *16* (11). doi: 10.1088/2040-8978/16/11/114021
222. Takahashi, S.; Watanabe, K., Decoupling from a Thermal Bath via Molecular Polariton Formation. *J. Phys. Chem. Lett.* **2020**, *11* (4), 1349-1356. doi: 10.1021/acs.jpcclett.9b03789
223. Sykes, M. E.; Kim, M.; Wu, X.; Wiederrecht, G. P.; Peng, L.; Wang, Y.; Gosztola, D. J.; Ma, X., Ultrafast Exciton Trapping at sp³ Quantum Defects in Carbon Nanotubes. *ACS Nano* **2019**, *13* (11), 13264-13270. doi: 10.1021/acs.nano.9b06279
224. Pfohl, M.; Glaser, K.; Graf, A.; Mertens, A.; Tune, D. D.; Puerckhauer, T.; Alam, A.; Wei, L.; Chen, Y.; Zaumseil, J.; Colsmann, A.; Krupke, R.; Flavel, B. S., Probing the Diameter Limit of Single Walled Carbon Nanotubes in SWCNT: Fullerene Solar Cells. *Adv. Energy Mater.* **2016**, *6* (21). doi: 10.1002/aenm.201600890
225. Ren, S.; Bernardi, M.; Lunt, R. R.; Bulovic, V.; Grossman, J. C.; Gradečak, S., Toward Efficient Carbon Nanotube/P3HT Solar Cells: Active Layer Morphology, Electrical, and Optical Properties. *Nano Lett.* **2011**, *11* (12), 5316-5321. doi: 10.1021/nl202796u
226. Hertel, T.; Perebeinos, V.; Crochet, J.; Arnold, K.; Kappes, M.; Avouris, P., Intersubband Decay of 1-D Exciton Resonances in Carbon Nanotubes. *Nano Lett.* **2007**, *8* (1), 87-91. doi: 10.1021/nl0720915
227. Lüer, L.; Gadermaier, C.; Crochet, J.; Hertel, T.; Brida, D.; Lanzani, G., Coherent Phonon Dynamics in Semiconducting Carbon Nanotubes: A Quantitative Study of Electron-Phonon Coupling. *Phys. Rev. Lett.* **2009**, *102* (12). doi: 10.1103/PhysRevLett.102.127401

Eidesstattliche Versicherung gemäß §8 der Promotionsordnung der Gesamtfakultät für Mathematik, Ingenieur- und Naturwissenschaften der Universität Heidelberg

Bei der eingereichten Dissertation zu dem Thema

Strong light-matter coupling with single-walled carbon nanotubes

handelt es sich um meine eigenständig erbrachte Leistung.

Ich habe nur die angegebenen Quellen und Hilfsmittel benutzt und mich keiner unzulässigen Hilfe Dritter bedient. Insbesondere habe ich wörtlich oder sinngemäß aus anderen Werken übernommene Inhalte als solche kenntlich gemacht.

Die Arbeit oder Teile davon habe ich bislang nicht an einer Hochschule des In- oder Auslands als Bestandteil einer Prüfungs- oder Qualifikationsleistung vorgelegt. Die Richtigkeit der vorstehenden Erklärungen bestätige ich. Die Bedeutung der eidesstattlichen Versicherung und der strafrechtlichen Folgen einer unrichtigen oder unvollständigen eidesstattlichen Versicherung sind mir bekannt.

Ich versichere an Eides statt, dass ich nach bestem Wissen die reine Wahrheit erklärt und nichts verschwiegen habe.

Lund (Schweden), 9. November 2021

Jan Matthias Lüttgens

